



Master Thesis on the Subject

Charge Transfer Processes in Gold-Titania Nanostructures

For Obtaining the Degree

Master of Science (M.Sc.) in Physics

Lisa Mehner

24.03.2025

First Reviewer: Prof. Dr. Matias Bargheer
Second Reviewer: Prof. Dr. Svetlana Santer
Supervisor: Dr. Wouter Koopman

Ultrafast Dynamics in Condensed Matter
Institute of Physics and Astronomy
Faculty of Sciences
University of Potsdam

Abstract

Metallic nanoparticles (NPs) are popular as photocatalysts and enable chemical reactions, such as artificial photosynthesis. Their large absorption cross section and bandwidth make them suitable for a broad range of applications. To extend the short lifetime of excited carriers in metals and make the carriers available for chemical reactions, they can be collected by a semiconductor. Optimizing charge carrier injection from metallic NPs into semiconductors is an active field of research.

Within this master's thesis the injection of electrons from Au NPs into commercially available P25 TiO₂ NPs is investigated using transient absorption spectroscopy. The absorption of infrared (IR) radiation is proportional to the number of electrons in the TiO₂ conduction band. Therefore, a working setup for transient IR absorption spectroscopy was established in the UDKM optics lab using a two-step IR non-collinear optical parametric amplifier (NOPA). To excite charges in the Au NPs that can be transferred to TiO₂, a pump wavelength of 400 nm was chosen to excite interband transitions.

With $\lambda_{\text{pump}} = 400 \text{ nm}$ and $\lambda_{\text{probe}} = 2200 \text{ nm}$ multiple fluences were measured on samples with TiO₂& Au NPs and only TiO₂ NPs for comparison. The amplitudes show a linear behavior with the fluence, indicating the absence of tunneling and thermal excitations. Comparing both samples for similar fluences reveals a faster signal decay for samples with Au NPs. Back transfer of electrons from TiO₂ to Au might be the cause.

Contrary to other experiments in this field, the pump wavelength can directly excite the TiO₂ NPs. This leads to a complex dynamic, which has yet to be unraveled.

Kurzdarstellung

Metallische Nanopartikel (NP) erfreuen sich großer Beliebtheit als Photokatalysatoren und werden eingesetzt, um chemische Reaktionen wie die künstliche Photosynthese zu ermöglichen. Aufgrund ihres großen Absorptionsquerschnitts und ihrer breiten Bandbreite sind sie für viele Anwendungen geeignet. Um die kurze Lebensdauer der angeregten Ladungsträger in Metallen zu verlängern und diese für chemische Reaktionen zugänglich zu machen, können die Ladungsträger auf Halbleiter übertragen werden. Die Optimierung des Ladungsträgertransfers von metallischen NP zu Halbleitern ist ein aktives Forschungsgebiet.

Im Rahmen dieser Masterarbeit wird mittels transientser Absorptionsspektroskopie untersucht, wie Elektronen von Au NP in kommerziell erhältliche P25-TiO₂ NP injiziert werden. Die Absorption von Infrarot (IR)-Strahlung dient als Maß für die Anzahl der Elektronen im Leitungsband von TiO₂. Daher wurde im Optiklabor der UDKM ein funktionierendes Setup für die transiente IR-Absorptionsspektroskopie eingerichtet, das einen nicht-kollinearen optisch-parametrischen Verstärker (NOPA) nutzt. Um Ladungen in den Au NP anzuregen, die auf TiO₂ übertragen werden können, wurde eine Pumpwellenlänge von 400 nm gewählt, um Interbandübergänge zu stimulieren.

Bei Messungen mit $\lambda_{\text{pump}} = 400 \text{ nm}$ und $\lambda_{\text{probe}} = 2200 \text{ nm}$ wurden Fluenzserien an Proben mit TiO₂-Au NP sowie an reinen TiO₂ NP zum Vergleich aufgenommen. Die Amplituden zeigen ein lineares Verhalten in Abhängigkeit von der Fluenz, was auf das Fehlen von Tunnelprozessen und thermischen Anregungen hinweist. Ein Vergleich der Proben bei ähnlichen Fluenzwerten zeigt einen schnelleren Signalabfall bei den Proben mit Au NP. Es wird vermutet, dass der Rücktransfer von Elektronen von TiO₂ zu den Au NP hierfür verantwortlich ist.

Anders als bei anderen Experimenten in diesem Feld kann die Pumpwellenlänge TiO₂ NP direkt anregen. Dies führt zu einer komplexen Dynamik, die noch entschlüsselt werden muss.

Contents

| | |
|--|-----------|
| Contents | v |
| 1 Introduction | 1 |
| 2 Background | 5 |
| 2.1 Metal- and semiconductor interface physics | 5 |
| 2.1.1 Schottky barrier at metal semiconductor interface | 5 |
| 2.1.2 Other interface models | 7 |
| 2.1.3 Electron transfer processes | 8 |
| 2.2 Transient measurement of Au - TiO ₂ charge transfer | 10 |
| 2.2.1 Visible pumping of Au | 10 |
| 2.2.2 IR probe of TiO ₂ | 13 |
| 2.2.3 Deviations due to visible absorption in TiO ₂ | 13 |
| 3 NOPA-NOPA transient IR absorption spectroscopy | 17 |
| 3.1 Transient absorption spectroscopy setup | 17 |
| 3.2 Nonlinear optics: why intensity is important | 19 |
| 3.3 Visible NOPA | 22 |
| 3.3.1 White light generation | 23 |
| 3.3.2 Generating the pump beam from SHG | 24 |
| 3.3.3 Amplification process | 29 |
| 3.3.4 Alignment steps | 34 |
| 3.4 IR NOPA | 35 |
| 3.5 Characterization of NOPAs | 37 |
| 3.5.1 Spectra | 37 |
| 3.5.2 Determination of the pulse duration via autocorrelation (AC) | 39 |
| 3.5.3 Beam profiles | 41 |
| 3.6 Optimizations | 43 |
| 4 Measurements and analysis | 47 |
| 4.1 Sample characterization | 47 |
| 4.2 Pump-probe measurements | 50 |
| 4.2.1 Data analysis | 50 |
| 4.2.2 Homogeneity | 54 |
| 4.2.3 Fluence series | 54 |
| 4.2.4 Problems with fluence series | 58 |
| 4.2.5 Results | 67 |
| 5 Conclusion | 77 |
| 6 Appendix | 79 |
| 7 Authorship declaration | 87 |
| 8 Acknowledgments | 89 |

1 Introduction

To satisfy the ever-growing energy consumption in today's globalized society and economy, it has become a crucial task for researchers to uncover new sources of sustainable energy and to optimize the efficiency of existing technologies.

In pursuing this goal, photocatalysis has become a popular field of research. It aims, for example, at reducing CO_2 to organic compounds which can be used as synthetic fuels. CO_2 is a very stable molecule, so a high activation energy is necessary to reduce it to organic compounds. By using photocatalysts, light can be employed to drive the reaction more efficiently than it would be possible with heat. The photocatalyst can absorb incident light and generate an electron hole pair, where the excited electron is used to drive the reduction of CO_2 . Metallic nanoparticles are known to be photocatalytically active themselves, but often exhibit short lifetimes for excited carriers. Pairing such a metallic NP with a semiconductor can drastically extend the electron's lifetime. [42]

As a semiconductor that is nontoxic, reactive, and easy to produce, TiO_2 has gained a lot of attention as a catalytic material. Already in 1972, studies on "Electrochemical photolysis of water at a semiconductor electrode" demonstrated promising catalytic properties of TiO_2 [12]. It has been of great interest for catalysis ever since. However, it was quickly realized that TiO_2 as a material on its own is limited due to the wide band gap in the UV range (3.0 – 3.2 eV) [31]. With the UV part only making up about 5 % of the solar energy [37], the idea of combining TiO_2 to with other materials to broaden the absorption range quickly arose. Metallic nanoparticles (NPs) have proven to be auspicious. Due to their plasmonic properties, which depend on material, shape, and environment, the absorption bands of these nanoparticles can span the majority of the visible range. Metallic NPs also exhibit photocatalytic properties themselves, but the short lifetime of their excited carriers makes it difficult to drive reductions efficiently. Injecting an excited electron from the metal into the semiconductor conduction band (CB), however, can drastically increase the lifetime of an excited charge carrier. Without any holes in the valence band (VB) and a potential barrier to the metallic NP, the quick recombination of injected electrons via the usual recombination channels is inhibited. The combination of gold nanoparticles (Au NPs) with TiO_2 to enhance absorptive or photocatalytic properties has since become very popular.

Ratchford et al. determine the total injection efficiency of Au NPs submerged in layers of anatase TiO_2 in ref. [28], finding injection efficiencies up to 45 %. To study the injection efficiency, they use transient infrared absorption spectroscopy (TIRAS), which is a pump-probe method. A pulsed femtosecond (fs = 10^{-15} s) laser is used to first excite (pump) the sample. Then, a probe pulse is used to measure the changes in the absorption behavior caused by the previous excitation. This method allows for a high temporal resolution by changing the delay of the pulses with respect to each other via a mechanical delay stage.

The fundamental idea of the experiment is sketched in fig. 1a). First, a so-called "hot electron" is produced by exciting it high above the Fermi level using the pump energy $\hbar\omega_{\text{pump}}$. With $\lambda_{\text{pump}} = 585\text{nm}$, the pump energy is not sufficient to overcome the band gap directly, as shown in fig. 1b). Therefore, the pump beam only interacts with the gold nanoparticles. If a hot electron crosses the Schottky barrier ϕ_B , that naturally forms upon contact between a metal and a semiconductor, it can be probed

1 Introduction

by exciting intraband transitions. For the excitation of intraband transitions, IR is well suited [27], therefore, the probe wavelength was set to $\lambda_{\text{probe}} = 5 \mu\text{m}$. Since the gold particles do not produce a signal in response to the probe beam, as also shown in fig. 1b), the change in absorption ΔA of the probe beam can be directly attributed to the number of electrons in the conduction band due to electron injection.

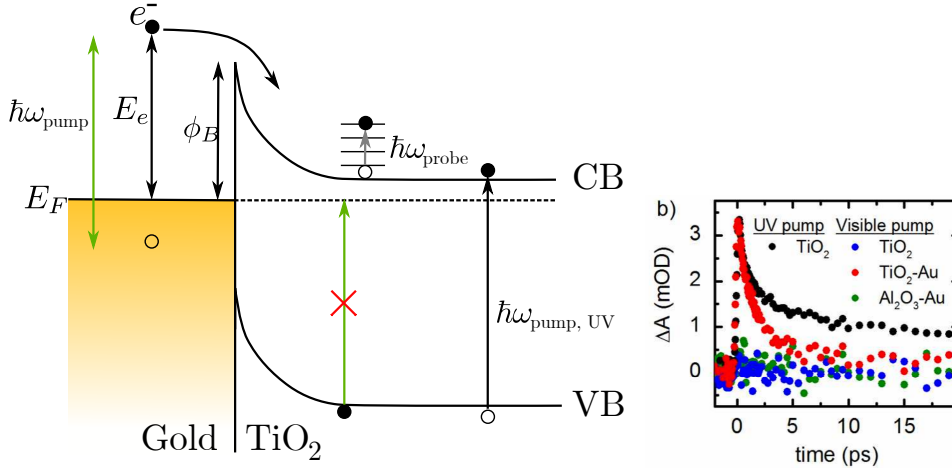


Figure 1: a) Schematic of the charge carrier injection process that is investigated with pump-probe spectroscopy. The green arrows represent the pump energy. It is sufficiently high to excite an electron over the Schottky barrier ϕ_B but not to excite an electron over the semiconductor's band gap. To directly excite an electron over the band gap, UV light (black arrow) is necessary. The gray arrow represents the probe energy, which is used to excite intraband transitions. b) Transient absorption measurement of Au NP&TiO₂ with a visible pump beam and an IR probe beam (red). Control measurements were conducted to show that Au NPs do not absorb the IR probe beam (green), and that TiO₂ NPs do not absorb the visible pump beam (blue). Therefore, the change in absorption is proportional to the number of electrons injected into the TiO₂ conduction band. Exciting the semiconductor over the band gap with a UV pump beam produces a signal, which Ratchford et al. used to calculate the injection efficiency for visible pump wavelengths. Figures (adapted) from ref. [28].

To determine the injection efficiency, the maximum signal strength ΔA_{\max} of the transient signal is measured as a function of the absorbed photon density. A linear relationship is found. When the measurement is repeated for pure TiO_2 under UV excitation and IR probe, ΔA_{\max} behaves linearly as well. Assuming the “injection efficiency” is 100 % for over the gap excitation of pure TiO_2 , the injection efficiency of the mixed sample can be calculated from the ratio of the slopes.

With this method, Ratchford et al. determine the injection efficiency to be up to 25 – 45 % , depending on the pump wavelength.

Ostovar et al. measure a similar injection efficiency of 44 % in ref. [26]. However, they go a step further and investigate the different underlying electron injection processes. Two main charge transfer mechanisms at metal-semiconductor interfaces have been identified: direct and indirect (plasmon-mediated) charge transfer. Ostovar et al. use gold nanorods coated with a TiO_2 shell to separate the contributions of both processes by employing different measurement techniques. First, they utilize single-particle dark-field scattering spectroscopy to identify the efficiency of direct charge transfer through the broadening of the plasmon linewidth. Afterwards, they use transient infrared absorption spectroscopy on these particles to determine the overall injection efficiency. With a total efficiency of 44 %, the direct charge transfer is responsible for about half the injections (19 %).

These results appear to be promising, but it is unclear how far these results can be generalized. In particular, the popular combination of Au NPs with the commercially available P25 TiO_2 has not been studied. Moreover, it is unclear why these high transfer rates do not translate to similarly high reactivities.

The goal of this thesis is therefore to establish a TIRAS setup in the UDKM labs and test it on P25 TiO_2 NPs. Size quantization effects due to using TiO_2 NPs instead of the previously mentioned films should not play a role for particles with a diameter $d > 2$ nm [31]. If similar injection efficiencies could be obtained, this kind of sample could be produced in large quantities more easily, posing an advantage for possible future applications.

To guide the reader through the underlying concepts and the conducted experiments, the background section will provide a brief overview regarding metal- and semiconductor interface physics as well as the pump and probe processes that are used for the transient absorption spectroscopy. Furthermore, this work will supply a detailed discussion concerning the working principles and setup of Non-collinear Optical Parametric Amplifiers (NOPAs), which are used to generate both visible and IR fs-pulses. Subsequently, the conducted experiments and their adaptation to various unforeseen obstacles will be elaborated on.

2 Background

2.1 Metal- and semiconductor interface physics

2.1.1 Schottky barrier at metal semiconductor interface

Metals and semiconductors can be distinguished by the position of the Fermi energy within the band structure. The highest completely filled band will be referred to as the valence band (VB) and the lowest partially occupied or unoccupied band as the conduction band (CB). Metals have their Fermi level within the conduction band, so that the conduction band is always partially filled with electrons. Because the valence band of an intrinsic semiconductor (SC) is completely occupied while its conduction band is empty, a semiconductor's Fermi level is located within the band gap. For illustration, compare to fig. 2 I (metal) and II (SC); the shaded areas represent occupied electronic states. The occupation of the VB and CB can be modified by so-called "doping", which refers to the introduction of foreign atoms into the semiconductor crystal lattice. Doping shifts the position of the Fermi level within the band gap towards the dopants' energy levels. Introducing atoms with an additional electron to the lattice is called n-doping. Since less energy is necessary to delocalize these additional electrons (=excite them into the conduction band), the Fermi level shifts towards the conduction band. The opposite is true for p-doping, which adds holes to the valence band.

Considering a metal and a semiconductor separately, both have material specific Fermi energies E_F . The respective vacuum energies E_{vac} , which are the energies electrons possess just after entering the vacuum due to ionization, align in thermodynamic equilibrium. The work functions $\phi_{\text{m/SC}}$ describe the energy that is necessary to ionize an electron from the respective Fermi level. Since the Fermi energy cannot be occupied in a semiconductor because it is within the band gap, the electron affinity χ_{SC} is defined to describe the energy necessary to ionize an electron from the CB minimum.

When bringing the two materials in contact, however, the Fermi levels need to align in order to reach thermal equilibrium. In thermal equilibrium, the minimization of the system's energy is aspired. Therefore, the electron configuration shifts in order to occupy the lowest possible energetic states until the Fermi levels are aligned. Considering the metal - n-type SC interface forming for materials like in fig. 2, the semiconductor has a higher Fermi level. Upon contact, it needs to lower in order to align with the metal Fermi level. This is realized by transferring charges from the donor states or conduction band to the metal. While lowering the SC's Fermi level, the metal contains orders of magnitude more free electrons so that its Fermi level is barely affected [9, p. 215-217]. Due to the charge transfer in the interface region, a depletion zone develops. The transferred electrons leave the interface region slightly positively charged which causes free electrons to accumulate at the metal side of the interface. This depletion zone is equivalent to the creation of a potential barrier, which is indicated by band bending (fig. 2 III). For a metal-SC interface, this potential barrier is called the Schottky barrier ϕ_B .

Figure 2 illustrates the creation of a Schottky barrier for $\phi_{\text{m}} > \phi_{\text{SC}}$. Reversing this relation, e.g. by considering p-doped SCs, would lead to band bending in the opposite direction.

2 Background

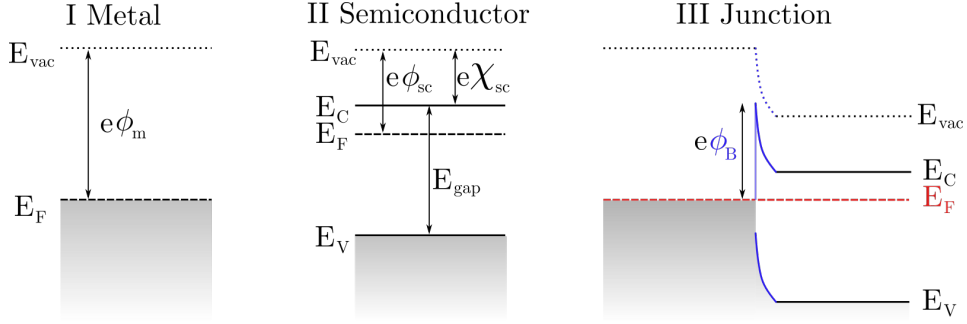


Figure 2: Formation of a Schottky barrier at the interface between a metal and a semiconductor. I) The metal has its bands filled with electrons up to its Fermi energy E_F , which lies within the conduction band. ϕ_m denotes the metal work function, which is the energy necessary for an electron to reach the vacuum energy E_{vac} from the Fermi level. II) The semiconductor has its valence band filled with electrons up to the valence band maximum at E_V . Since E_F lies in the band gap with energy E_{gap} where no states can be occupied, the conduction band is only occupied by either thermal electrons or electrons from donor states. The SC's work function is denoted with ϕ_{SC} , and the electron affinity as χ_{SC} . χ_{SC} is defined by the energy that is necessary to excite an electron from the conduction band minimum to E_{vac} . III) When metal and SC are brought into contact, the Fermi levels align (red, dashed line) through charge transfer at the interface. This causes the creation of an electrostatic potential. At the interface, vacuum levels need to align as well, which leads to band bending (blue) in the SC as the material specific values χ_{SC} , ϕ_{SC} , and E_{gap} need to remain constant throughout the material. Figure adapted from ref. [9].

This description of the Schottky barrier formation is also known as the Schottky-Mott model. Following the Schottky-Mott rule, the Schottky barrier height (SBH) is determined by the metal work function ϕ_m and the (n-type) semiconductor's electron affinity χ_{sc} (eq. 1) [22].

$$\phi_B = \phi_m - \chi_{sc} \quad (1)$$

Even though this rule predicts band bending at the interface correctly, the height of the barrier ϕ_B is often not predicted correctly when comparing this rule to experimental measurements of the SBH. Since this model is a pure electrostatic consideration of perfect crystals, the neglect of interface states and interface chemistry is a certain cause for its failure in prediction.

2.1.2 Other interface models

First experimental data on the SBH revealed a rather weak dependency of the SBH on the metal work function compared to the expected strong linear dependence. The missing dependency of the SBH became known as “Fermi level pinning” (FLP). To attempt an explanation, attention was drawn to interface effects. When atoms at interfaces of the involved materials interact with each other - possibly forming molecular orbitals - this creates states different from the usual bands, often located in the band gap. When bringing both materials in contact, charge transfer can also occur due to rearrangements of the electron configuration of interacting atoms, introducing an additional “interface dipole” eD_{int} .

Reports in literature studying FLP, determined the SBH as a function of the metal work function. Applying a linear fit to the data resulted in a slope S that diverges from the Schottky-Mott model expecting a slope of 1. Since the failure of the Schottky-Mott model was attributed to the neglect of interface interactions, S was defined to be the “interface behavior parameter”. It depends on D_{int} and is supposed to “describe the semiconductor’s ability to screen out external (metal) influences” [36]. Semiconductors with a small S -parameter would be influenced strongly by the neighboring metal. Nevertheless, finding the correct origin for the screening ability was still a challenge as various properties, such as ionicity, polarizability or dielectric constant, might be contributing to this behavior simultaneously. Subsequent experiments also uncovered an inhomogeneity in the FL position at the interface and therefore of the SBH, especially with polycrystalline samples. This suggests, that previous measurements might have just returned an average over an actually inhomogeneous SBH, also explaining why measurements of the same sample structure returned a wider variance in results depending on preparation methods. An inhomogeneity is a direct contradiction to a “pinned” Fermi level.

At the same time a second effect, also referred to as “Fermi level pinning” was investigated. It describes the pinning of the Fermi level in the band gap at an interface/surface of a semiconductor due to charge neutrality conditions. Since a charged surface would not comply with energy minimization, electronic states of the surface have to differ from the bulk band structure. Dangling bonds and defects lead to (bands of) electronic states within the band gap that are occupied so that the surface is electrically neutral, effectively pinning the FL in the gap. John Bardeen suggested the “fixed separation model” to treat both FLP phenomena. His model proposes that charge transfer between metal and SC surface states can rectify the difference of the respective work functions. To avoid modifications of the interfaces

2 Background

due to contact, he introduces a very thin dielectric- or gap layer between metal and SC, not considering their respective interaction with the dielectric layer.

Another origin of the gap states was proposed to be the tail of Bloch waves of the metal that decay into the semiconductor, creating so-called “metal induced gap states” (MIGS). When complying with charge neutrality condition, this model results in a similar description as published by Bardeen. Even though MIGS also has some rather obvious flaws as a model (charge transfer to gap states might not be possible when the state itself is created by the charge being present in the metal), the model has become popular as a ground for discussing SBH data

In conclusion, numeric calculations or experimental determination of the SBH are necessary for reliable results. For the combination of Gold and TiO₂ nanoparticles, the Schottky barrier height is between 0.9 and 1.3 eV [24, 19].

For illustrative purposes, the Schottky-Mott model will remain the reference picture for further considerations. Both Ratchford and Ostovar chose this model to outline their experiments as well [28, 26].

2.1.3 Electron transfer processes

The exact process of electron injection has not yet been fully understood. Possible pathways for an electron to enter the conduction band of a semiconductor are generally divided into either direct or indirect mechanisms [21, 26].

The indirect transfer is based on Fowler’s internal photoemission. Fowler developed this theory in the 1930s, describing the emission of an electron from a metal, a so-called “emitter”, into an adjacent material, a so called “collector”. Following this theory, the internal photoemission proceeds in three steps. First, a hot electron is excited via photon absorption by the emitter. Then, the electron is transported to the interface. Finally, the electron can cross the potential barrier at the interface but only if it has enough momentum perpendicular to the interface [11]. Due to this process, the internal photoemission or indirect transfer is also known as “over the barrier transfer”. To quantify the electron yield, the empirical relation eq. 2 emerged

$$Y_{\text{Fowler}} \propto (\hbar\omega - \phi_B)^2 \quad (2)$$

where $\hbar\omega$ is the photon energy [16]. This relation matches experimental results well, considering the order of magnitude and spectral response [20]. The electron can either be excited directly through the absorption of a photon or via the decay of a plasmon as indicated in fig. 3 a). A plasmon is the collective oscillation of free electrons in a metallic nanoparticle (LSPP), that can decay into a hot electron-hole pair (see fig. 4). The relevant plasmonic decay processes will be described in more detail in sec. 2.2.1. Note that the indirect process was chosen to represent carrier injection in fig. 1a).

However, the injection efficiency based on this simple equation is limited to only 1 % [11], which is much lower than experimentally observed later on. Ostovar et al., for example, found injection efficiencies caused by indirect electron transfer of about 20 % [26]. Considering a metal structure whose dimensions approach the electron mean free path, scattering effects can enhance the injection efficiency. Nevertheless, optimistic estimations still did not exceed 10 %, indicating that the simple equation neglects important aspects.

The direct charge transfer mechanism assumes that upon excitation, an electron enters the conduction band of the semiconductor directly without having to cross

the barrier. A hole is also generated in the metal and remains there. Interfacial charge transfer (IFCT) postulates that the mixing and coupling of semiconductor and metal states at the interface permit the direct generation of an electron in the CB and a hole in the metal, as displayed in fig. 3 b). Plasmon induced charge-transfer transition (PICTT) is the plasmonic counterpart of IFCT. During this process, a plasmon decays by directly exciting an electron in the conduction band and a hole in the metal, see fig. 3 c). [21]

There is no consensus regarding the exact details of the direct charge transfer. Different variations are discussed. Current hypotheses either assume that the excited electron enters the conduction band after briefly occupying an interface state or that the electron is directly generated in the SC conduction band without occupying any other states previously. [21, 41]

Regarding Ostovar's results, chemical interface damping (CID), which is a subset of the direct excitation mechanisms, was responsible for 19% of the total injection efficiency of about 44% [26].

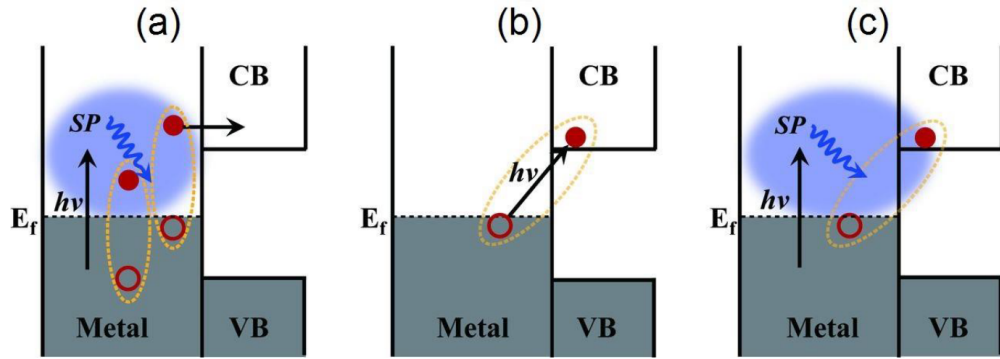


Figure 3: Possible pathways for charge carrier injection of an electron from a metal into a semiconductor's conduction band (CB). a) indirect transfer: the hot electron is created as consequence of plasmon decay (or through the absorption of a photon) and enters the CB only with enough energy to overcome the potential barrier, and if spatially close by. b) interfacial charge transfer (IFCT): the electron is directly excited into the CB via interface states. c) PICTT (plasmon induced charge transfer transition): this is the plasmonic equivalent of IFCT, where an excited plasmon decays by creating an electron directly in the CB. Figure from ref. [21].

2.2 Transient measurement of Au - TiO₂ charge transfer

2.2.1 Visible pumping of Au

When considering the TiO₂&Au NP system, one needs to select a suitable wavelength to excite electrons high above the Fermi level in the Au NPs, as sketched in fig. 1. This can be achieved either by exciting the interband transition from the 5d to the 6p band, or by exciting the plasmon resonance of the metallic nanoparticle, which results in the creation of a hot electron as well. Since the latter excitation was the modus operandi of the discussed literature in the introduction and the initial goal of the measurement, a brief overview will be given. However, the necessary wavelength for this excitation was not available at the time of the experiments. Therefore, all measurements within this work were conducted with a 400 nm pump beam that rather corresponds to interband transitions, as discussed subsequently.

Electron excitation by plasmon decay When metallic nanoparticles are resonantly excited with light of a wavelength much larger than the particles themselves, a so-called “plasmon” can be excited. A plasmon is a quasi-particle that refers to the collective oscillation of free electrons within the nanoparticle. Plasmonic excitations are well known for electromagnetic field enhancement properties, that are, for example, used for spectroscopy on single molecules. However, the plasmon itself has a rather short lifetime of ≤ 100 fs, after which it decays in multiple steps [43]. Figure 4 shows a schematic of the decay processes with their respective timescale. After the oscillation of the electrons (fig. 4a)), the plasmonic energy is redirected to generate excited electron-hole pairs via Landau damping (fig. 4b)). Depending on the electron’s relative position to the Fermi energy before excitation, the electron can be excited up to $\hbar\omega_0$, the total incidence photon energy, above the Fermi energy. This creates a highly non-thermal electron distribution, which can either decay radiatively or non-radiatively. During radiative decay, the electrons and holes simply recombine and emit their energy as a photon. For non-radiative decay, the excited (“hot”) electrons partake in electron-electron scattering processes, leading to a thermal electron distribution. For gold, this process happens within about 1 ps of the plasmon excitation. On a longer timescale of a few nanoseconds, energy is transferred from the electrons to the lattice by electron-phonon scattering. Electron and phonon temperatures equilibrate and energy is slowly dissipated to the surrounding environment (fig. 4c)).

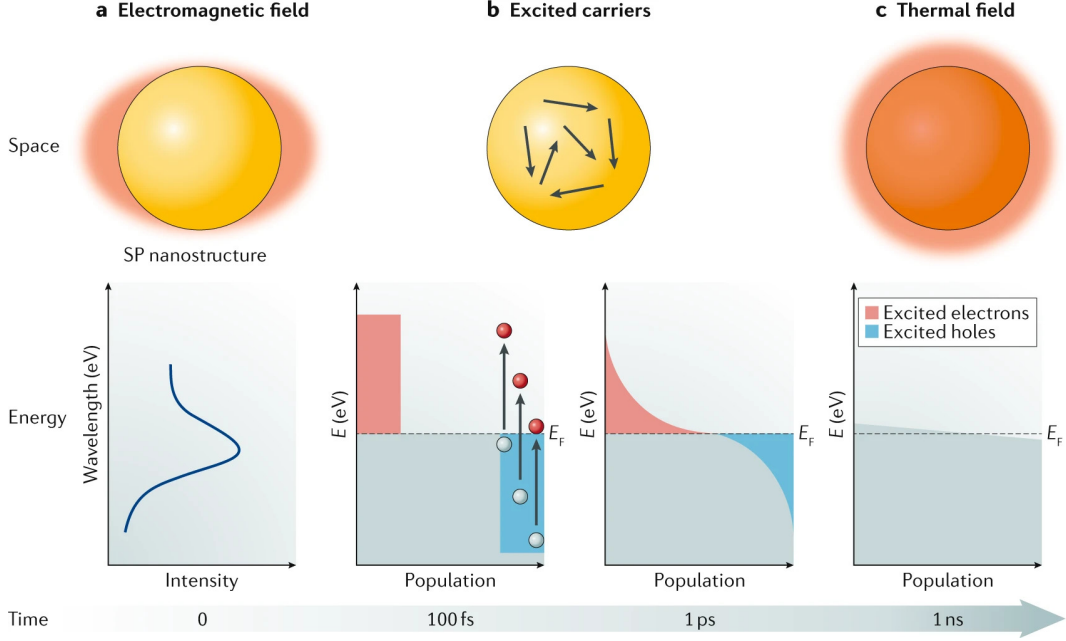


Figure 4: Decay process of a plasmon. a) A plasmon is excited by an external electromagnetic field. The collective oscillation of electrons with the external field leads to an enhancement of the external field near the poles of the spherical NP. b) Landau damping creates hot electron-hole pairs with a non-thermal energy distribution. Through electron-electron scattering, a thermal electron distribution is reached. c) Electrons transfer their energy to the lattice by electron-phonon scattering. Figure from ref. [43].

For spherical nanoparticles, the Fröhlich condition in eq. 3 can be used to determine the plasmonic resonance. It takes the particle's material and the environment into account.

$$\varepsilon_{\text{sph}} = -2\varepsilon_{\text{med}} \quad (3)$$

ε_{sph} is the (real part of) the dielectric function and ε_{med} is the dielectric function of the medium surrounding the particle. For TiO₂ as a surrounding medium with a refractive index of $n_{\text{TiO}_2} \approx 2.5$, the resonance position for spherical gold nanoparticles is expected to be at about 600 nm. This was reproduced experimentally by Ratchford et al. in ref. [28]. Since the particles in the samples at hand are not fully coated in TiO₂, slight deviations are expected.

Exciting the plasmon resonance would require a pump beam with a visible wavelength. As discussed in section 3, a visible NOPA setup was at hand, but due to instabilities of the fundamental laser, measurements could not be conducted with its output.

Instead, 400 nm, which is easy to realize experimentally by non-linear second harmonic generation, will be used for pumping.

Interband transitions The 400 nm pump pulses are supposed to excite interband transitions in the Au NPs. 400 nm correspond to an energy of 3.1 eV. Looking at the band structure of gold as depicted in fig. 5a) and b), interband transitions from the 5d to the 6p can be excited at the X- and L point. These transitions would only require about 1.8 eV and 2.3 eV respectively, being well below the maximum available

2 Background

energy provided by the pump beam. However, these transitions only correspond to an excitation to the Fermi level. To inject an electron from gold into TiO_2 , the excitation energy has to be sufficient to excite the electron above the Schottky Barrier $\phi_B \approx 1.2 \text{ eV}$, so 1.2 eV above the Fermi level. The band structure at the L point does not meet this condition. To reach an electronic state $\geq 1.2 \text{ eV}$ above the Fermi level, a second interband transition to the 6s band would be necessary which exceeds the available energy by far.

At the X point, a direct transition from the 5d to an excited state in the 6p band $\geq 1.2 \text{ eV}$ above the Fermi level is possible. Of course, both transitions can occur, but due to the SBH, the transition at the X-point is expected to be the main source of electrons injected from Au into TiO_2 when pumping with 400 nm .

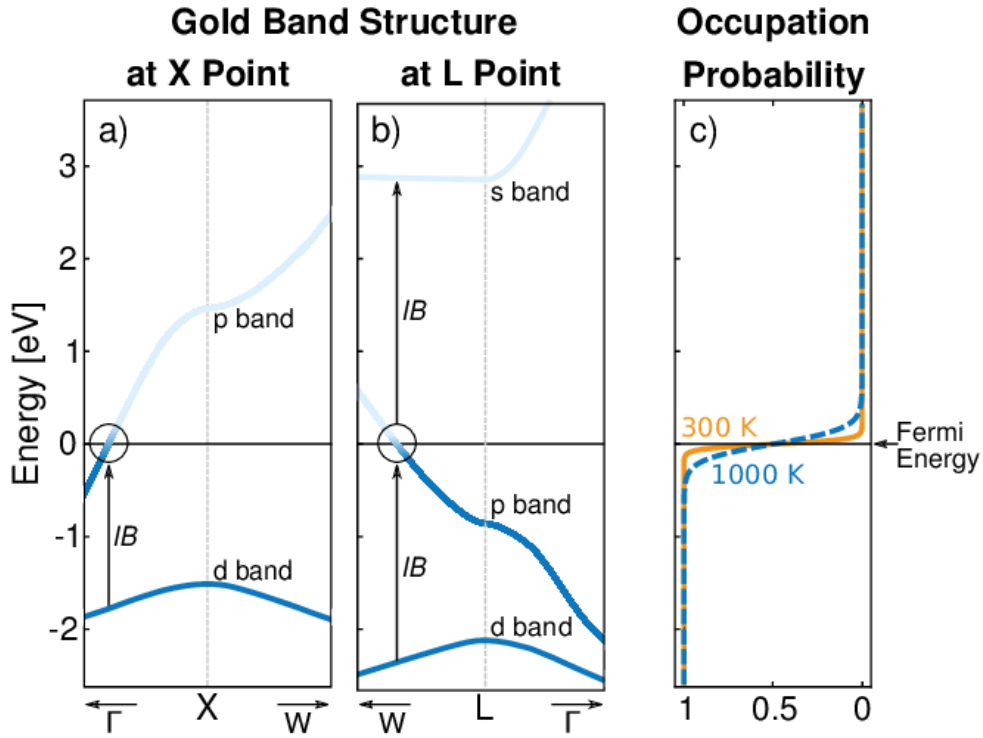


Figure 5: Band structure of gold at a) the X point and b) the L point. Dark blue represents occupied states, whereas light blue indicates unoccupied states. The lowest bands of the band structure are the 5d bands. Interband (IB) transitions from the 5d to the 6p band are possible both at the X point and at the L point. A consecutive IB transition from the 6p to the 6s band could be excited at the L point. c) displays the Fermi-Dirac distribution for room temperature (orange) and a higher temperature of 1000 K (dashed blue). The Fermi-Dirac distribution describes the occupation probability of electronic states depending on the temperature of the system. For higher temperatures, the occupation of the electronic states around the Fermi level is smeared, because some electrons occupy states above the Fermi level leaving some states at the Fermi level or below empty. The smearing is indicated by the color gradient in a) and b). Figure from ref. [34].

2.2.2 IR probe of TiO₂

After a successful charge transfer process, the electrons are relocated to the conduction band of the semiconductor. The barrier initially prevents the electron from direct back transfer. Moreover, the absence of holes in the SC valence band also prevents efficient recombination, providing the electron with a long life time.

In this thesis, electrons in the conduction band of TiO₂ are probed by infrared (IR) absorption. As demonstrated by Panayotov et al., electrons at energies close to the conduction band edge of TiO₂, effectively absorb IR photons by phonon-assisted intraband transitions [27]. Due to the lack of other sources of IR absorption [28, 26, 13], the absorption signal of TiO₂ in the low energy region is therefore proportional to the number of charges in the conduction band.

Panayotov et al. investigated the absorption behavior for wavelengths between 4500 nm and 10000 nm. The strongest absorption was measured for the longest wavelength of 10000 nm. Both the groups around Ratchford and Furube used shorter wavelength of 5000 nm and 3500 nm to probe the number of injected carriers, still obtaining good signals [28, 13].

Within this thesis, a probe wavelength of 2200 nm will be used, since the detection range of the available spectrometer is limited to 2500 nm.

2.2.3 Deviations due to visible absorption in TiO₂

Up to now, we have considered a system based on a TiO₂ anatase single crystal and an ideal TiO₂-Au interface. In a more realistic system, several deviations have to be taken into account.

The commercially available P25 TiO₂ particles, which are used to prepare the samples for this thesis, also contain 20% rutile TiO₂. Unlike anatase, which has a band gap of $E_{\text{gap}} = 3.18$ eV, the rutile phase has a direct band gap of $E_{\text{gap}} = 3.03$ eV [10]. Pumping the TiO₂&Au NP sample with 400 nm will therefore likely excite the TiO₂ directly as well.

An additional problem might be caused by a large amount of trap states: semiconductors' optical properties are usually defined by their band structure and, more importantly, by their band gap. Considering a perfect crystal, it only absorbs light with sufficient energy to cross the band gap. However, the bands (and the gap between them) are calculated based on a perfect, infinite lattice. When the lattice is neither perfect nor infinite, additional states ensue that are located within the band gap. Since these states are more localized than the quasi-free states in the conduction band, they are also called trap states. Due to the large surface-to-volume ratio, surface and defect states play a more significant role when it comes to the semiconductor nanoparticles compared to bulk materials. The additional states change the optical properties of the semiconductor slightly, since it is possible for the electron in the band gap states to reach the conduction band with less than the band gap energy. To not completely change the optical properties, however, it is important to keep the number of defects and surface states relatively small compared to the atoms that follow the correct lattice structure.

Impurities can be divided into two categories: shallow and deep traps. Shallow traps can result from point defects. They are generated when an atom with a different number of valence electrons replaces a lattice atom. TiO₂ is commonly known as an n-type semiconductor, meaning additional electrons are introduced into the structure. The additional electrons are not part of the crystal bonding, but

2 Background

are (due to screening effects) weakly bound to their atomic core. Since they are only weakly bound, it only takes a small amount of energy to delocalize such an electron, which is equivalent to lifting the electron from its dopant state in the band gap into the conduction band. Oftentimes, room temperature already provides enough thermal energy to overcome the binding energy and lift a portion of the dopants into the conduction band. When an atom with fewer valence electrons is placed in the lattice, a hole is introduced to the valence band. Since conduction is also possible via holes, both processes work analogously.

Shallow traps can also be caused by surfaces and interfaces. Here, the lattice periodicity is interrupted, leading to different microscopic potentials. When the lattice is interrupted, the last row of atoms cannot partake in the usual binding processes. When two materials are brought into contact but are in thermodynamic equilibrium, an electric potential is created to match the potentially different Fermi levels at the interface, causing the SC bands to bend. A similar process happens at a surface to ensure a neutral charge of the surface, which is obligatory due to energy minimization principles. The position of the shallow traps within the bandgap can experimentally be determined by far-infrared absorption spectroscopy or temperature dependent conductivity measurements.

When the periodicity or crystal symmetry is disturbed within the lattice, e.g. through gaps from missing atoms or atoms on interstitial sites, deep trap states form. These states are more strongly localized and belong to eigenstates that are not described by Bloch functions. Deep traps are located ≥ 1 eV underneath the conduction band minimum for n-doped semiconductors. Deep traps can also alter the properties of a semiconductor by limiting its carrier lifetime.

This short overview on trap states is based on ref. [35], which also provides more details for the interested reader.

Taking the various additional trap and interface states into account, pump-probe spectroscopy is not as distinct regarding the excited transitions as proposed by Ratchford et al.. Instead of only interacting with the Au NPs, the 400 nm pump beam can directly excite the semiconductor, either over the band gap or by exciting electrons from or into trap states. The probe beam can also be absorbed by shallow trap states [27], which might detract from the direct correlation between the number of electrons in the CB and the absorption strength. For relaxation processes, the trap states will play a major role as well. With a high enough density of trap states, trap-assisted Auger recombination as well as the usual trap-assisted decay might be possible. The high number of trap states might also significantly reduce the lifetime of electrons in the CB, but this is to be investigated. Charge back transfer from the CB to the Au NP either over the barrier for electrons with enough energy or via tunneling might also be possible. Even though no control measurements could be made due to the lack of a suitable sample with a very high Schottky barrier, it is still assumed that the electrons in the Au NPs do not interact with the probe beam. Figure 6 provides a schematic overview over the possible pump, probe, and decay processes.

2.2 Transient measurement of Au - TiO₂ charge transfer

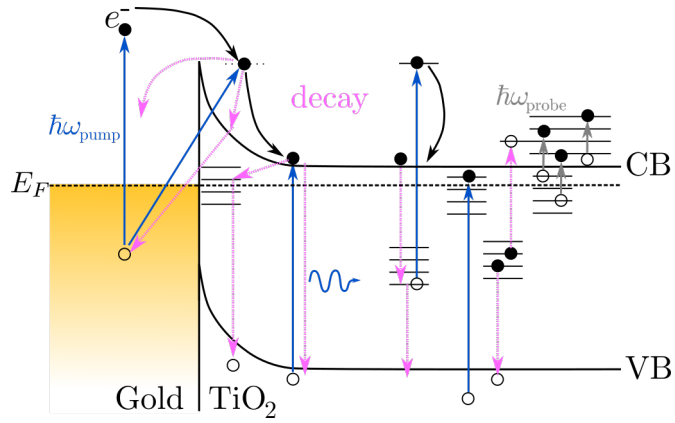


Figure 6: Overview over possible pump (blue), probe (gray) and decay (pink) mechanisms for our TiO₂&Au NP system. Due to the smaller band gap of rutile, a direct excitation of TiO₂ with the 400 nm pump beam is feasible. Various trap states provide additional options for excitation decay processes.

3 NOPA-NOPA transient IR absorption spectroscopy

To study the dynamics of a sample after an excitation that causes a non-equilibrium state, transient absorption spectroscopy can be a powerful tool. Depending on the chosen wavelength for the experiment, different transitions and dynamics can be addressed. For the investigation of electron dynamics, for example, very short timescales must be reached in order to resolve ultrafast phenomena. For that reason, femtosecond (fs) lasers are usually employed for this kind of experiment.

When using fs lasers, a welcome side effect of the extremely short pulses is high peak intensities, which allow for the application of nonlinear optics. **Non-collinear Optical Parametric Amplifiers (NOPAs)** employ various nonlinear processes to convert a fundamental (input) wavelength into another wavelength. Here we employ a two-stage NOPA to generate femtosecond IR pulses, which are subsequently used to probe the free carriers in TiO_2 .

This chapter outlines the basic function of a pump-probe spectroscopy setup. Since two NOPAs are integrated into the setup, the second subsection will explain the nonlinear processes on which the NOPA principle is based. Finally, the third subsection will describe the setup's components and their functions in more detail.

3.1 Transient absorption spectroscopy setup

To reach the desired time resolution to resolve ultrafast dynamics, a pulsed fs laser is split into so-called “pump” and “probe” parts. The pump beam excites the sample, whereas the probe pulse reaches the sample with an adjustable time delay, which is typically realized through a mechanical stage. The probe pulse interacts with the sample and is measured with a spectrometer. By comparing the interaction of the probe pulse with the unpumped versus the pumped sample, the influence of the excitation on the system can be monitored. Changing the delay between pump and probe pulses then allows for the observation of the sample dynamics at each set delay, comparable to a flip-book. This method is mostly referred to as transient absorption spectroscopy, even though in this case a change in transmission is measured.

3 NOPA-NOPA transient IR absorption spectroscopy

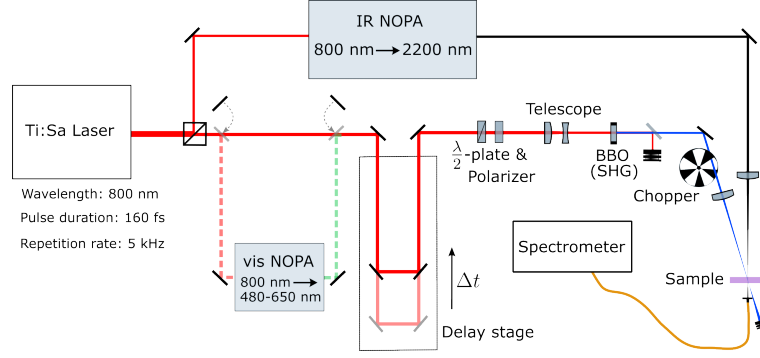


Figure 7: Schematic of the transient absorption spectroscopy setup. The fundamental laser with a central wavelength of $\lambda_{\text{central}} = 800 \text{ nm}$, a repetition rate of $\nu_{\text{rep}} = 5 \text{ kHz}$, and a pulse duration of about $\tau_{\text{pulse}} = 160 \text{ fs}$, is split into two parts. While the upper part is led through an IR NOPA setup to obtain the probe beam with a wavelength of $\lambda_{\text{probe}} = 2200 \text{ nm}$ (illustrated with a black line), the lower part is used as the pump beam. The pump path provides three options: I) the beam is used with the laser’s fundamental ($\lambda_{\text{pump}} = 800 \text{ nm}$). The path follows the solid red line, where the beam is guided over a mechanical delay stage. With the $\lambda/2$ -wave plate and the polarizer, its power can be adjusted. From here, it can either continue with $\lambda_{\text{pump}} = 800 \text{ nm}$ or II) a BBO crystal on a flip mount can also be used to generate the second harmonic, so that the pump wavelength is $\lambda_{\text{pump}} = 400 \text{ nm}$ (illustrated with the blue solid line). As a third option, III), the fundamental pump beam can be diverted from its standard path in the beginning and coupled into a vis-NOPA setup via a flip mirror (dashed red line) where it can be converted into (any) visible wavelength. The output (preferably green: $\lambda_{\text{pump}} = 530 \text{ nm}$) can then be coupled back onto the standard pump path with another flip mirror (dashed green line). From there, I), II) and III) follow the same path which leads through a chopper and a focusing lens before reaching the sample. At the sample position, a spatial overlap between pump and probe must be established. After passing through the sample, the probe beam is coupled into a spectrometer that is synchronized with the chopper, making it possible to differentiate between pumped and unpumped sequences. With the delay stage that either of the pump beams has passed, a variable time delay Δt can be introduced between the pump and the probe pulses at the sample, providing the desired time resolution.

This setup specifically uses a titanium:sapphire (Ti:Sa) laser as a fundamental laser that creates 160 fs pulses with a repetition rate of $\nu_{\text{rep}} = 5 \text{ kHz}$ and a central wavelength of $\lambda_{\text{central}} = 800 \text{ nm}$ via chirped pulse amplification (CPA). The “MaiTai” (MT) oscillator creates 800 nm pulses with a repetition rate of $\nu_{\text{rep,MT}} = 80 \text{ MHz}$ and a spectral width of about 9 nm. These pulses are guided into the “Spitfire” regenerative amplifier, where the pulse length is stretched (chirped), reducing peak intensity, before entering a second cavity with another Ti:Sa crystal as the active medium. The crystal is pumped by the “Ascend” continuous-wave laser with $\lambda_{\text{Ascend}} = 530 \text{ nm}$. Only one femtosecond light pulse from the oscillator enters the cavity at the same time, with entry and exit of the pulse being controlled by Pockels cells. Therefore, their settings also determine the number of circulations of the pulse in the cavity. All

3.2 Nonlinear optics: why intensity is important

other pulses are discarded, which therefore changes the repetition rate from $\nu_{\text{rep,MT}}$ to ν_{rep} . After exiting the cavity, the pulses are then recompressed by a grating compressor to compensate for the chirp introduced earlier, leaving the pulses both intense in power and short. The Spitfire output beam is split into pump and probe beams with a ratio of about 0.9. An IR NOPA (non-collinear optical parametric amplification) setup converts the 800 nm pulses to $\lambda_{\text{probe}} = 2200$ nm. The pump beam is guided over a mechanical delay stage to set the time delay Δt , and through a $\lambda/2$ -plate and a polarizer to adjust the pump power. With either the visible NOPA setup before the stage or a BBO (β -barium borate, $\text{Ba}(\text{BO}_2)_2$) crystal and a reflective filter, the pump wavelength can be converted to $\lambda_{\text{pump}} = 480 - 650$ nm or $\lambda_{\text{pump}} = 400$ nm respectively. Both the pump and the probe beam are then focused onto the sample. For comparing pumped- to unpumped signals, the pump pulse passes through a chopper before it reaches the sample. The chopper's blades rotate with a frequency of $\nu_{\text{chop}} = 125$ Hz, so that a few pulses in a row can pass before the blade blocks the next few pulses. The exact number of pulses depends on the width of the blades. Behind the sample the ‘‘Avantes AvaSpec NIR256-2.5-HSC’’ spectrometer monitors the transmission T of the probe beam. Since the spectrometer is synchronized with the chopper, it can ascribe the measured signals to pumped or unpumped intervals. These can be used to calculate a relative change in transmission $\frac{\Delta T}{T_0}$ from the raw data:

$$\frac{\Delta T}{T_0} = \frac{T_{\text{pumped}} - T_{\text{unpumped}}}{T_{\text{unpumped}}}$$

Measuring absorption would require accounting for scattering and reflection, which is rather complicated and not feasible with the present setup. In consequence, all measurements will be made in transmission mode. To characterize the pump beam on the sample, a beam sampler on a flip mount is installed about 10 cm before the sample. It diverts a fraction of the pump beam towards a beam profiling camera, that is installed perpendicular to the sample, but at the same distance. With a known pump power, the fluence at the sample position can be determined. The camera also enables the monitoring of the beam profile, which is circular with a Gaussian profile at optimum.

Since the NOPAs are essential (and sensitive) parts of the setup and experiments and a lot of time during the master thesis was invested in optimizing the NOPAs, their underlying nonlinear processes and working principles will be discussed in more detail in the following.

3.2 Nonlinear optics: why intensity is important

In solid-state physics, the polarization \vec{P} is a key property, as it describes the influence of an electric field \vec{E} on a material. When an electric field is applied to an atom, the positively charged core and the negatively charged electrons move in opposite directions, effectively creating a dipole. In a dielectric material the microscopic dipoles create an overall polarization. How strongly the core and electrons are displaced by electric field is described by the susceptibility χ , which is material-specific.

In linear optics, the polarization can be described by

$$\vec{P} = \epsilon_0 \chi^{(1)} \vec{E} \quad (4)$$

where the polarization is directly (**linearly**) proportional to the electric field. This

3 NOPA-NOPA transient IR absorption spectroscopy

is true for sufficiently small/weak \vec{E} . In the linear regime, however, it is impossible to convert one wavelength into another. Since this is the main goal of the NOPA setup, a closer look at the nonlinear regime is necessary. Generally speaking, the polarization can be expressed as a series expansion of the electric field, making it possible to define separate polarization contributions that go with different orders of the electric field [3]

$$\vec{P} = \epsilon_0 \left(\chi^{(1)} \vec{E} + \chi^{(2)} \vec{E}^2 + \chi^{(3)} \vec{E}^3 + \dots \right) := \vec{P}^{(1)} + \vec{P}^{(2)} + \vec{P}^{(3)} + \dots \quad (5)$$

where ϵ_0 is the vacuum permittivity (constant) and $\chi^{(i)}$ is the susceptibility tensor of the i -th order. Already the second order polarization $\vec{P}^{(2)}$ allows for second harmonic generation (SHG). Inserting $\vec{E}(t) = \vec{E}e^{-i\omega t}$ into the expression for $\vec{P}^{(2)}$ yields

$$\begin{aligned} \vec{P}^{(2)} &\sim \chi^{(2)} \vec{E}^2(t) \\ &= \chi^{(2)} \left(Ee^{-i\omega t} + c.c. \right) \left(Ee^{-i\omega t} + c.c. \right) \\ &= \chi^{(2)} 2EE^* + \chi^{(2)} \left(E^2 e^{-i2\omega t} + c.c. \right) \end{aligned}$$

So the second order polarization produces a static term (which is not a contribution to light emission for a monochromatic beam, but is known as the optical rectification) and a term that contains double the fundamental frequency 2ω . The latter causes the generation of second harmonic radiation. Optical parametric amplification is a $\vec{P}^{(2)}$ process as well and can be derived in a similar fashion as SHG, but of course starting with two different frequency components ω_1 and ω_2 . [32]

White light generation (WLG) requires an additional order of polarization, making it a $\vec{P}^{(3)}$ process. WLG is based on the (temporal) optical Kerr effect, often referred to as self-phase modulation. The effect becomes relevant when a medium is exposed to pulsed light with high peak intensities. The high intensities cause the refractive index to become intensity dependent. Considering a Gaussian pulse shape, the intensity of the pulse varies with time. Therefore, the refractive index is not only intensity but also time dependent. This means, each part of the pulse experiences a different refractive index when passing through the medium.

But how can the refractive index become intensity dependent in the first place? Optical properties like the refractive index n and the dielectric function ϵ are linked to the susceptibility via equation 6.

$$n = \sqrt{\epsilon} = \sqrt{1 + \chi} \quad (6)$$

Factoring out the electric field once and defining the remaining terms of the sum as a nonlinear susceptibility χ_{NL} results in an expression for the nonlinear polarization \vec{P}_{NL} (eq. 7) which exhibits the same structure as the linear polarization in eq. 4.

$$\vec{P}_{\text{NL}} = \epsilon_0 \left(\chi^{(1)} + \chi^{(2)} \vec{E} + \chi^{(3)} \vec{E}^2 + \dots \right) \vec{E} = \epsilon_0 \chi_{\text{NL}} \vec{E} \quad (7)$$

Following eq. 6, the nonlinear refractive index is then

3.2 Nonlinear optics: why intensity is important

$$\begin{aligned}
n_{\text{NL}} &= \sqrt{1 + \chi_{\text{NL}}} \\
&= \sqrt{1 + \chi^{(1)} + \chi^{(2)} \vec{E} + \chi^{(3)} \vec{E}^2 + \dots} \\
&= \sqrt{1 + \tilde{\chi}^{(1)} + \tilde{\chi}^{(2)} (\vec{E}) + \tilde{\chi}^{(3)} (\vec{E}^2) + \dots} \tag{8}
\end{aligned}$$

where $\tilde{\chi}^{(i)}$ is a function of the electric field to the $i - 1$ power. Now, assuming the third order nonlinearity is relatively small, the nonlinear refractive index n_{NL} as a function of $\tilde{\chi}^{(3)}$ according to eq. 8 can be expanded to a Taylor series. Note that the rewriting of $\chi^{(i)} \vec{E}^{i-1} \rightarrow \tilde{\chi}^{(i)} (\vec{E}^{i-1})$ is purely done to simplify the expression for the Taylor expansion. Due to symmetry arguments, the susceptibility is zero for all even orders.

$$\begin{aligned}
n_{\text{NL}} (\tilde{\chi}^{(3)}) \Big|_{\tilde{\chi}^{(3)}=0} &\approx n (\tilde{\chi}^{(3)} = 0) + n' (\tilde{\chi}^{(3)} = 0) \cdot (\tilde{\chi}^{(3)} - 0) \\
&= \sqrt{1 + \chi^{(1)} + \chi^{(2)}} + \frac{1}{2\sqrt{1 + \chi^{(1)} + \chi^{(2)}}} \tilde{\chi}^{(3)} (\vec{E}^2) \\
&= \sqrt{1 + \chi^{(1)}} + \frac{1}{2\sqrt{1 + \chi^{(1)}}} \tilde{\chi}^{(3)} (\vec{E}^2) \\
&= n_0 + \frac{\chi^{(3)}}{2n_0} \cdot \vec{E}^2 \\
&= n_0 + n_2 I
\end{aligned}$$

This derivation results in an intensity dependent term of the refractive index. n_0 denotes the “normal” (linear) refractive index, whereas n_2 is defined as the nonlinear part of the refractive index whose contribution increases with intensity.

Due to $I \propto \vec{E}^2$, the intensity dependent refractive index exhibits a Gaussian profile as well when a laser pulse with a Gaussian envelope (eq. 9) propagates through the medium.

$$E(t, z) = E_0 e^{-\frac{t^2}{2\tau^2}} e^{i(\omega_0 t - kn_{\text{NL}} z)} = E_0 e^{-\frac{t^2}{2\tau^2}} e^{i\phi_{\text{NL}}} \tag{9}$$

The instantaneous frequency $\omega(t)$ of the electric field can be defined as the variation of the phase $\phi(t)$ over time [8, 30, 17]. Because the phase depends on the nonlinear refractive index, which in turn depends on time, the instantaneous frequency changes with time, as outlined in figure 8.

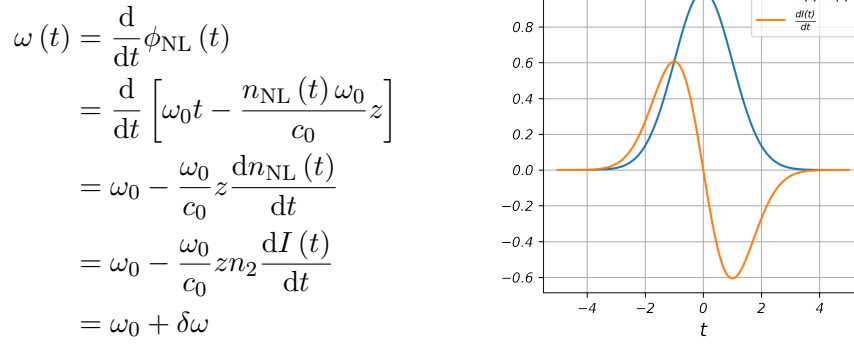


Figure 8: Left: Instantaneous frequency for a time dependent nonlinear refractive index. Since the refractive index depends on the time profile of the pulse, the instantaneous frequency causes a broadening of the initial spectrum by $\delta\omega$. Right: Gaussian intensity profile of a light pulse. The profile is transferred to the nonlinear refractive index (blue). The instantaneous frequency is proportional to the negative derivation of the Gaussian temporal profile (orange).

A variation of the instantaneous frequency with time is also associated with chirp, which means that the frequencies within the pulse are shifted against each other time.

3.3 Visible NOPA

As previously mentioned, a **Non-collinear Optical Parametric Amplification (NOPA)** setup converts an input wavelength into another by using a combination of the nonlinear processes motivated in the prior section. When aiming at the conversion to a visible (vis) wavelength, only one non-collinear amplification step is necessary. Figure 9 displays the corresponding setup. The main advantage of this setup is the adjustability of the output wavelength once the NOPA is well calibrated for broadband use. This makes NOPA setups unique and very useful.

The amplification over a broad range of visible wavelength requires three nonlinear processes: white light generation (WLG), second harmonic generation (SHG), and (the non-collinear) amplification process, which is essentially a stimulated difference frequency generation (DFG). The second harmonic is used to pump the amplification crystal, providing the energy for the DFG process, while the WL is used to select the output energy by stimulating the process. Nonlinear processes all depend on intensity, therefore, a telescope is mounted before the actual NOPA setup the adjust the beam diameter and henceforth control the intensity (power per area).

The telescope consists of two lenses L1 and L2. Lens L2 is a concave lens with a focal length of $f_{L2} = -f_{L1}/2$, choosing the appropriate focus lengths can adjust the beam diameter while keeping the beam collimated. The beam is then coupled into the NOPA using the apertures A1 and A2. Part of the incoming beam is branched off by a beam sampler to generate white light with the components M4 to L4, while the rest is used to pump the amplification process.

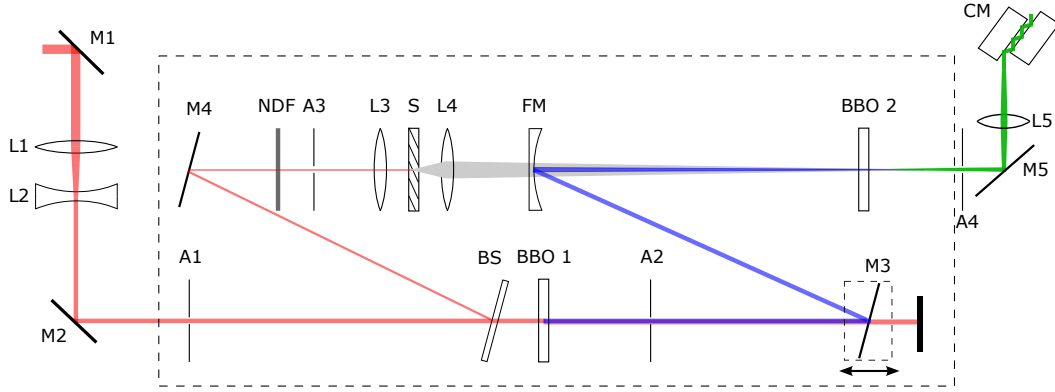


Figure 9: Setup sketch of the vis-NOPA. The incoming beam diameter is adjusted by a telescope (lenses L1 and L2) before entering the NOPA (dashed lines). A beam sampler (BS) is used to provide some intensity from the fundamental beam for white light generation (elements M4-L4). The remaining fundamental is used for SHG to create a 400 nm pump beam. With the moveable mirror M3, the temporal overlap between the pump and white light can be adjusted. Additionally, mirrors M3 and FM are dichroic, filtering out the remaining 800 nm that were not converted. With the focusing mirror FM, which is positioned at a reduced height, the pump beam is focused into BBO2 at an angle from below. In BBO2, a spectral fraction of the seed light selected by the BBO2 angle and the position of mirror M3 amplifies the output wavelength in the visible range. The output is recollimated with L5. Through the amplification processes, a chirp is introduced to the pulse, which is roughly compensated by a pair of chirped mirrors. A: aperture, M: mirror, L: lens, BS: beam sampler, BBO: β - Barium-Borate crystal, NDF: neutral density filter, S: sapphire plate, FM: focusing mirror, CM: chirped mirror. Figure adapted from [18].

3.3.1 White light generation

To generate WL as per section 3.2, the lens L3 is used to focus the beam into a sapphire plate S where the WLG process takes place. The generated WL and remaining fundamental are collimated with the lens L4. When setting up the WLG path, an alignment tool is used to ensure that the beam follows a straight path that leads to the desired position of the WL in the amplification crystal (BBO2). The beam splitter (BS) and mirror M4 are used to set the beam path by adjusting on the tool marking at two different distances (use instead of apertures). When the

beam path is adjusted correctly, aperture A3 and lens L3, which are glued together, are inserted into the path. The beam is supposed to pass straight through aperture A3 and not be diverted by the lens. Again, the alignment tools are helpful for checking that the lens does not divert the beam. In this setup, aperture A3 seems not to be glued to the center exactly. While mounting the combined parts, the beam either did not pass the center of aperture A1 or its direction was changed by lens L3. Before inserting the sapphire plate, it is important position the adjustable neutral density filter (NDF) so that only a little intensity can pass through. The Sapphire plate is then inserted behind the focus of lens L3. With aperture A3 almost closed, the focus of lens L3 is moved toward the sapphire plate. If no WLG can be observed on a business card behind the sapphire plate, then the NDF should be adjusted to pass slightly more intensity, repeating the insertion process of the sapphire plate S as described before until a continuum is produced. The optimal stability is achieved when slightly more than the minimal possible intensity generates the output. Aperture A3 can be opened a little further, but should not be completely open. Since the WL generation is highly dependent on the beam's intensity, the edges of a Gaussian beam profile would be most prone to cause instabilities through slight intensity fluctuations. Therefore, aperture A3 is used to create a top-hat profile. Since lens L3 has a short focal length, the beam quickly diverges without lens L4 for collimation. Lens L4 is inserted in the same manner as lens L3, so that the beam stays on path. After proper alignment, the WL should be symmetrical. If this is not the case, the beam splitter BS and mirror M4 can be used for fine-tuning, while lenses L3 and L4 can be used to keep the beam on path.

3.3.2 Generating the pump beam from SHG

To generate the pump light that later provides the energy for the amplification process, second harmonic generation (SHG) is used. It is a degenerate version of the sum frequency generation (SFG) processes where two photons with the frequencies ω_1 and ω_2 are combined to a photon with frequency ω_3 . For SFG or DFG processes with three photons involved, the highest frequency ω_3 is often referred to as “pump” frequency ω_p due to historical notation. The next lower frequency ω_2 can be denoted as “signal” frequency ω_s and the lowest frequency ω_1 as “idler” frequency ω_i . SHG now describes the special case of $\omega_1 = \omega_2$ (see section 3.2), so that $\omega_3 = 2\omega_1$. For a fundamental wavelength of $\lambda_1 = 800$ nm, this means a conversion to $\lambda_3 = 400$ nm.

However, when generating a second frequency, both energy and momentum conservation has to be satisfied in order to get a sufficient output. For photons moving through a medium, the momentum is defined as

$$\vec{p} = \hbar\vec{k}, \quad (10)$$

$$\text{with } |\vec{k}| = \frac{2\pi}{\lambda} = \frac{\omega n(\omega)}{c_0} \quad (11)$$

where c_0 is the vacuum speed of light. In general, the refractive index $n(\omega)$ depends on the light's frequency. Therefore, when waves with different frequencies ω_1 and ω_3 propagate through a medium, there is usually a momentum mismatch $\Delta k = \vec{k}_3 - \vec{k}_1$. The mismatch also becomes apparent when considering the phase velocity $v_{\text{ph}} = c \cdot n(\omega)$ of light propagating through a medium. When two photons with ω_1 , that share the same phase and direction, generate a photon with $\omega_3 = 2\omega_1$,

the photon with ω_2 inherits the phase and direction. Due to $n(\omega_1) \neq n(\omega_3)$, the phase velocities differ. Propagating through the medium, the fundamental beam creates more harmonic photons in the same way but at different points in time or space. Each of them will also inherit the fundamental's phase but that will have a rather random relationship to the previously generated photons phases. Therefore, destructive interference occurs, annihilating the SHG frequency (compare to fig. 10a)). To achieve constructive interference, leading to an SHG output, the phase velocities of both waves have to match (see fig. 10b)). Phase- and momentum matching are equivalent in this context.

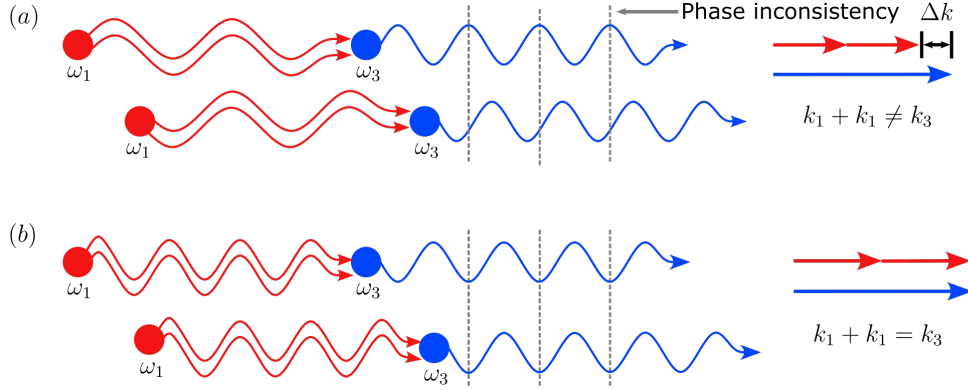


Figure 10: Illustration of phase matching for SHG (collinear). (a) displays a phase mismatch $\Delta k = k_3 - 2k_1 \neq 0$ between ω_1 and ω_3 . Photons with frequency ω_3 generated at different points in time do not have the same phase as already generated ω_3 - photons. Due to the different phase velocities, destructive interference is observed. (b) shows perfect phase matching $\Delta k = k_3 - 2k_1 = 0$. All photons share the same phase and phase velocity. Therefore, constructive interference of the generated photons with ω_2 emerges. Figure adapted from [7].

Phase matching conditions are fulfilled when eq. 12 is true.

$$\Delta \vec{k} \stackrel{!}{=} 0 \quad (12)$$

For SHG in a collinear geometry, eq. 12 is equivalent to 13. With the expression for k from eq. 10, the condition in eq. 14 arises for phase matching.

$$k_3 = 2k_1 \quad (13)$$

$$\begin{aligned} \frac{\omega_3 n(\omega_3)}{c_0} &= 2 \frac{\omega_1 n(\omega_1)}{c_0} \\ \omega_3 n(\omega_3) &= 2\omega_1 n(\omega_1) \\ n(\omega_3) &= n(\omega_1) \end{aligned} \quad (14)$$

Considering equations 13 and 14, phase matching as an equivalent for momentum conservation is formally derived. When the momenta are matched, the phase velocities, and hence the phases of the light fields, are matched as well.

To get the same refractive index for different frequencies, birefringence is necessary.

3 NOPA-NOPA transient IR absorption spectroscopy

Uniaxial, birefringent materials have an ordinary and an extraordinary refractive index, n_o and n_e . In three dimensions, the refractive index can be illustrated as an ellipsoid. Two axes have the same length n_o and the third one has a different length of n_e . Depending on whether the extraordinary axis is longer or shorter, the birefringence $\Delta n = n_e - n_o$ corresponds to a positive or negative value, respectively. Figure 11 displays an index ellipsoid for a negative birefringent material, such as β -BBO.

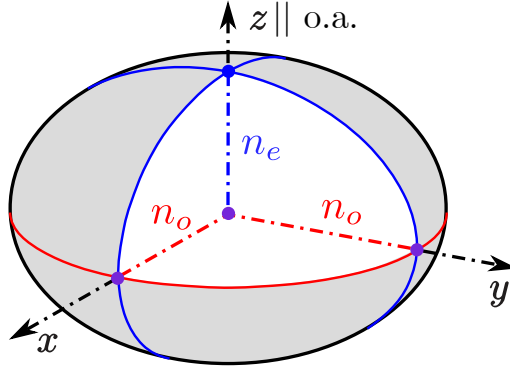


Figure 11: Index ellipsoid of an uniaxial, negative birefringent crystal ($n_e < n_o$). Depending on the orientation of the incident light relative to the optical axis (o.a.), the light experiences a varying refractive index. Light coming in parallel to the o.a. only experiences the ordinary index of refraction n_o . Light propagating perpendicularly to the optical axis experiences the extraordinary index of refraction n_e . For an arbitrary angle θ between the propagation direction of the light and the optical axis, an effective refractive index $n_e(\theta)$ applies. Figure adapted from ref. [29].

Which axis is seen by the light then depends on the orientation of the beam to the optical axis and on the beam's polarization. Since light is a transverse wave, a beam with linear polarization propagating along the extraordinary axis always sees the ordinary refractive index.

When the polarization is in perpendicular to the optical axis, the refractive index is n_o . Parallel-polarized light sees n_e instead. Both refractive indices can be calculated as a function of the wavelength from the Sellmeier equations in eq. 15 [2].

$$\begin{aligned} n_o^2(\lambda) &= \frac{2.7366122 + 0.0185720}{\lambda^2 - 0.0178746} - 0.0143756\lambda^2 \\ n_e^2(\lambda) &= \frac{2.3698703 + 0.0128445}{\lambda^2 - 0.0153064} - 0.0029129\lambda^2 \end{aligned} \quad (15)$$

It is important to enter λ in μm to get the correct results. Note, that the parameters are empirical and might differ from source to source. If the light goes through the medium at an angle θ relative to the optical axis, both components are combined into an effective refractive index $n_e(\theta)$ (eq. 16).

$$\frac{1}{n_e^2(\omega, \theta)} = \frac{\cos^2(\theta)}{n_o(\omega)} + \frac{\sin^2(\theta)}{n_e(\omega)} \quad (16)$$

Depending on the polarization of the photons taking part in the process, there

are different types of phase matching. Within this setup, only type I is used. Type I phase matching refers to the processes where one photon of extraordinary polarization e is divided into or formed from two photons of ordinary polarization o or vice versa (see table 1). This classification is valid for both DFG and SFG processes, therefore, the relations work in both directions as indicated by the arrows in table 1.

| ω_1 (signal) | ω_2 (idler) | \leftrightarrow | ω_3 (pump) |
|---------------------|--------------------|-------------------|-------------------|
| o | o | \leftrightarrow | e |
| e | e | \leftrightarrow | o |

Table 1: Possible combinations of extraordinary (e) and ordinary (o) polarizations for photons taking part in a DFG (\leftarrow) or SFG (\rightarrow) process while fulfilling type I phase matching.

For this setup, the incoming beam has a horizontal polarization, implying that ω_1 experiences n_0 while propagating through the crystal. Following table 1, the generated pump ω_3 sees the (effective) extraordinary index of refraction $n_e(\theta)$. Since $n_0(\omega_1 = 800 \text{ nm})$ and $n_e(\omega_3 = 400 \text{ nm})$ are known from the Sellmeier equations 15, the effective refractive index $n_e(\omega_3, \theta)$ can be calculated for various angles θ between the propagation direction of the pump and the optical axis (o.a.), so that the phase matching condition from eq. 14 is fulfilled. Calculating the phase matching angle for various values of ω_1 results in an SHG phase matching curve of type I, displayed in figure 12. At each point of the curve, the refractive indices $n_o(\lambda_1)$ and $n_e(\lambda_3 = 400 \text{ nm}, \theta)$, and therefore the phase velocities of these waves, are equal. In case of two 800 nm photons creating a 400 nm photon, $\theta = 29.2^\circ$ ensures optimal phase matching conditions.

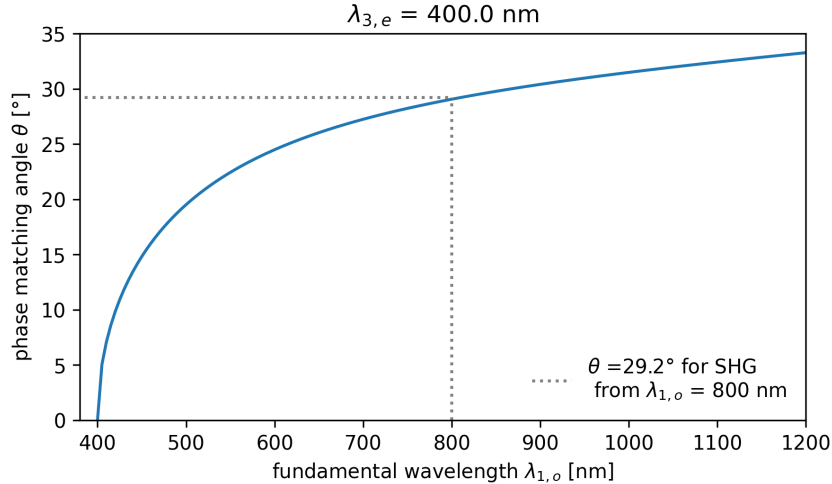


Figure 12: Phase matching curve for SHG calculated for type I phase matching ($o + o \rightarrow e$). The created wavelength $\lambda_{3,e} = 400 \text{ nm}$ has an extraordinary polarization and the fundamental wavelength $\lambda_{1,o}$ is ordinarily polarized. Eq. 16 gives leads to the phase matching angle θ as a function of the fundamental wavelength. A phase matching angle of $\theta = 29.2^\circ$ ensures perfect phase matching for SHG form $\lambda_{1,o} = 800 \text{ nm}$.

3 *NOPA-NOPA transient IR absorption spectroscopy*

Regarding the practical aspects, the conversion efficiency of the SHG process should be approximately 25 %. Higher efficiencies can produce undesired side-bands in the spectrum leading to WLG and crystal damage. Lower efficiencies provide fewer photons for the amplification process, reducing the output power. If the 25 % are not reached, the telescope (lenses L1 and L2, fig. 9) can be used to adjust the beam diameter. This changes the intensity on the BBO and can improve or impair the conversion efficiency. The unconverted intensity is filtered out through dichroic mirrors M3 and FM.

3.3.3 Amplification process

The amplification process in BBO2 is fundamentally a DFG process and therefore also a $P^{(2)}$ process. Unlike the SHG process, a pump photon of frequency ω_3 decays into a signal photon with ω_2 and an idler photon with ω_1 [3, ch. 2]:

$$\omega_2 = \omega_3 - \omega_1 \quad (17)$$

Every combination of frequencies that fulfills eq. 17 is allowed and the selection takes place spontaneously. To control the frequency output and produce a monochromatic, coherent beam, one can stimulate the process. By specifying the signal wavelength as an input that enters the crystal at the same time as the pump pulse, parametric conversion occurs: the pump photon decays via DFG with the fixed signal and corresponding idler wavelength (compare fig. 13a), and eq. 18).

$$\omega_3 + \omega_2 = (\omega_3 - \omega_2) + 2 \cdot \omega_2 = \omega_1 + 2 \cdot \omega_2 \quad (18)$$

The amplification then happens over the whole length of the crystal. The longer the photons propagate in the medium, the more signal photons are generated which can in turn stimulate more DFG processes. Therefore, the number of created signal and idler photons exponentially increases with the spatial coordinate x . The spatial coordinate is equivalent to the distance the photons propagated inside the crystal. Since a weak signal beam is already used as an input, the development of the signal amplitude $|A_s|$ is given by a $\cosh(z)$ function while a $\sinh(z)$ function describes the idler amplitude $|A_i|$ (compare fig. 13 (b)). A more formal, mathematical description can be found in [3, ch. 2].

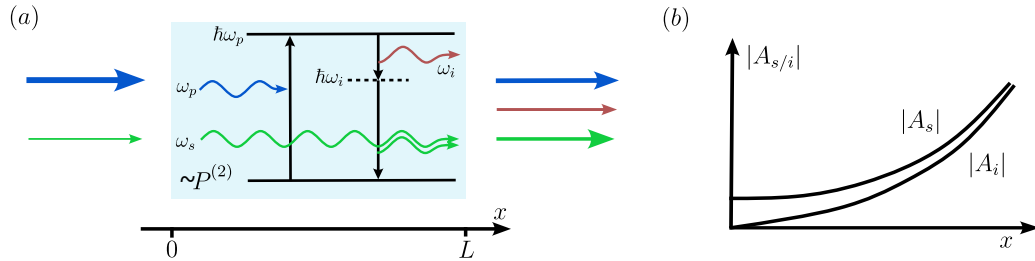


Figure 13: (a) The stimulated DFG process in a nonlinear medium, that results in the amplification of the input signal frequency ω_s . The pump frequency ω_p decays into a pair of signal and idler photons. By specifying the signal frequency through a weak input, the decay process can be stimulated to result in a second signal photon and the corresponding idler. This process occurs multiple times over the length of the crystal. The more it happens, the more signal (and idler) photons are capable of stimulating further decays. Therefore, the number of signal and idler photons, or the amplitude $|A_{s/i}|$ of the respective beam, rises exponentially as a function of propagation length x in the crystal, which is displayed in (b). Subfig. (a) adapted and subfig. (b) taken from ref. [3, ch. 2].

Because the amplified frequency depends on the incoming signal frequency, which can be varied, the process is called **parametric** amplification. Note: the phenomenon of parametric amplification originated from electric circuits but follows

the same principle for optics, explaining the term optical parametric amplification.

The phase matching is still of type I ($e \rightarrow o+o$), since the extraordinarily polarized pump decays into two ordinarily polarized signal and idler photons. But now that three different frequencies are involved in the process, the phase matching curve in fig. 12 is no longer applicable. Changing the geometry to make the beams non-collinear, as displayed in fig. 14, allows for phase matching conditions that hold for a broad range of visible frequencies.

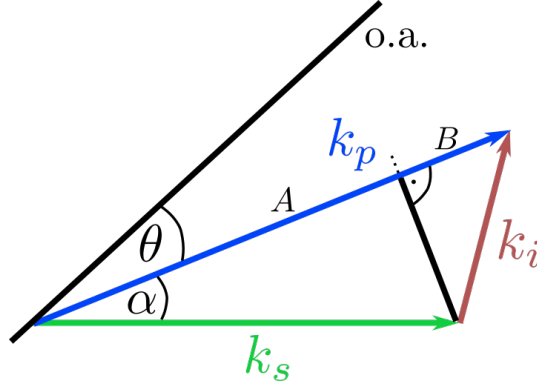


Figure 14: Sketch of the momentum vectors that are part of the DFG process. They are arranged in a non-collinear geometry so that the momentum mismatch is zero: $\vec{k}_p = \vec{k}_s + \vec{k}_i$. θ denotes the phase matching angle between \vec{k}_s and the optical axis (o.A.). α is the internal crossing angle between the pump- and signal beam. Basic geometry and trigonometry can be used to express the line segments A and B in terms of the vector lengths k_s , k_i and angle α so that phase matching is achieved, see eq. 20. A and B extend to the dashed line, adding up the length of k_p . Figure from ref. [39].

Again, phase matching is accomplished when eq. 12 holds, which is the same as

$$\vec{k}_p \stackrel{!}{=} \vec{k}_s + \vec{k}_i$$

Due to the geometry, the vectorial character cannot be neglected, but the vectors can be described via their length and angles with respect to each other. Following fig. 14, $|\vec{k}_p| = k_p$ can be dissected into two parts A and B that in turn can be expressed via k_s and k_i . A simply follows from trigonometric considerations. B is determined by using the Pythagorean theorem and a trigonometric expression for the perpendicular (black) line on B . Combining these leads to eq. 20, which is a parametric equation of the crossing angle α between the pump and the signal.

$$k_p = A + B \quad (19)$$

$$= k_s \cdot \cos \alpha + \sqrt{k_i^2 - (k_s \sin \alpha)^2} \quad (20)$$

Inserting equations 11 and 16 in the next two steps leads to the parametric equation in 21.

$$n_e(\omega_p, \theta) = \frac{k_s \cdot \cos \alpha + \sqrt{k_i^2 - (k_s \sin \alpha)^2}}{\omega_p} \cdot c_0$$

$$\left(\frac{\cos^2 \theta}{n_0^2(\omega_p)} + \frac{\sin^2 \theta}{n_e^2(\omega_p)} \right)^{-\frac{1}{2}} = \frac{k_s \cdot \cos \alpha + \sqrt{k_i^2 - (k_s \sin \alpha)^2}}{\omega_p} \cdot c_0 \quad (21)$$

Solving eq. 20 numerically for the phase matching angle θ and a few arbitrary values of α with $\lambda_p = 400$ nm results in the phase matching curves plotted in 15. This figure shows that a phase matching angle of $\theta = 31.2^\circ$ and an internal crossing angle of $\alpha = 3.7^\circ$ allow for broadband phase matching over almost the whole visible range of the spectrum.

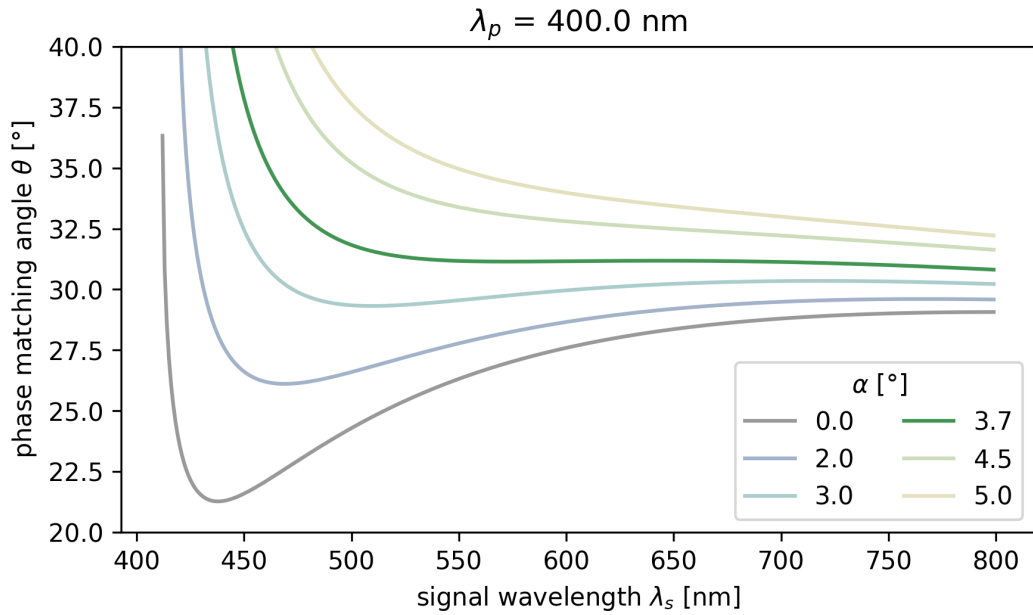


Figure 15: Numerically calculated phase matching curves for a DFG process in BBO with $\lambda_p = 400$ nm. The phase matching curves were calculated for six different internal crossing angles α . Broadband phase matching can be achieved with a phase matching angle of $\theta = 31.2^\circ$ and an internal crossing angle of $\alpha = 3.7^\circ$ (green curve).

Owing to the non-collinear geometry, the group velocities of signal and idler in the signal's propagation direction are matched as well. Therefore, the pulse does not undergo significant temporal broadening. More details on this effect can be found in the review by Cerullo et al., see ref. [6].

As a side note, the choice of parameters for the Sellmeier equation influences the phase matching curves. However, the influence is minuscule for the non-collinear geometry at $\alpha = 3.7^\circ$ and is only of consequence for signal wavelengths approaching the pump wavelength (see figure 16).

3 NOPA-NOPA transient IR absorption spectroscopy

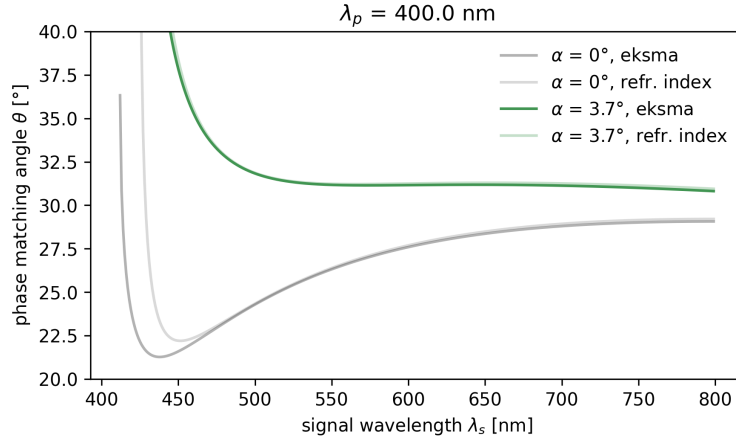


Figure 16: Difference in phase matching curves for different Sellmeier equation parameters (parameters for darker lines from ref. [2], transparent lines from ref. [25]). The parameters from ref. [2] were chosen to match the graphics in ref. [38].

The non-collinearity is achieved by lowering the height of focusing mirror FM, so that the pump beam reaches BBO2 from below while the signal beam propagates horizontally, see fig. 17a). Due to refraction, the calculated internal crossing angle between pump and signal of $\alpha = 3.7^\circ$ does not match the external crossing angle α_{ext} . The latter can be obtained through a few geometrical considerations and Snell's law. From fig. 15, it is known that $\theta = 31.2^\circ$ and $\alpha_{\text{int}} = 3.7^\circ$. The cutting angle of our crystal is $\theta_{\text{cut}} = 32.5^\circ$. With this, all angles can be determined by equations I) to VII) in fig. 17. Fig. 17a) displays an overview of the geometry of the amplification process with accurate angles, whereas b) and c) focus on the internal and external geometry, respectively.

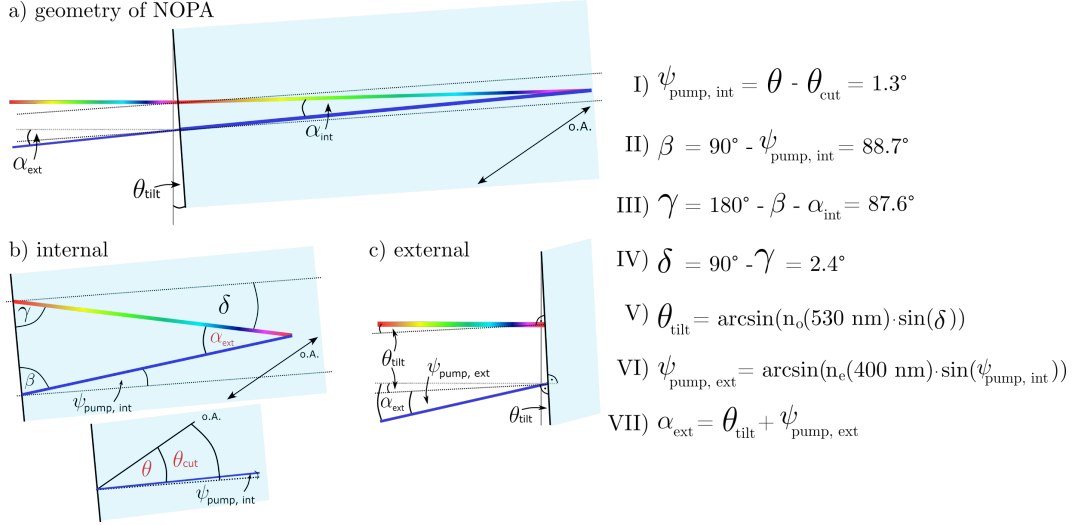


Figure 17: Subfigure a) displays the non-collinear geometry of pump and signal beam entering the BBO, taking refraction into account. The angles are displayed with exact proportions. Subfigures b) and c) focus on the geometry within, and outside of the crystal, respectively. For illustration purposes, the angles are not true to real proportions. Linking the equations on the right hand side to the figures, one first considers the internal geometry in subfigure b): I) calculates the angle $\psi_{\text{pump, int}}$ between the surface normal and the pump beam inside the crystal. The required phase matching angle $\theta = 31.2^\circ$ and the cut angle $\theta_{\text{cut}} = 32.5^\circ$ are fixed values (red); compare to the magnification in b). From this, the corresponding angles in eqs. II), III) and IV) can be calculated, assuming $\alpha_{\text{int}} = 3.7^\circ$ is fixed. Using Snell's law, eq. V) calculates the tilting angle of the crystal θ_{tilt} , which is illustrated in c). With the tilting angle, the angle between pump and surface normal on the external side, $\psi_{\text{pump, ext}}$ is determined through eq. IV). Finally, the external crossing angle α_{ext} results from eqs. VI) and VII). Figure adapted from ref. [40].

Entering all given values from the setup into equations I) - VII) leads to an external crossing angle of $\alpha_{\text{ext}} \approx 6^\circ$. With a little more geometry, the height of the pump beam on the FM necessary to get the correct α_{ext} can be calculated as a (linear) function of the distance between the focusing mirror FM and BBO2.

Since the phase matching does not pose a constraint over the visible range for the signal frequency, its selection is implemented through the temporal overlap. The necessity of a temporal overlap between signal and pump for stimulated (parametric) amplification can be exploited to make the output tunable over the visible range. By using a broad (strongly chirped) WL pulse as the signal beam and a short pump pulse, a specific frequency from the WL pulse can be selected to be amplified by adjusting the temporal overlap. The adjustment can be implemented quite easily by making the mirror M3 in the setup (see fig. 9) movable. By varying the distance of the pump pulse to the amplification crystal BBO2, a temporal delay Δt is introduced that allows the selection of the signal frequency. Fig. 18 illustrates this principle.

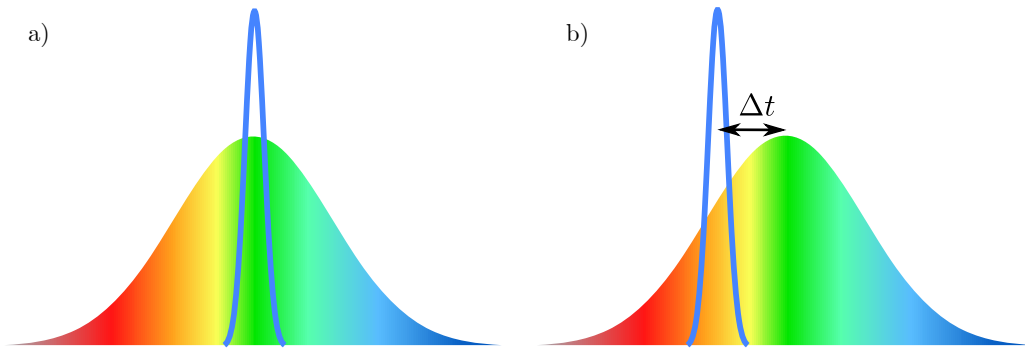


Figure 18: The overlap between the short pump pulse (blue contour) and the broad, chirped WL pulse (colored) determines the signal wavelength. The desired wavelength can be selected by introducing a time delay Δt between the pump pulse and the WL pulse. The delay is created by moving the mirror M3 either closer to or farther away from the amplification crystal BBO2. Subfigures a) and b) represent the selection of a green and orange signal wavelength, respectively.

3.3.4 Alignment steps

When aligning this part of the setup, the subsequently listed steps should be followed:

1. The WL has to be aligned so that the beam propagates parallel to the table. The height must match the height of the amplification crystal BBO2. The pump beam is blocked for this step.
2. The WL is blocked. After inserting the crystal into the beam path before the pump focus, it can be moved towards the pump beam focus slowly. The fluorescence cone's intensity should be visible with the bare eye, but when it gets too intense or even starts flickering, crystal damage might ensue. When the distance between focusing mirror FM and BBO2 is fixed, the pump beam height on the focusing mirror needs to be adjusted for the correct external crossing angle α_{ext} .
3. The optimal tilting angle θ_{tilt} for broadband amplification is set by adjusting the crystal's mount. The optimal position is found when all components of the fluorescence cone are closest together (compare to 19a) and b)).
4. After unblocking the WL, the mirrors M3 and FM are used to achieve an overlap between the WL and the pump beam inside the crystal, and between the WL and the fluorescence cone behind the crystal, see fig. 19c).
5. When there is no amplification yet, or not the desired frequency, the desired temporal overlap is achieved by adjusting the position of M3 with the delay stage (compare to 19d) and e)).
6. When spatial and temporal overlap are set successfully, the fluorescence cone depletes in favor of the amplification process. The spatial overlap usually requires fine-tuning. A power meter can be used for orientation. The mirrors M3 and FM are then adjusted until the power is maximized.

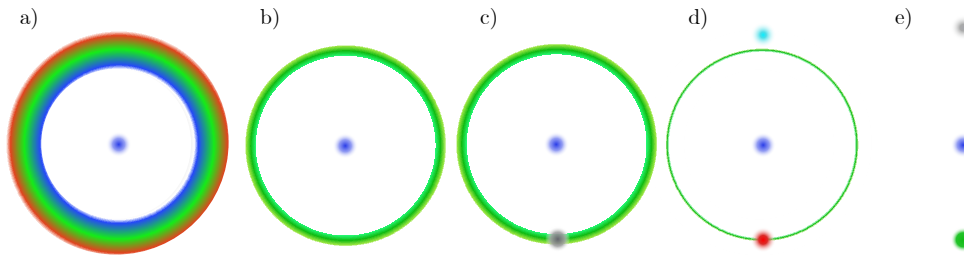


Figure 19: Illustration of the alignment steps for amplification in the visible range, optimized for green output. a) When the pump beam passes through BBO2, a fluorescence cone is generated. The various frequencies have different diameters, making the total cone broad. b) Tilting BBO2 to θ_{tilt} brings the diameters of the different frequency cones closer together until they overlap, optimizing the setup for broadband amplification. c) Spatial overlap between the WL and pump is created inside the crystal. The fluorescence cone and the WL need to overlap behind BBO2 for efficient amplification. d) Additional to the spatial overlap, temporal overlap between pump and WL beam inside BBO2 is created. Depending on what frequency component of the broad, chirped WL pulse overlaps with the pump pulse, different frequencies can be amplified. The amplification process depletes the fluorescence cone (d). The closer the amplified frequency is to the optimal frequency, the stronger the depletion (e).

After fine tuning, the first amplification setup is complete and the visible NOPA is operational. Since the WL signal is focused into BBO2, the beam diverges after the focus point. Therefore, a lens is placed after the output to recollimate the beam. An additional aperture is placed at the output to prevent back reflexes from entering the setup. The aperture can also be used to clip the beam profile if it contains unwanted features. A pair of chirped mirrors is used to shorten the pulse by counteracting the chirp of the output pulses of the NOPA. These mirrors work by offering different penetration depth for each frequency so that some of the frequencies have a slightly longer path and some have a slightly shorter path when being reflected from the mirrors. In order keep the beam on its original path, only an even number of reflections can be used. Therefore, the implementation of a prism compressor, which is not bound to discreet settings, would be useful for future experiments.

3.4 IR NOPA

Converting the fundamental wavelength of 800 nm to wavelengths in the (near) IR regime requires a second, collinear amplification step. The first amplification step works analogously to the visible NOPA described in sec.3.3. However, the infrared part of the WL seeds the first amplification stage, and the amplified idler propagates in the direction of the WL. The idler of the first step will also be used as the signal beam that seeds the second DFG process ($\lambda_{i,1} = \lambda_{s,2}$). Therefore, an even longer idler wavelength $\lambda_{i,2}$ is generated. All necessary phenomena to describe the second amplification step have already been introduced in the previous sections of this chapter. Therefore, this section rather focuses on the practical aspects of the setup.

The second amplification step can be added seamlessly to the first step, as displayed in the setup sketch of the IR NOPA in fig. 20. The only necessary change

3 NOPA-NOPA transient IR absorption spectroscopy

to the first step is to remove the blocking element behind the dichroic mirror M4 (M3 in the former setup sketch). This permits reusing the remaining intensity of the fundamental 800 nm after the SHG process. The remaining 800 nm are then used as the pump light for the second amplification step $\lambda_{p,2}$ (or $\omega_{p,2}$). After the first amplification step, the signal beam $\lambda_{s,2}$ is collimated using lens L5. With the filter F1, the WL which is a remnant from the prior pump process, is removed. The signal beam is then guided to BBO3, passing through the dichroic mirror M9 from the back. To stay with type I phase matching ($e \rightarrow o + o$), the pump $\lambda_{p,2}$ is sent through a $\lambda/2$ - wave plate to rotate the polarization by 90° ($o \rightarrow e$). Subsequently, the beam is directed towards BBO3 via the movable focusing mirror FM2. Both beams pass through another aperture A6 for alignment before reaching the crystal. Here, the DFG process described in sec. 3.3 creates and amplifies an even lower idler frequency $\omega_{i,2}$. Since all optical elements of the second step have the same height, the amplification step is collinear this time. This means all three frequencies follow the same path.

To obtain the desired output wavelength, all other wavelengths need to be chosen accordingly. Applying energy conservation, the correct signal wavelength $\lambda_{s,2}$ can be determined.

$$\begin{aligned} \frac{1}{\lambda_{p,2}} &= \frac{1}{\lambda_{s,2}} + \frac{1}{\lambda_{i,2}} \\ \Leftrightarrow \lambda_{s,2} &= \frac{1}{\frac{1}{\lambda_{p,2}} - \frac{1}{\lambda_{i,2}}} \end{aligned} \quad (22)$$

For later experiments, $\lambda_{i,2} = 2200$ nm was favored as a probe wavelength. Using eq. 22, the corresponding signal wavelength needs to be $\lambda_{s,2} = \lambda_{i,1} = 1257$ nm.

Since the wavelengths extend into the near infrared (nIR), BBO3 might be replaced by KTP, which has better transmission properties for wavelength up to 3000 nm. For further details, review ref. [1].

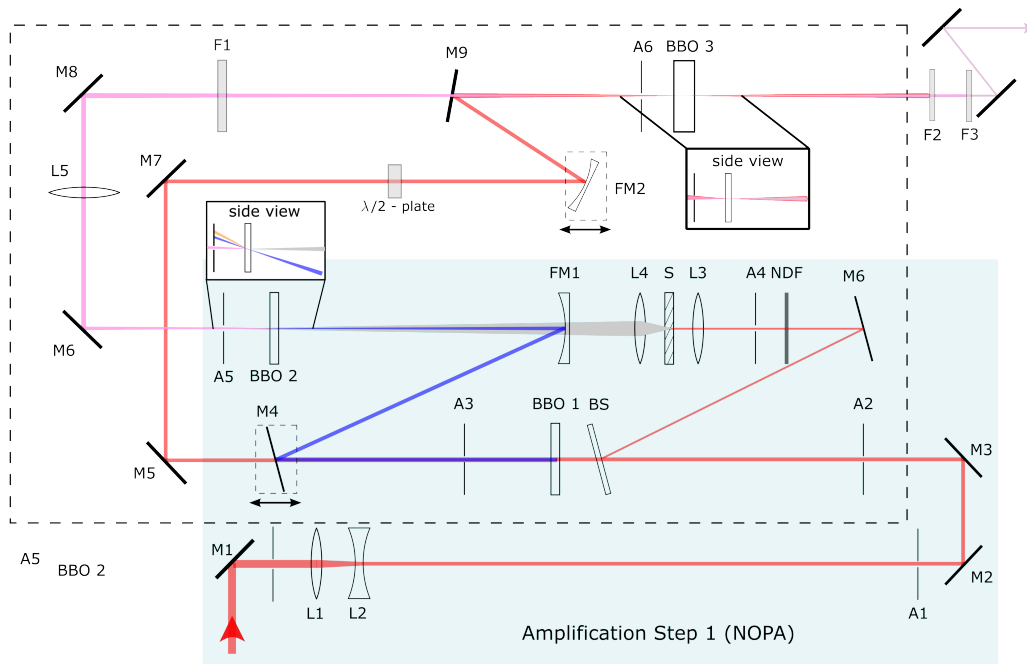


Figure 20: IR NOPA setup: after the first amplification step (highlighted in color), another collinear amplification step is added. It uses the remaining 800 nm from the SHG process as the pump beam. The idler of the first step is used seed the second amplification step. In the second step, it acts as the signal beam, because the DFG process creates an even lower energetic idler wavelength. After the second amplification step, the pump and signal beams are blocked or filtered from the collinear beam, so that the IR idler can be used as the sole output. The side views of the amplifications steps illustrate the different geometries for non-collinear and collinear amplification, respectively. A: aperture, M: mirror, L: lens, BS: beam sampler, BBO: β - Barium-Borate crystal, F: filter, NDF: neutral density filter, S: sapphire plate, FM: focusing mirror.

3.5 Characterization of NOPAs

3.5.1 Spectra

For the vis-NOPA, the spectra featured in fig. 21 were obtained by adjusting only the staged mirror position. Spectra of five different wavelengths were taken and normalized to their respective power. It is apparent that the NOPA is optimized for green settings but is also functional for other wavelengths. Towards shorter wavelengths, the power decreases more rapidly than towards longer wavelength, which is consistent with the phase matching curve in fig. 15. With the phase matching curve in mind, one could have expected less decrease in power towards longer wavelength. This could mean that the phase matching and crossing angles are not exactly met as expected.

3 NOPA-NOPA transient IR absorption spectroscopy

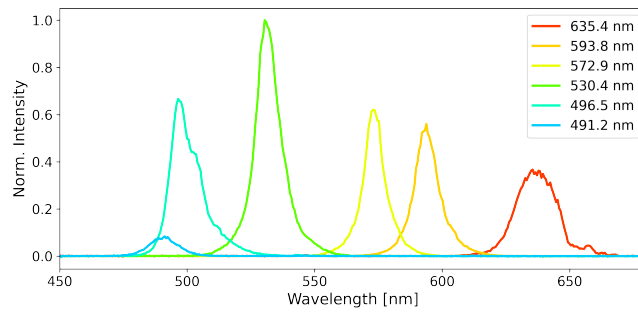


Figure 21: Spectra of the vis-NOPA output, taken for different settings of the movable mirror. The Spectra are normalized to their power.

Fig. 22 shows a spectrum of the IR-NOPA output, optimized for 2200 nm. The spectral shape displays a satisfactory Gaussian profile. The power measured for the IR output was about 13 mW, but this value should be treated with caution as the power meter's sensitivity rapidly decreases for this central wavelength.

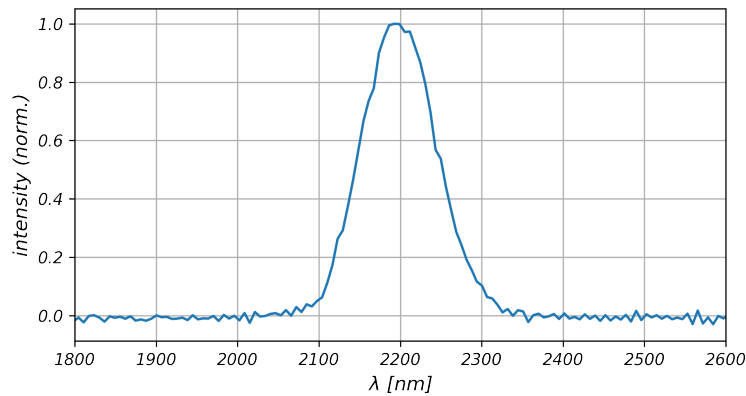


Figure 22: Spectrum of IR NOPA output set to 2200 nm normalized to maximum intensity. The adjustment of the two-step NOPA is more elaborate and only this one central wavelength is needed for experiments. Therefore, the IR NOPA was optimized for a central wavelength of 2200 nm and left at that setting.

3.5.2 Determination of the pulse duration via autocorrelation (AC)

To characterize the pulse length of a fs-pulse, electronics are not suitable anymore because they are too slow. Instead, the pulse itself is used to determine its length. During autocorrelation (AC), the pulse that is supposed to be characterized, is split into two parts. The two parts are then recombined to participate in a $P^{(2)} \propto \chi^{(2)}EE$ nonlinear process. One part of the pulse is then delayed in time with respect to the other. Since a $P^{(2)}$ process is intensity dependent, it is sensitive to the temporal overlap of the two pulse parts. When the pulses overlap perfectly, the intensity is at its maximum, but when the pulses arrive with a relative delay at the medium, the total intensity provided for the $P^{(2)}$ process decreases (see fig. 23 b)). Thus, the AC signal is a function of the delay time Δt that is introduced between the two parts of the pulse. When the initial pulse has a Gaussian profile in time, the AC signal will also be Gaussian. The pulse duration can be determined by eq. 23

$$\tau_{AC} = \sqrt{2}\tau_{\text{pulse}} \quad (23)$$

where τ is the respective full width half maximum (FWHM) of either the AC signal or the investigated pulse.

The autocorrelator used to characterize the visible NOPA output is called NOPA-Pal and was purchased alongside the vis-NOPA's components. Its setup is sketched in fig. 23a). Part of the beam is led into the AC using apertures A1 and A2. The split mirror SM divides the beam into two parts, where one part of the mirror can be moved forward and backward via a piezoelectric crystal that expands or contracts depending on the applied voltage. To produce a continuous back and forth of the mirror position, a sawtooth voltage is applied to the piezo element. Since the range of motion is limited, one part of the mirror is additionally staged, so that the temporal overlap of the pulses can be adjusted.

When the two parts of the beam are focused into the BBO crystal and cross paths, the second harmonic is generated. Due to momentum conservation, the light from the SHG moves straight forward, whereas the two beam parts keep their diagonal paths. Aperture A2 can therefore be used to block majority to the NOPA beam, which leaves mostly the SHG. With the F1 filter, the remaining fundamental is removed before the SHG is focused into a diode. The diode measures the SHG intensity. When both parts of the pulse overlap perfectly, the signal reaches peak intensity whereas more delay between them diminished the SHG intensity (compare to fig. 23b)). Varying the delay between the pulses results in a Gaussian intensity profile if the pulses themselves were Gaussian.

3 NOPA-NOPA transient IR absorption spectroscopy

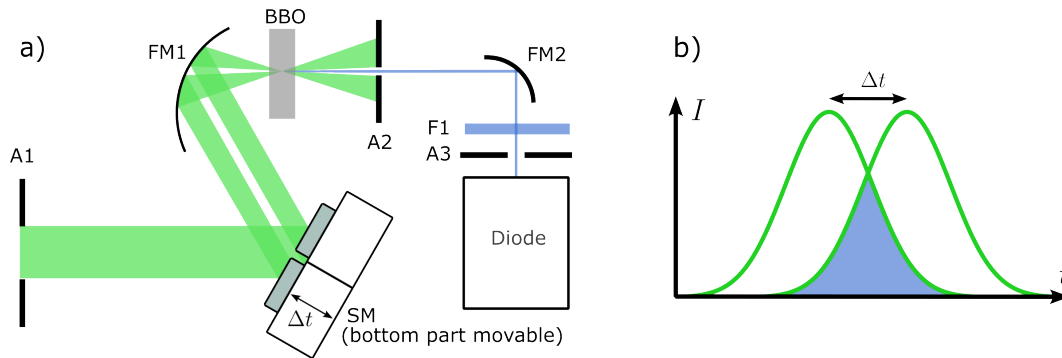


Figure 23: a) Intensity autocorrelation setup. The incoming beam is aligned with the apertures A1 and A2. It is split into two parts by the split mirror (SM). The two parts are then focused into a BBO crystal in a non-collinear geometry. In the BBO, the second harmonic is generated and propagates straight ahead due to momentum conservation. The initial beam is filtered out by aperture A2 and filter F1. A diode measures the SHG intensity.

The trace in fig. 24 displays the autocorrelation signal, that was obtained through the LabView software. It determines the pulse width to $\tau_{\text{pulse}} \approx 125$ fs. Unfortunately, intensity autocorrelation does not contain any information on the pulse's chirp. Therefore, it cannot be assessed whether the pulse is at the Fourier limit (the shortest possible) or not. To reduce potential chirp, a pair of chirped mirrors is installed behind the vis-NOPA. By varying the number of reflections and observing the pulse duration with the AC, the chirp can be minimized. The optimal number of reflections was first determined to be six. But due to various changes in the setup, in attempt to optimize the output power, the appropriate number of reflections might have changed. Throughout the course of the lab work, the vis-NOPA proved to be very unstable. It could not be used for pump-probe experiments despite various attempts. When the vis-NOPA provides a stable output in the future, a prism compressor will be implemented to compensate the chirp. It is not restricted to discrete settings and would not need as much readjustment when changing the output wavelength.

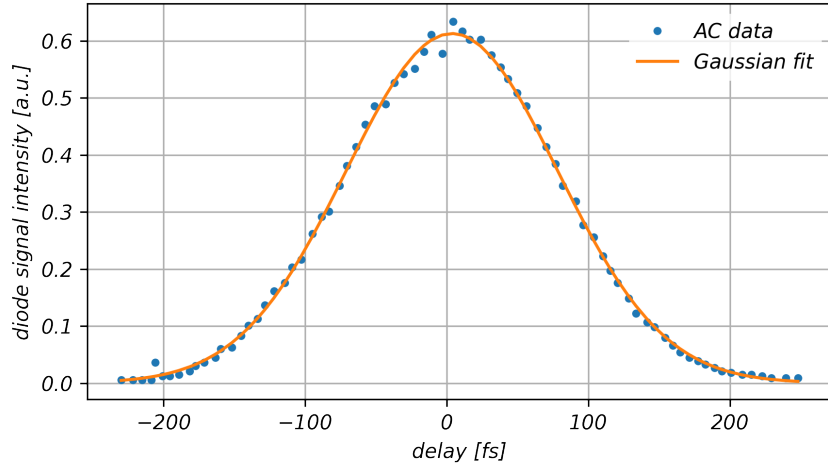


Figure 24: Autocorrelation signal taken with the NOPA-Pal and the corresponding LabView software (blue dots). A Gaussian fit (orange line) results in a FWHM of $\tau_{AC} = 176$ fs which corresponds to a pulse length of $\tau_{\text{pulse}} = \frac{\tau_{AC}}{\sqrt{2}} \approx 125$ fs, according to eq. 23.

3.5.3 Beam profiles

Usually, beam profiles are captured by inserting a beam sampler into the beam path, which guides a small fraction of the beam's intensity towards the beam profiling camera (Thorlabs DCC1545M - USB 2.0 CMOS Camera, 1280 x 1024, Monochrome Sensor). The camera chip is positioned at the exact same distance as the beam sampler is to the location of the sample. However, the camera chip is not sensitive to the 2200 nm IR NOPA output. Instead of using only a fraction of the beam's intensity for imaging, the camera is placed at the sample's position. Multiphoton absorption enabled the observation of the IR beam profile possible. To ensure that the camera is positioned at the correct spot, the pump-probe overlap was fine-tuned before inserting the camera. Subsequently, the camera can be positioned where the pump and probe beam exactly overlap. The IR NOPA's beam profile is displayed in fig. 25. It exhibits a size of $55 \times 40 \mu\text{m}$ with a slightly elliptical but Gaussian profile in x and y direction, respectively.

3 NOPA-NOPA transient IR absorption spectroscopy

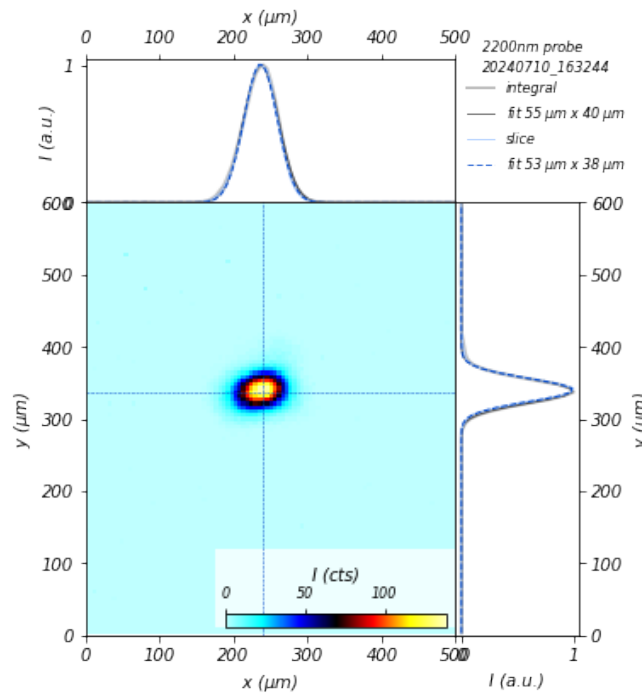


Figure 25: Beam Profile of the 2200 nm IR NOPA output at sample position. The beam profile is determined by integrating over the intensity of the respective dimension and by slicing the beam profile before fitting Gaussian profiles to the data. Both methods yield the same result of $55 \times 40 \mu\text{m}$.

The vis-NOPA beam profile for $\lambda = 530 \text{ nm}$ is captured with the beam sampler in place. The beam profile consists of two intensity maxima, see fig. 26, left. In order to achieve a Gaussian beam profile, an aperture is used to isolate the left intensity maximum. This reduces the total output power by about 40 %.

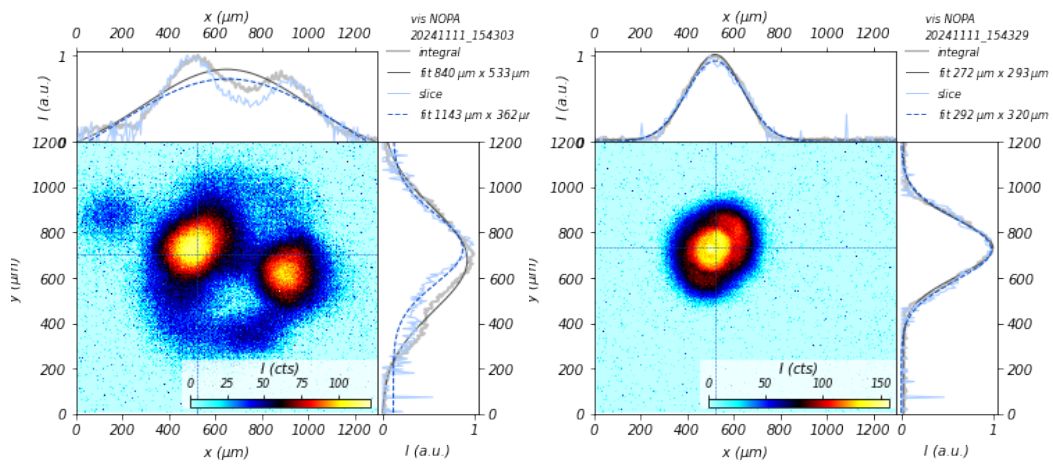


Figure 26: Left: Beam profile of the 530 nm vis-NOPA output at the sample position. Two maxima are clearly visible. The origin of the split profile is unknown, but the WL seed of the vis-NOPA might be responsible. Right: Clipped beam profile. An aperture was used to clip the beam profile to the maximum intensity.

3.6 Optimizations

1. For the alignment of the vis-NOPA setup, the focus of the pump beam was positioned after the amplification crystal. Focusing the beam in air prior to entering the BBO could cause unwanted nonlinear effects that would influence the beam profile and overall performance of the amplification process. Therefore, the focus was moved behind the BBO by adjusting the distance of the telescope lenses and the position of the BBO as much as possible without clipping the incoming beam. Bringing the BBO closer to the focusing mirror requires the pump beam to hit the FM higher up in order to still achieve the required crossing angles. To grant the correct beam height, the FM was elevated by about half a centimeter by installing it on a mounting plate, that are typically used to secure mirror mounts to the table. To find the correct height, the relationship between distance and pump beam position on the FM was plotted in fig. 27 using trigonometry.

3 NOPA-NOPA transient IR absorption spectroscopy

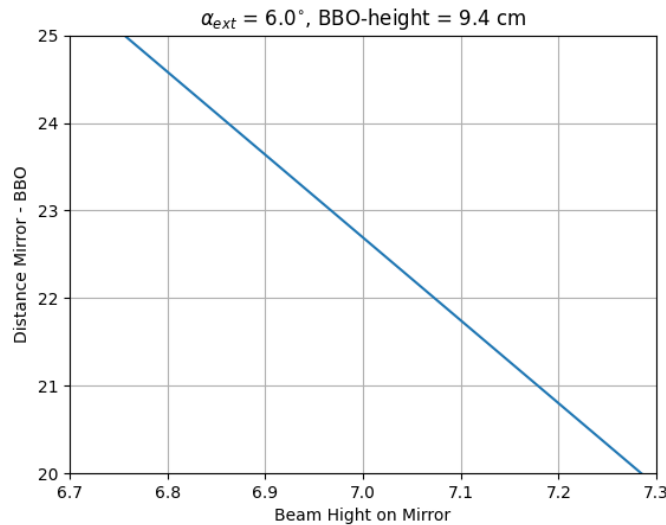


Figure 27: The pump beam height on the focusing mirror FM h_{FM} as a function of the distance d between the amplification crystal BBO2 and the focusing mirror FM, in order to preserve the external crossing angle α_{ext} . From trigonometric considerations the linear relation $h_{\text{FM}} = -d \tan \alpha_{\text{ext}} + h_{\text{BBO}}$ is found, where h_{BBO} is the height above the table.

2. During the initial alignment of the vis-NOPA, the crystal had to be tilted significantly more than expected to bring the colors of the fluorescence cone together as closely as possible. It turned out that the amplification BBO actually had a cutting angle of $\theta_{\text{cut}} = 29.2^\circ$ instead of the assumed $\theta_{\text{cut}} = 32.5^\circ$. A crystal with the correct cutting angle was found and inserted into the setup, leading to a narrower fluorescence cone and a safer tilting angle regarding laser safety. Since the new crystal is thinner, the output power decreased slightly, setting the maximum achieved power to about 40 mW, instead of the previously achieved 50 mW.
3. When attempting to use the vis-NOPA as a pump beam, barely any of the generated output power of the NOPA arrived at the sample. It turned out that the chirped mirrors have to be used with a very steep angle of incidence (AOI) of only $5 - 10^\circ$ with respect to the surface normal. When the AOI becomes larger, an increasing fraction of the NOPA output is transmitted rather than being reflected by the mirrors. With multiple reflections, this drastically decreased the intensity available for pump-probe experiments.
4. The IR NOPA mostly produced a stable output, but due to its wavelength in the near IR range, it was difficult to work with. IR viewers and fluorescence cards could not detect the wavelength and the thermal power meter was not very sensitive to the wavelength. This made it difficult to find the spatial overlap for a pump-probe measurement and couple the IR probe beam into a fiber for the spectrometer. Unfortunately, the IR beam did not precisely follow the apertures on the way to the sample. Yet, the signal wavelength of about 1500 nm, which is usually filtered out with a low-pass filter, approximately followed the apertures. It became apparent that the second amplification step

was not as collinear as expected. Some time was spent on rebuilding the collinearity, but this unfortunately decreased the output power. When IR sensitive thermopaper was provided by a colleague, the IR NOPA output was optimized for power and guided to the sample using the paper.

5. As a result of a laser service, the output power of the spitfire was raised from about 0.83 W to 1.3 W by increasing the current of the Ascend CW pump laser. Since the BBO crystals can be damaged by overly high intensities, absorptive gray filters were used to temporarily reduce the beam intensity to the previous input power. While removing the filters one by one the SHG spectrum of the IR 400 nm pump beam was simultaneously observed. Before the crystal is damaged, the SHG spectrum is expected to produce wings at the edges. At the highest possible intensities the formation of wings could be observed. In order to reduce the intensity on the crystal, the telescope was used to enlarge the beam diameter. However, the Spitfire beam profile started to deteriorate noticeably after about an hour of operation time. Because it also provides the pump beam for the experiments, a regular beam profile is of great importance. In the end, the Ascend pump current was decreased to reinstate the initial settings to produce a Spitfire output of about 0.85 W. The change in telescope settings was discarded.

4 Measurements and analysis

The initial goal was to recreate the measurements described in the introduction, but with a slightly different sample, using TiO₂ nanoparticles (NPs) with Au NPs instead of embedding the Au NPs in a film of TiO₂. Due to various problems with the setup, this goal could not be achieved. Instead, discrepancies within the fluence series became the center of attention. This chapter will first provide an overview of the samples used and their characterization. Subsequently, the transient measurements taken in the course of the lab work will be discussed.

4.1 Sample characterization

The samples used for transient absorption spectroscopy consist either of only TiO₂ NPs, which are commercially available (Sigma-Aldrich: Titanium(IV) oxide, product nr. 718467), with a primary particle size of 21 nm or they consist of TiO₂ NPs and Au NPs. In total, three samples were used for the transient measurements: one with only TiO₂ NPs and two with Au NPs added. Steven Berth manufactured the sample TiO₂-AuNP #2 in July 2024, while the other two samples (TiO₂-AuNP #1 and TiO₂ #32) were fabricated by Dr. Wouter Koopman more than a year ago. TiO₂-AuNP #2 has a 2 mm thick CaF₂ substrate while both other samples use a 1 mm glass slide as a substrate.

To achieve the growth of Au NPs on the TiO₂ NPs, the latter were dissolved in ethanol. Gold-containing acid (Chloroauric acid, HAuCl₄) was added and under illumination, the growth of Au NPs was stimulated. After reducing and washing the particles, they are used to coat a substrate with. For a more detailed description of the sample preparation process, see ref. [42].

Imaging similar samples (additionally containing copper) with TEM provides the pictures displayed in fig. 28. Images of the original samples were not obtained. However, the sample preparation with- and without copper follow the same scheme, so that the resulting samples can be assumed to be quite similar. According to fig. 28, the metallic nanoparticles appear to be only a fraction of the TiO₂ NPs' size. Assuming the bigger particles are TiO₂, measuring a few particles from the images results in diameters of 18 nm to 35 nm, but with most values around 20 nm for the TiO₂. For the smaller particles, that are associated with metallic particles, diameters between 4 nm and 10 nm have been sampled.

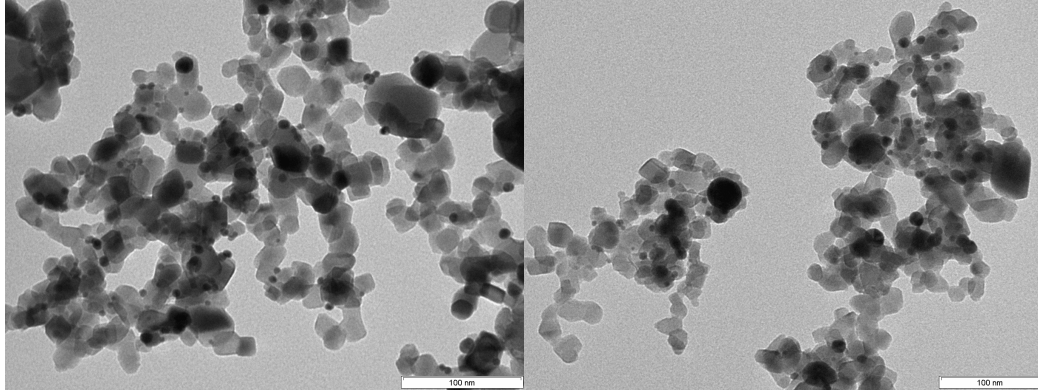


Figure 28: TEM pictures of TiO_2 with Au and Cu NPs. Bigger, more angular particles are associated with TiO_2 , smaller round particles are associated with Au or Cu. Figure provided by Dr. Wouter Koopman.

For further characterization, static extinction spectra of all three samples were taken with the Cary5000 UV-Vis-NIR spectrometer. Figure 29 shows the baseline-corrected spectra. The spectrometer obtains the extinction A only from the transmission signal: $A = -\log_{10}\left(\frac{T}{T_0}\right)$, not taking scattering or reflection into account. A true absorption spectrum also considering these influences could not be obtained since the Ulbricht sphere is broken at the moment. Due to the possibly strong scattering influence on the samples' extinction spectra, only the transient measurements as a very sensitive method will reveal the absorption behavior with certainty.

The TiO_2 samples exhibit a quickly rising extinction when nearing the band gap energy. However, the absorption (unexpectedly) also extends into the visible range. Considering the large surface-to-volume ratio of the TiO_2 nanoparticles, the tail can be attributed to surface states in the band gap. Even though the extinction in the visible range is comparatively small, the contribution, especially at 400 nm where the sample is to be excited, is still enough to produce signal in the transient measurements. At 2200 nm where the probe wavelength will be situated, the static absorption is zero, so that which supports the attribution of the probe signal to additional carriers in the conduction band.

The static absorption spectra of the TiO_2 &Au NP samples both show an additional feature that can be attributed to the plasmon peak of the Au NPs. For sample #2 the peak is visibly more pronounced. Since sample #1 was older than a year when the spectra were taken, degradation of the Au NPs might be a reason. Differences in the preparation method might also play a role. Comparing the position of the plasmon peak at 570 nm to the position for Au NPs in air at about 500 nm [33] reveals a distinct shift. Alongside the TEM images, this might be an indicator that the metallic NPs grew directly on the TiO_2 : since TiO_2 has a different permittivity than air, the resonance position shifts according to the Fröhlich condition [44]. However, in ref. [23] a shift of the plasmonic resonance of metallic NPs covered with multiple levels of polymers is observed, even though the polymer merely lies on top of the NP. Therefore, the shift in the resonance position only proves that the Au NPs are surrounded by TiO_2 , but the growth of the metallic NPs on the surface of the TiO_2 NPs cannot certainly be determined.

Both the pure and the mixed samples do not produce a static extinction signal at the probe wavelength of 2200 nm, which is in accordance with the assumption that the probe only interacts with the conduction band electrons in the SC.

(Note: transient measurements were executed before measuring the absorption spectra because the latter could damage the sample).

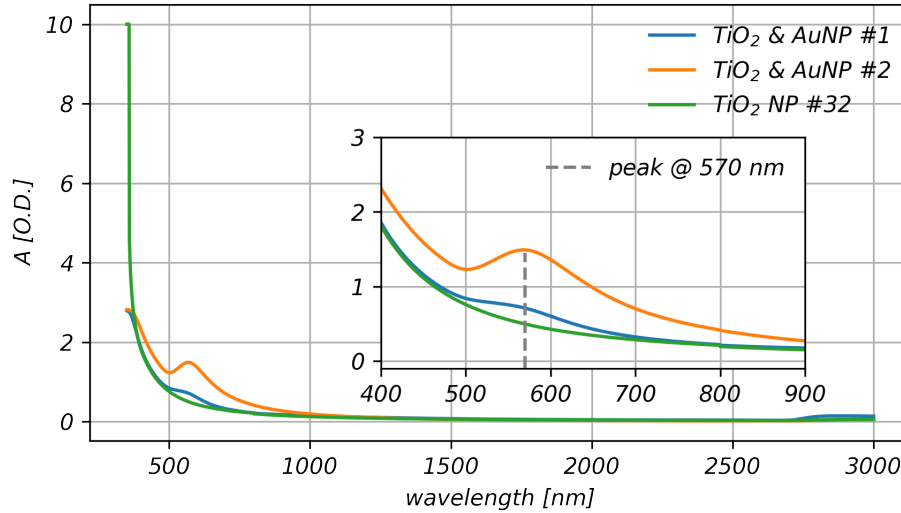


Figure 29: Extinction Spectra of the investigated samples TiO₂ & AuNPs #1 (blue), TiO₂ & AuNPs #2 (orange), TiO₂ #32 (green) measured with the Cary5000 UV-Vis-NIR spectrometer from 350 nm to 3000 nm. Both samples with Au NPs show an increased extinction A at 570 nm where the plasmon absorption band would be expected (see inset). For sample #2, however, this feature is much more pronounced. Approaching shorter wavelengths, the extinction increases quickly, as expected due to nearing the band gap energy. It is important to note that even the pure TiO₂ sample exhibits non-zero extinction over the whole visible range, which indicates a high number of trap states. Since the extinction does not take scattering into account, only the TIRAS measurements will reveal the true absorption behavior of the sample.

4.2 Pump-probe measurements

Since the data, which will be discussed in the following subsections, is already pre-processed, the first part of this section will describe the pre-processing. Subsequently, the different measurement series will be considered in more detail.

4.2.1 Data analysis

Figure 30 displays the processed data. Here, the relative change in transmission $\frac{\Delta T}{T}$ is plotted against the time delay.

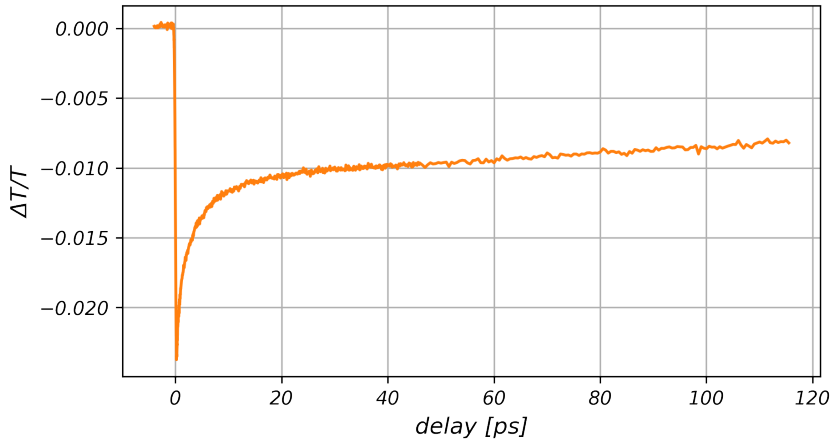


Figure 30: Pump-probe trace obtained by calculating the average difference signal from the pumped and unpumped data, applying a background correction, and sigma-clipping. t_0 was determined from the fit of a sigmoid function. This trace belongs to the data set displayed in fig. 49 and was taken with a pump fluence of $F = 8.7 \frac{\text{mJ}}{\text{cm}^2}$.

The delay is achieved through varying the mechanical stage position, which delays the pump and probe pulse with respect to each other. To measure the change in transmission, the transmitted probe intensity for an unpumped sample and a pumped signal have to be subtracted as per eq. 24.

$$\frac{\Delta T}{T} = \frac{T_{\text{pumped}} - T_{\text{unpumped}}}{T_{\text{unpumped}}} \quad (24)$$

To measure these intensities, the Avantes AvaSpec NIR256-2.5-HSC spectrometer monitors the probe beam. The spectrometer is synchronized with a chopper to differ between pumped and unpumped signals. Our chopper is a disc with an alternating pattern of open and closed segments, which interrupt the beam periodically when rotating. It is placed into the pump beam path so that the pump beam can only pass the chopper and reach the sample when it arrives with at an open segment (compare to fig. 31). The rotation frequency is set to 125 Hz, which means that every segment blocks or allows a few pulses in a row. The exact number of pulses depends on the width of the segments.

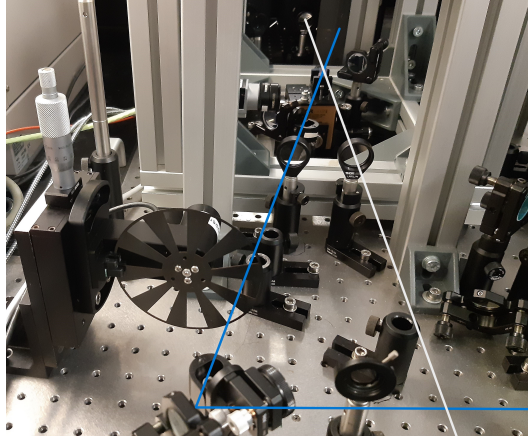


Figure 31: Chopper in the pump-probe setup. The disc chopper periodically blocks the pump beam (blue). The probe beam (light gray) is monitored by the spectrometer and unaffected by the chopper.

Because the spectrometer is synchronized with the chopper, each data point can be ascribed to either the measurement of an unpumped or pumped sample. For each delay step, the pumped and unpumped signals are integrated for a set integration time, and then saved in separate files. From these files, the change in transmission can be calculated later on, according to eq. 24. When all delays from the given range have been measured, one “loop” is completed and the process restarts at the first delay until the set number of loops is reached. The loops can then be averaged in order to improve the signal-to-noise ratio. For setting the number of loops to measure, the integration time, and the spectral range, the “Spectro Pump Probe” Python software, which was programmed by a previous UDKM group member, is utilized. It coordinates the spectrometer communication and the synchronization with the laser and the chopper, saving the collected data automatically. It also automatically takes a background spectrum (with the probe beam blocked) before the measurement.

Fig. 32a) (upper part) displays the initial result of a pump-probe measurement as described above, $\frac{\Delta T}{T}$ already calculated and background corrected. The signal is averaged over five loops and measured from 2050 – 2400 nm with the delays ranging from –1400 to –1280 ps regarding the absolute stage settings. The relative change in transmission is indicated by the blue color map where darker blue encodes an increasingly negative difference. Since the probe signal indicates the number of electrons in the TiO_2 conduction band, a negative signal is equivalent to an increased number of electrons that can absorb the pump light contrary to an empty conduction band. At the edges of the spectrum the signal consists rather of noise, because the probe pulse has a Gaussian spectral shape, centered around 2200 nm with a full-width at half-maximum (FWHM) of 104 nm (see fig. 32b)). At the edges, the probe pulse intensity has decreased to zero. One can also see, that the center of the probe pulse is not exactly the center of the spectrum which explains why the noise is not distributed symmetrically around the signal. I therefore chose a window of ± 40 nm around the central wavelength (indicated by the orange box in fig. 32 a)) to extract the transient behavior in all subsequent measurements. In this region, one is well within the FWHM of the probe pulse, where a strong the signal can be expected. Averaging the signal over this window increases the signal-to-noise ratio and results in the trace displayed in the lower part of fig. 32a).

4 Measurements and analysis

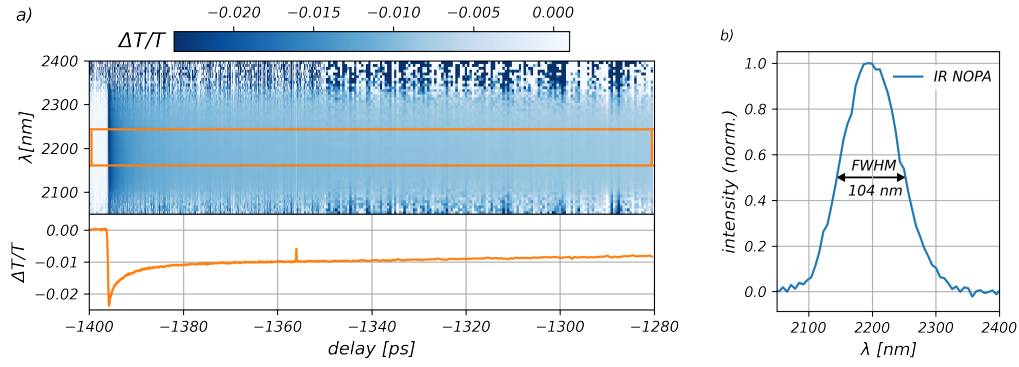


Figure 32: Overview of the pump-probe data from a measurement with five loops. The upper part of subfigure a) displays the differential signal averaged over all measured loops and with the background spectrum subtracted. The color gradient encodes the amplitude of the difference signal $\Delta T/T$, which is negative for this kind of measurements. The lower part shows a cut through the upper signal, averaged over the orange box above, that has a width of 80 nm. Subfigure b) displays the spectrum of the IR NOPA output that is used as a probe beam. It exhibits a FWHM of 104 nm.

To discuss the data as a function of the delay between the pump and probe pulses instead of the absolute stage delay, one needs to determine the “time zero” t_0 , at which the pulses arrive at the sample at the same time. There are different conventions to determine t_0 , such as using i) the maximum signal, ii) the first point where the signal drops, iii) the steepest slope of the decrease, or iv) the center of the decrease. The latter is the convention used in this thesis. t_0 is determined by fitting a sigmoid function $s(t)$, that is based on the error function “erf”, to the modified data. Equation 25 specifies the form of the sigmoid function

$$s(t) = a \cdot \left(\operatorname{erf} \left(\frac{t - \mu}{\tau} \right) \right) \quad (25)$$

where a is the amplitude of the function, μ is the center and τ is the width of the function, which is proportional to the pump pulse duration. When normalizing the data to the maximum amplitude, the parameter a can be set to $a = -1$. The sigmoid function cannot handle the decay of the signal. Therefore, the data is modified for fitting process by replacing all values after the maximum amplitude with the maximum, see fig. 33. When a fitted successfully, the center μ of the sigmoid function can be identified with t_0 .

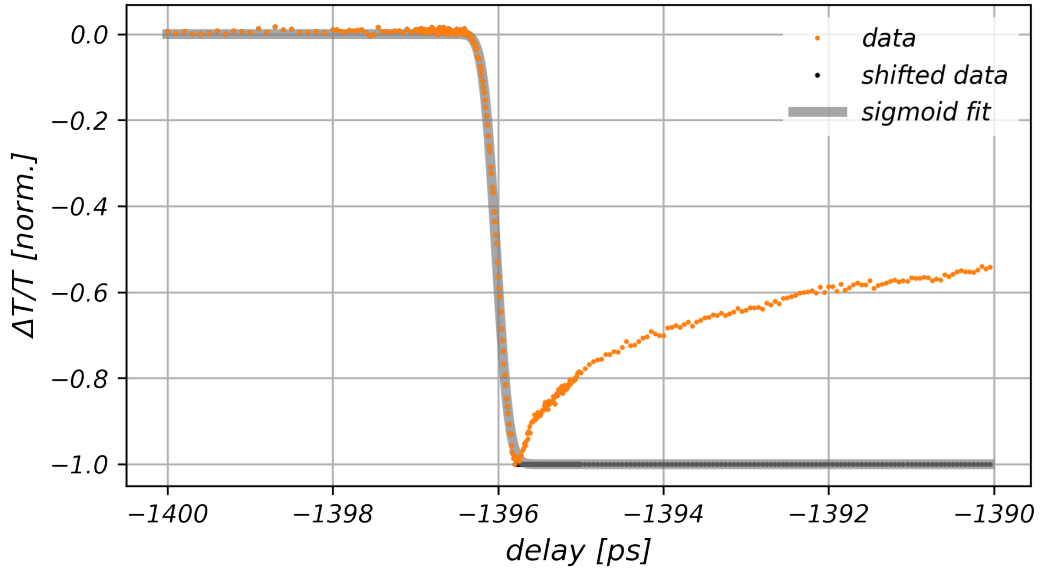


Figure 33: The sigmoid function $s(t)$ (eq. 25) is fitted (gray line) to the modified data (black dots). The center of the sigmoid’s slope is at $t_0 = -1396.02$ ps.

Following this procedure, the absolute time zero was determined to be at $t_0 = -1396.02$ ps.

Throughout the measurement, outliers can occur, for example, due to an interruption of the beam or a software issue. To eliminate these outliers from the data sigma-clipping is implemented, which is based on the Astropy function “sigma_clip”. In order to find outliers, the standard deviation σ is determined for an interval of the data, which glides along a selected axis, usually the delay axis. When one value is outside the bounds of $c \cdot \sigma$, where c is a constant factor, this value is replaced by the mean value of the interval. By selecting the factor c properly, outliers and noise can be reduced. However, imposing too strict constraints might distort the data, especially in places with steep slopes. Therefore, the factor is usually chosen just strict enough to dispose of the outliers. Applying sigma-clipping with $c = 2.4$ to the data in fig. 32a) eliminates the outlier at about -1255 ps. The corrected data is displayed in fig. 30.

Now that the signal processing has been established, I will discuss its interpretation. Three samples are investigated. Two of them consist of P25 TiO_2 NPs with Au NPs grown on them. Because the extinction spectra in fig. 29 suggest the possibility of a direct excitation of the TiO_2 with a 400 nm pump wavelength, the third sample is only made of P25 TiO_2 NPs. Examining both sample types makes it possible to compare the results and attribute differences to the Au NPs. Pumping the samples with 400 nm excites electrons into the conduction band of the semiconductor via various mechanisms. Possible excitations include the direct excitation of rutile TiO_2 (over the band gap), excitation of in-gap states to the TiO_2 conduction band, and charge transfer from interband excitations of the Au NPs. Ratchford et al. demonstrated in ref. [28] [13] that Au NPs themselves do not absorb near-IR probe wavelength even after carrier excitation. Therefore, the observed absorption of the 2200 nm probe beam is attributed to the electrons in the TiO_2 conduction band. Since the signal only considers the difference between pumped and unpumped sample, it directly indicates the number of electrons excited into the CB by the pump

beam.

4.2.2 Homogeneity

After obtaining a first signal from the sample TiO₂-Au NP #1, the sample's homogeneity was investigated first. For this purpose, measurements were conducted at different sample positions; see fig. 34. The measurements were executed with $\lambda_{\text{pump}} = 400 \text{ nm}$ and $\lambda_{\text{probe}} = 2200 \text{ nm}$. The initial amplitudes vary, suggesting that the sample concentration is not distributed completely evenly over the substrate. Normalizing the traces to the maximum amplitude returns the same dynamics, as expected.

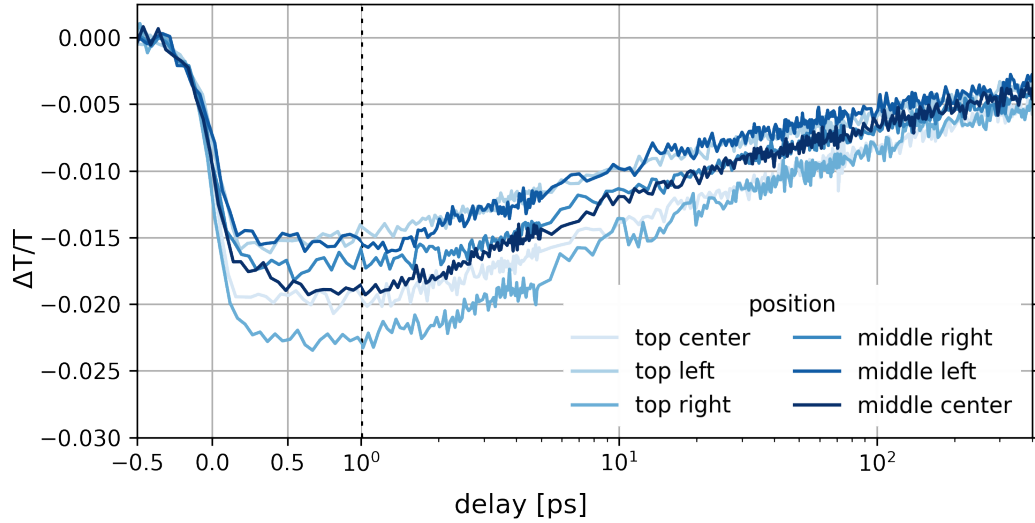


Figure 34: Transient measurements with $\lambda_{\text{probe}} = 2200 \text{ nm}$ and $\lambda_{\text{pump}} = 400 \text{ nm}$, with a fluence of $F = 11.5 \frac{\text{mJ}}{\text{cm}^2}$ on different positions of the sample. Since the initial amplitudes vary, the sample seems to be not strictly homogeneous. On longer time scales, the dynamics align.

Due to this insight, special attention is paid to finishing one related series of measurements (e.g. a fluence series) on the same day so that drifts of the laser spot or repositioning of the sample cannot pose a source of errors. The homogeneity was not checked for all samples, but since the method of preparation is very similar, similar results are to be expected.

4.2.3 Fluence series

As a first step to investigate the sample, a fluence series is taken. Since the vis-NOPA does not produce output reliably, the pump wavelength is kept at $\lambda_{\text{pump}} = 400 \text{ nm}$ to excite Au interband transitions. Since Brown et al. come to the conclusion that excited plasmons in Au NPs mainly decay to interband transitions [4], the replacement of the pump wavelength might not impact the pumping process much. This needs to be verified in future projects.

The sample TiO₂-AuNP #1 is first measured with four different fluences from high to low over a range of 2600 ps. The results are displayed in fig. 35. All curves show a maximum signal just after excitation, that decays, but does not reach zero within the measured 2600 ps. The inset of this figure shows the first picosecond of

the normalized data. Leaving the noise out of consideration, the different signals seem to follow the same dynamics directly after excitation.

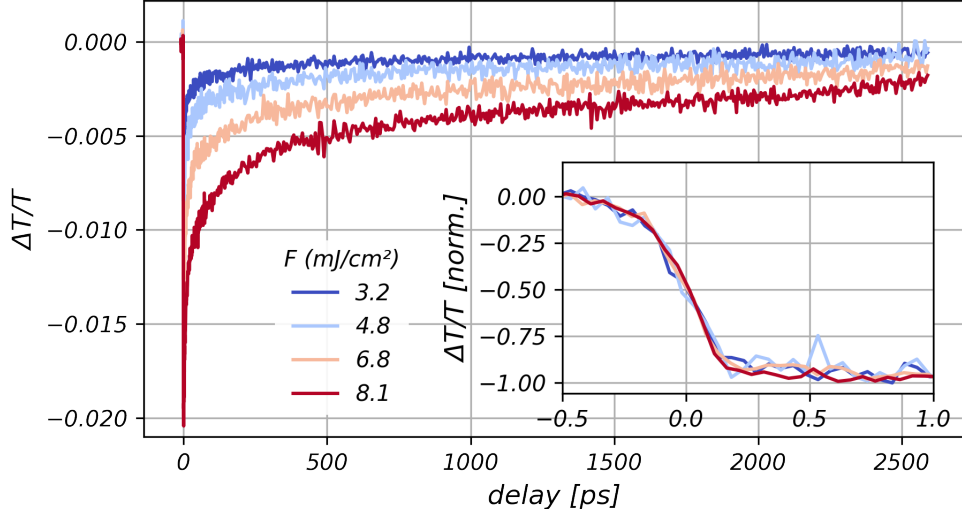


Figure 35: Fluence series on the sample $\text{TiO}_2\text{-AuNP \#1}$ with $\lambda_{\text{pump}} = 400 \text{ nm}$ and $\lambda_{\text{probe}} = 2200 \text{ nm}$. Four fluences were measured from high to low. Blue indicates the lowest fluence, and red indicates the highest fluence. The inset shows the normalized traces up to the first picosecond after excitation. Apart from some fluctuations, the dynamics seems to be equal for the different fluences. This indicates that the signal rises faster than can be resolved with the laser.

However, the beam profile during those measurements was irregular as can be seen in fig. 36. This means small shifts in the beam position on the sample could cause a strong change in the fluence. Even though the probe beam is significantly smaller than the pump beam, it might hit a spot where the fluence is not constant throughout. Therefore, the measurements should be repeated to ensure the results are reproducible.

4 Measurements and analysis

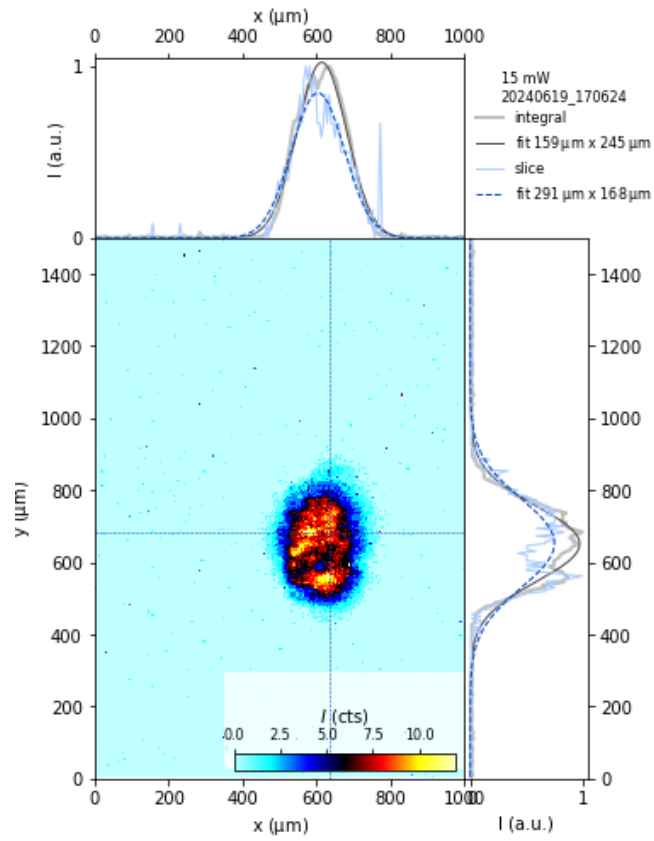


Figure 36: Beam profile of the pump beam at 15 mW pump power. The beam profile shows an irregular structure with a hole in the lower third.

Assuming the signal strength is proportional to the number of carriers excited to the conduction band, the amplitude of the signal is expected to increase with the fluence. Therefore, the maximum amplitudes $\frac{\Delta T_{\max}}{T}$ are plotted as a function of fluence in fig. 37. It should be noted that the “maximum amplitude” corresponds to the smallest value because the signals are all negative. The general trend follows the expectation, but from only four data points, it is difficult to determine whether the relation between amplitude and fluence is linear or nonlinear.

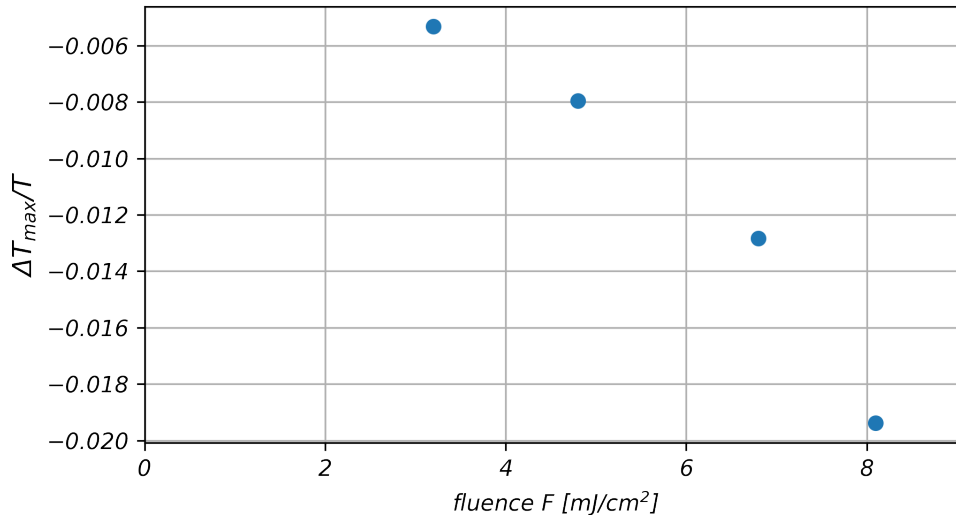


Figure 37: Maximum amplitudes plotted against the respective fluence. The amplitude is determined from the mean of the first ten points after the maximum of the signal.

In combination with the unsatisfactory beam profile the measurement is repeated with more fluences and an improved pump profile to reach conclusive results.

4.2.4 Problems with fluence series

For the second fluence series, sample TiO₂-AuNP #1 was used as well. Seven different fluences were measured. In the beginning of the measurement process, the beam profile had a more regular shape. But after the first three fluences, the beam profile started deteriorating by forming two intensity maxima, leaving a local minimum in the center of the beam. Beam profiles of the first and fourth measurement are displayed in fig. 38.

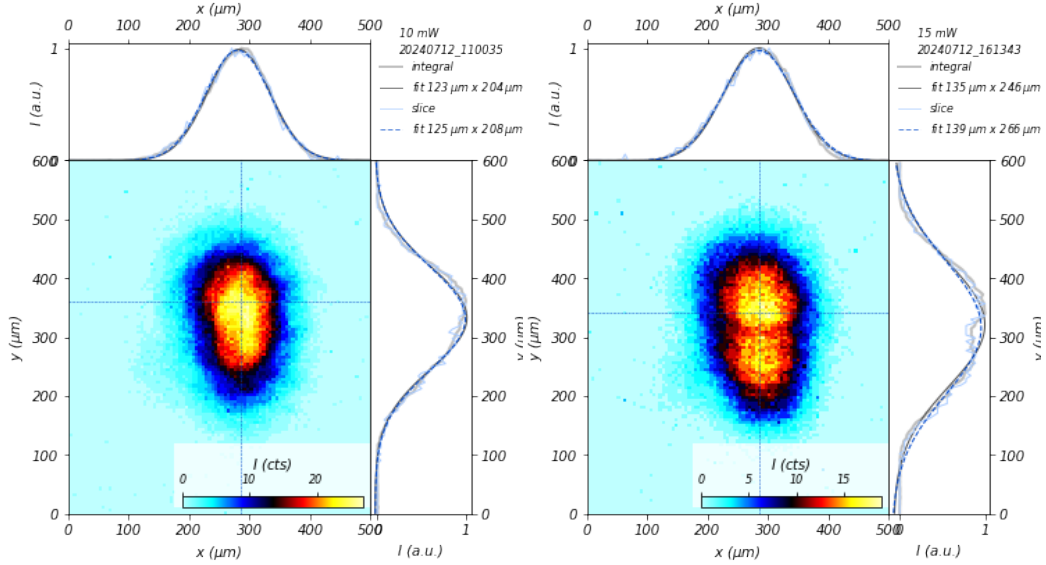


Figure 38: Beam profiles of the first (left) and sixth (right) measured fluences ($F = 6.7 \frac{\text{mJ}}{\text{cm}^2}$ and $F = 8.5 \frac{\text{mJ}}{\text{cm}^2}$, respectively). The Beam profile deteriorates with time.

A larger number of fluences was measured in order to confidently identify a (non)linear relation between amplitude and fluence. However, the signal unexpectedly became very noisy throughout the measurement series. The traces additionally exhibit a kink after 1500 ps, which might be caused by sample degradation. Since degradation is suspected, the measurement series will be repeated on another spot of the sample instead of analyzing it further.

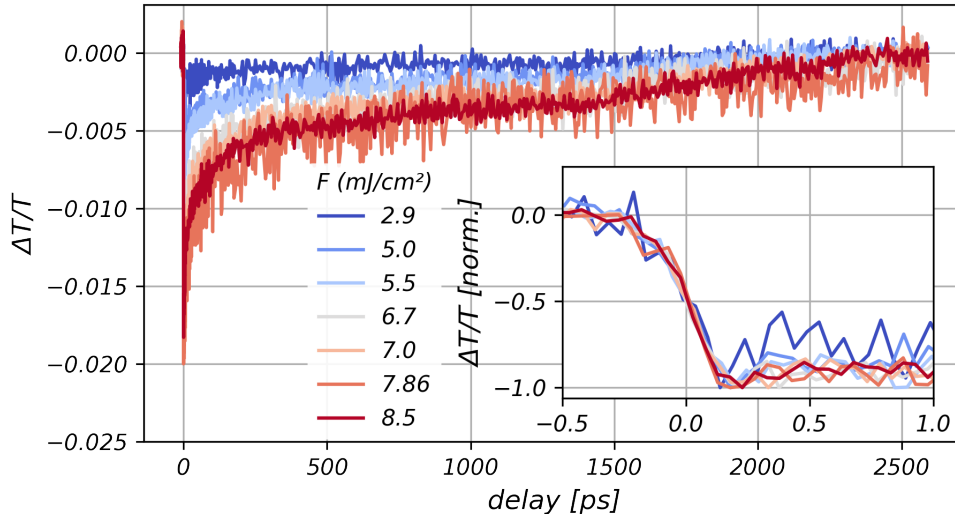


Figure 39: Second fluence series on the sample $\text{TiO}_2\text{-AuNP \#1}$ with $\lambda_{\text{pump}} = 400$ nm and $\lambda_{\text{probe}} = 2200$ nm. Seven fluences were measured. Blue indicates the lowest fluence, and red indicates the highest fluence. Compared to the previous fluence series, the signal bends back to zero earlier and more quickly than expected. Sample deterioration might be the cause. The inset shows no deviations in amplitude rise of the measurements.

To address the sudden increase in noise in the signal, various potential sources in the setup were investigated. Pointing stabilization, software issues, faulty cables and hardware issues with the chopper were identified as potential sources of increased noise. The pointing stabilization is prone to overshooting, which was addressed by reducing the step size of the motorized mirror. The problem still was not solved until a sleep time was introduced to the program to ensure the motorized mirror has stopped moving before reevaluating the position of the beam. Another source of outliers came directly from the spectrometer communication. When the data was requested quicker than the spectrometer was ready, the data point was recorded as zero and the spectrometer returned an error message. This issue was avoided by trying for data transmission between spectrometer and measurement program (PC) up to ten times before returning an error and a zero. Most of the time, a second communication attempt was enough. Furthermore, the chopper was suspected to cause noise due to errors in synchronization. Other labs within the work group had similar problems at the time, so that their troubleshooting was mirrored. The chopper's BNC cable, its phase, and even the chopper itself were changed in order to locate the source of the noise. In the end, a mixture of phase and height settings reduced the noise to an adequate level.

Similar to the second fluence series, the beam profile for the third fluence series resembled a Gaussian shape at first. With time, it started to exhibit a dent in the middle though. When adjusting the spatial overlap before the measurement, attention was paid not only to optimizing for signal intensity but also stability. This was realized by avoiding settings where the slightest change in position causes a significant drop of the signal intensity.

4 Measurements and analysis

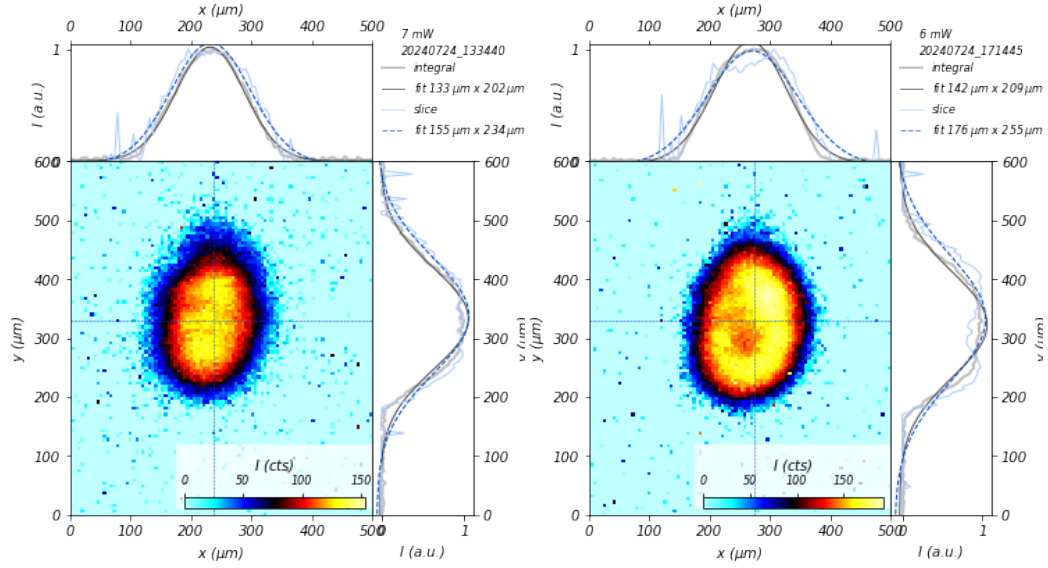


Figure 40: Beam profiles of the third and eighth measured fluences ($F = 4.8 \frac{\text{mJ}}{\text{cm}^2}$ and $F = 3.6 \frac{\text{mJ}}{\text{cm}^2}$, respectively). Here, too, the beam profile deteriorates over time.

Throughout the third fluence, series chopper height and the spatial pump-probe overlap were carefully optimized in between each measurement of the series. Nine different fluences were measured for this series, alternating between high and low. Fig. 41 displays the data of this series. These traces do not show a kink after 1500 ps, indicating that the previous sample spot was indeed deteriorating. Compared to the previous series, the noise level is reduced quite a bit, but it is still not at the initial low level.

A prominent feature that was not present in the previous data is the oscillations in the trace with the highest fluence. Since this cannot be reproduced properly and the oscillations vary from loop to loop, this feature could be caused by an unstable overlap due to overshooting of the beam stabilization. An optimization of the sleep time during the motor movement might help. But an unstable signal intensity due to the irregular beam profile is also conceivable.

The inset of fig. 41 shows the trace for each fluence normalized to its maximum amplitude. Unlike the two previous fluence series, the signals do not align as well, especially where the maximum amplitude is reached. They fan out slightly, and the highest fluence reaches its maximum later. This could be due to the noise level, which is lower than in the second series but still not on the initial level.

Looking at the first 400 ps of the signal, the amplitudes of the traces do not correlate with the fluence as expected. Lower fluences sometimes exhibit larger amplitudes or vice versa.

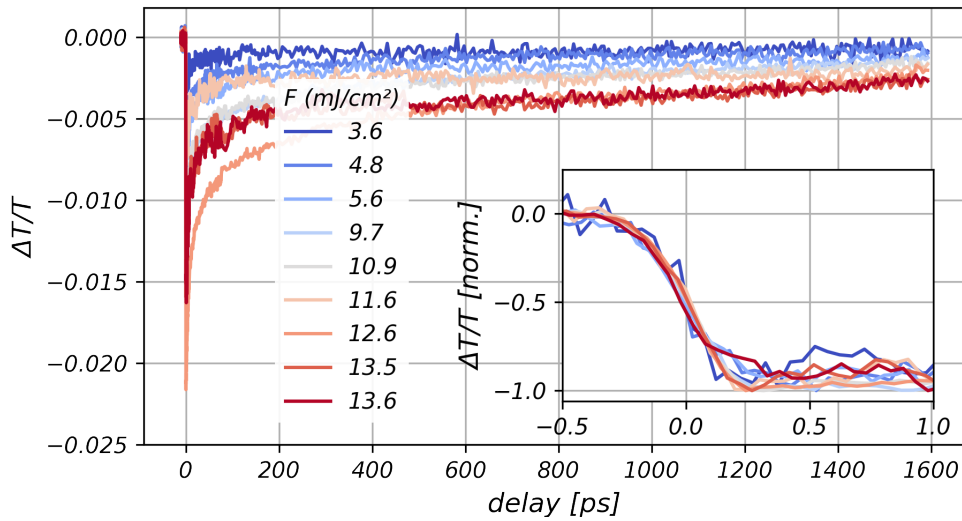


Figure 41: Third fluence series on the sample $\text{TiO}_2\text{-AuNP \#1}$ with $\lambda_{\text{pump}} = 400 \text{ nm}$ and $\lambda_{\text{probe}} = 2200 \text{ nm}$. Nine fluences were measured. The highest fluence does not correspond to the largest amplitude. The inset shows the normalized traces up to the first picosecond after excitation. Just before the maximum amplitudes are reached, the traces seem to fan out.

In order to take a closer look at the relation between the maximum amplitude and the fluence, they are plotted against each other, see fig. 42. This does not result in the clear trend, which was expected based on the visual assessment of the fluence series. Especially for higher fluences the amplitudes do not follow any trend.

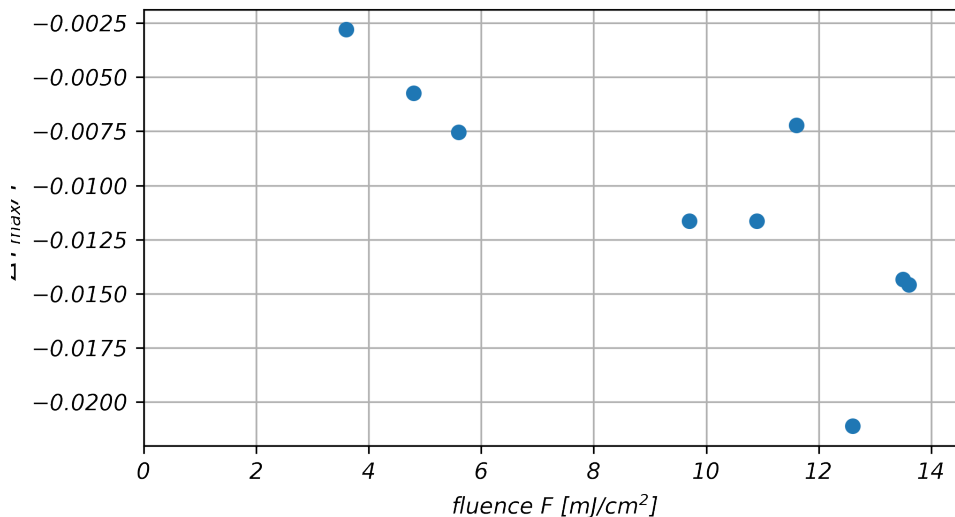


Figure 42: Maximum amplitudes of the third fluence series plotted against the fluences. The maximum amplitude is determined from the mean of the first ten points after the maximum signal. Especially for higher fluences, the amplitudes do not follow the expected monotonous increase.

4 Measurements and analysis

There are two hypotheses to explain the inconsistent relation between amplitude and fluence. Either instabilities of the laser setup cause the inconsistencies or the sample does not completely relax back into its initial state between measurements. This would mean that the previously set fluence influences the next measurement. Regarding the latter hypothesis, charging effects could, for example, play a role. The probe beam is only sensitive to the electrons in the TiO₂ conduction band, so charging effects could become relevant if the sample spot in focus is depleted of charges. This would of course influence the amplitudes of the next measurement(s). Following this suspicion, the maximum amplitudes were plotted in the order they were measured in fig. 43. The fluences are encoded in the same colors as in fig. 41. No instant correlation between amplitude and order of measurement or fluence can be made. Since the amplitudes do not strictly follow the order they were measured in, but also do not strictly in-/ decrease with the fluence, further experiments are required to draw a conclusion.

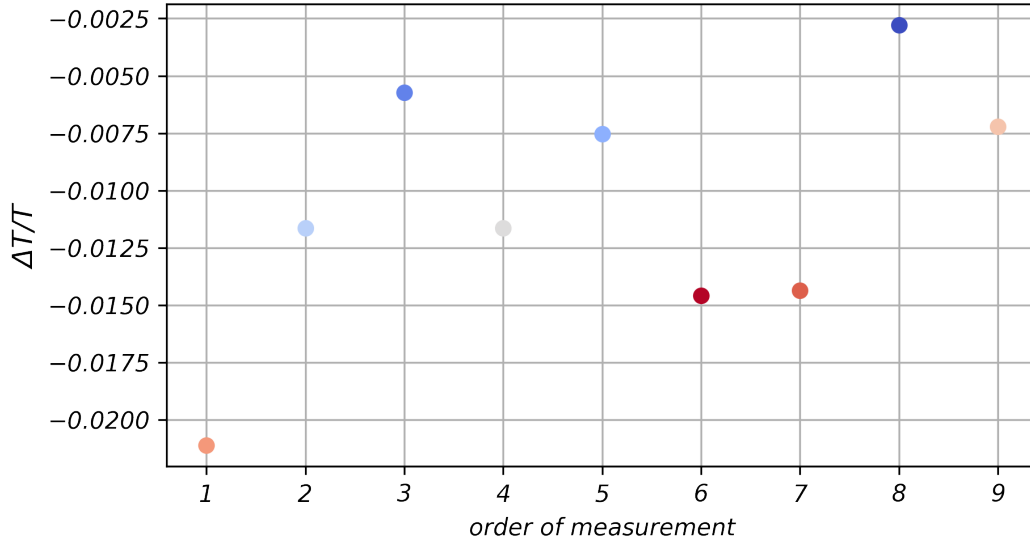


Figure 43: Maximum amplitudes of the third fluence series plotted against the order in which the measurements were conducted. The color indicates the fluence, matching with the colors used in fig. 41. No clear trend is apparent, but the amplitudes seem to rather decrease with the number of measured traces.

If charging effects prevent the sample from relaxing back into its initial state between measurements, the amplitude of a signal should slowly decrease throughout a longer measurement. To monitor possible changes in the sample response over a longer time, a 20 ps delay interval is measured over 20 loops to see whether any loop-to-loop changes become apparent. All three measurements in fig. 44 are taken with a fluence of $F = 7.24 \frac{\text{mJ}}{\text{cm}^2}$. The loop number is encoded in the color with the first loop being represented by the darkest color and the last by the brightest. A clear trend can be observed in the first measurement, where the amplitude decreases visibly with the number of loops. This could be consistent with a charging effect that cause free charge carriers to vacate the already charged area due to Coulomb repulsion. However, the second measurement shows a slight trend in the opposite direction with the amplitude slightly increasing with the number of loops. Since the

third measurement shows no trend at all, it is questionable whether charging effects cause the inconsistent amplitudes as they cannot be reproduced.

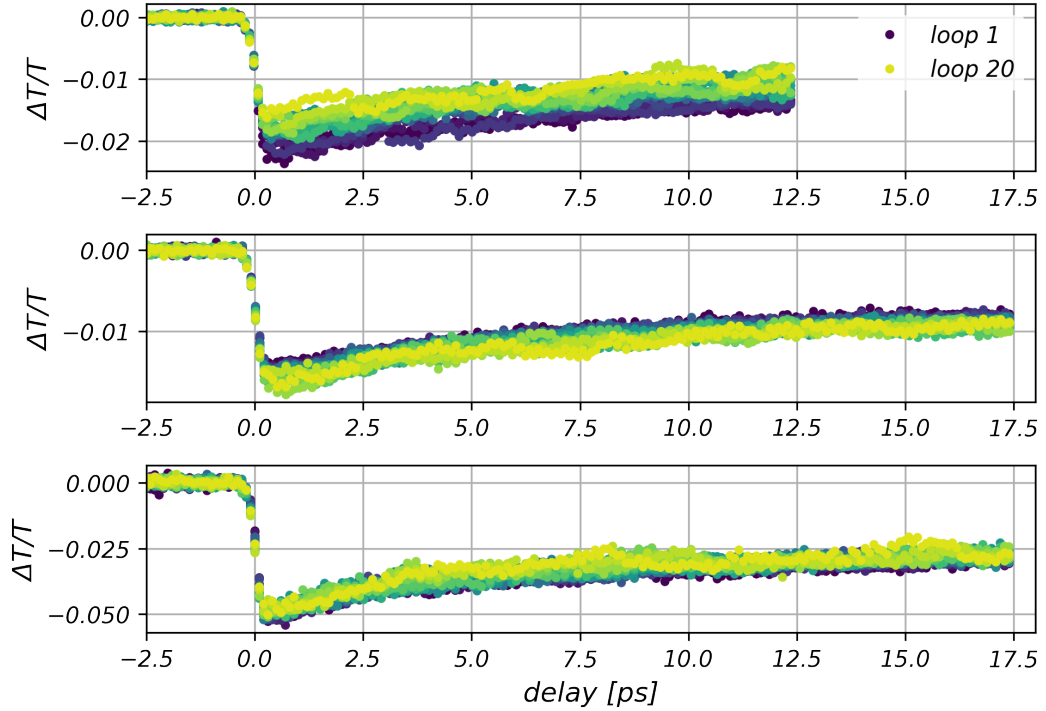


Figure 44: The three TIRAS measurements are taken with $F = 7.24 \frac{\text{mJ}}{\text{cm}^2}$, $\lambda_{\text{pump}} = 400 \text{ nm}$ and $\lambda_{\text{probe}} = 2200 \text{ nm}$. An interval of 20 ps is sampled with 20 loops in each measurement. The loops of each measurement are not averaged but plotted in one figure respectively. The darkest color corresponds to the first loop, and the brightest color corresponds to the 20th loop. The first two measurements exhibit opposing trends regarding the change in amplitude, while the last one does not show any trend.

It is important to note that the power of the pump beam frequently changed during the measurement, which was uncovered by monitoring the power before and after the measurements. This brings us back to the first hypothesis, which attributes the amplitude changes to an inconsistency in the pump laser power.

To further investigate power fluctuations as a source of error, a USB-capable power meter (Newport, Model 843-R USB) was added to the setup and placed in an unused part of the beam. It can therefore monitor the laser output power throughout the measurement without disturbing it. To match the measured powers to the transient signal, a timestamp was added to the data of the transient signal. Since the laser oscillator (MaiTai) also exhibits fluctuations regarding the central frequency, a drop in the pump power could also occur in the SHG process. Nevertheless, the pump beam power cannot be monitored after the SHG process without modifying the beam path. As a workaround, the monitoring of the spare beam path is continued, while also observing the oscillator's spectrum and the SHG power before and after the experiment.

Fig. 45 displays another measurement of multiple loops where a steady decrease of laser power throughout the measurement could be observed. At the same time,

4 Measurements and analysis

the amplitude clearly decreases over time. Even though there was no way to directly monitor the SHG beam, comparing the SHG power before and after the measurement reproduces the loss of about 0.8 mW from the probe beam. It is apparent that the loss over laser power causes the decrease in amplitude. This measurement was taken with the sample TiO₂-AuNP #2 that became available recently.

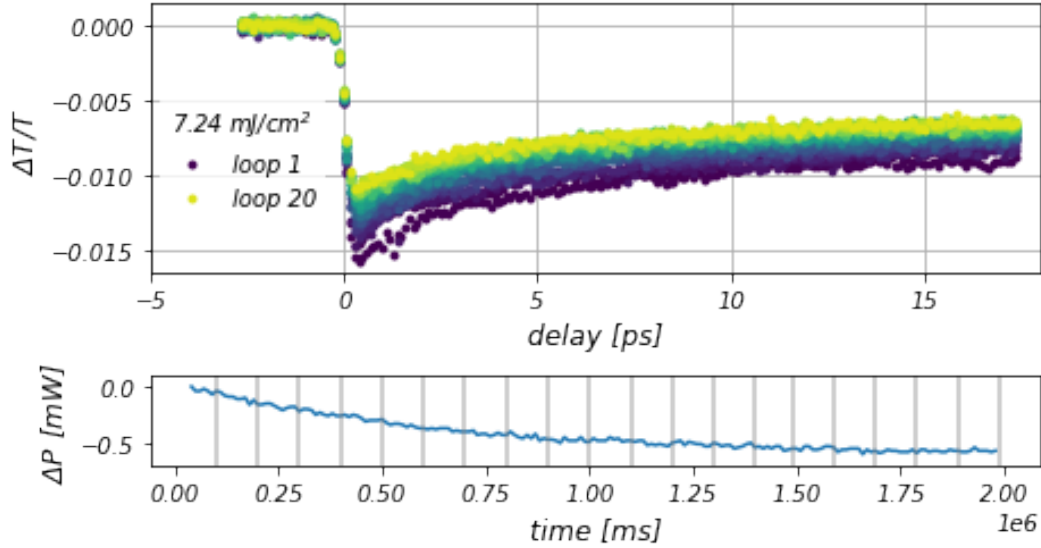


Figure 45: TIRAS measurement with $F = 7.24 \frac{\text{mJ}}{\text{cm}^2}$, $\lambda_{\text{pump}} = 400 \text{ nm}$ and $\lambda_{\text{probe}} = 2200 \text{ nm}$, and 20 loops. Below the transient signal, the monitored laser power during the measurement is plotted. The power was measured by taking the average of ten data points every ten seconds. The vertical gray lines mark the beginning of each new loop. The beginning of a loop was correlated to the elapsed time via the newly implemented timestamp in the transient raw data. Both the transient signal amplitude and the power decrease notably.

In fig. 46, the maximum amplitudes are plotted against the average power difference for the corresponding loop. One can see a clear correlation between the two values, suggesting that the change in signal truly depends on the change in laser power.

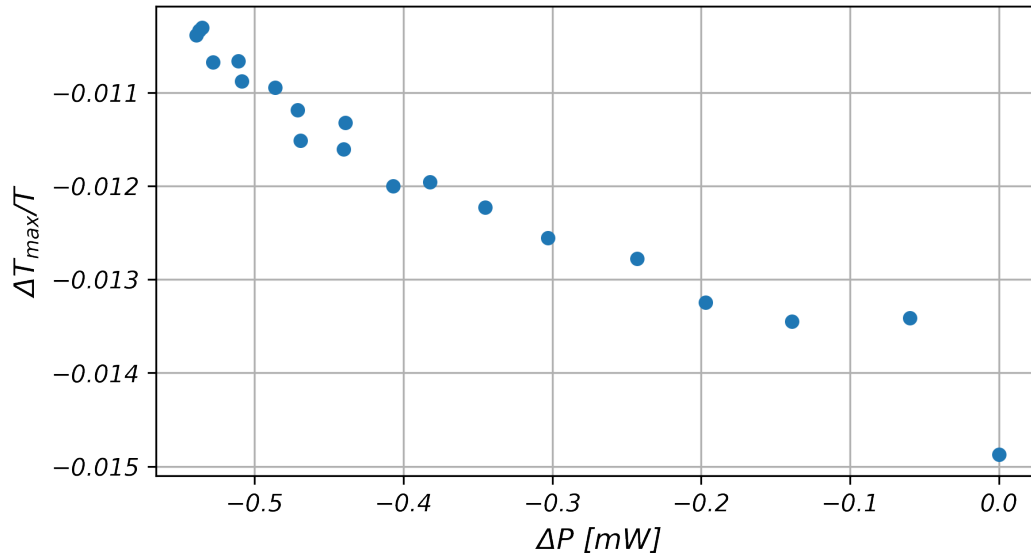


Figure 46: Maximum amplitude plotted against the change in the laser power ΔP during the measurement. ΔP was calculated as an average of all data points corresponding to the same loop. Amplitude and laser power are clearly correlated.

To see whether any changes could be observed with no drift in the laser power, the measurement in fig. 47 was selected, where neither the monitored laser power nor the SHG power varied during, before or after the measurement respectively. Since no changes in amplitude could be observed within this trace, it is very likely that no charging effects are present. Instead, the inconsistencies can be attributed to the fluctuations of the pump power.

4 Measurements and analysis

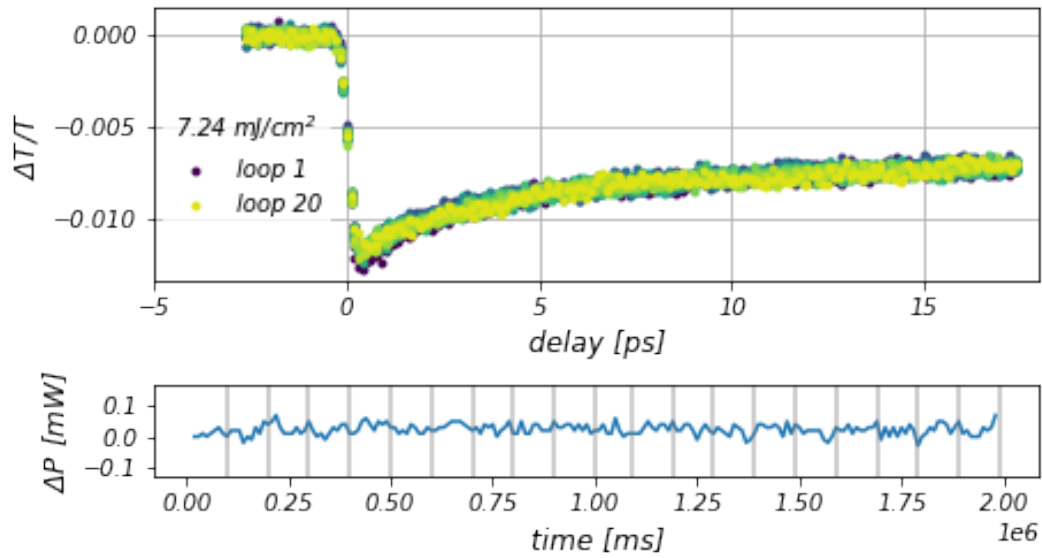


Figure 47: TIRAS measurement with $F = 7.24 \frac{\text{mJ}}{\text{cm}^2}$, $\lambda_{\text{pump}} = 400 \text{ nm}$ and $\lambda_{\text{probe}} = 2200 \text{ nm}$, and 20 loops. Below the transient signal, the monitored laser power during the measurement is plotted. The vertical gray lines mark the beginning of each new loop. Neither the transient signal amplitude nor the power decrease notably.

During the following measurements, the laser power was therefore continuously monitored, while also keeping an eye on the MaiTai Spectrum and comparing pump power before and after the measurement. As a precaution, the warm-up time for the laser was extended to two hours at minimum rather than the one hour that used to be standard for laser operation.

4.2.5 Results

Another fluence series was measured with the TiO₂-AuNP #2 sample. Six different fluences were set from low to high and the power has been monitored to record any significant drifts. After the last measurement, the Glen-laser prism and one of the telescope lenses in the pump beam path were exchanged due to laser injections. The shape of the pump beam profile (two examples in fig. 48) was consistent throughout the next fluence series but it slowly became larger with time.

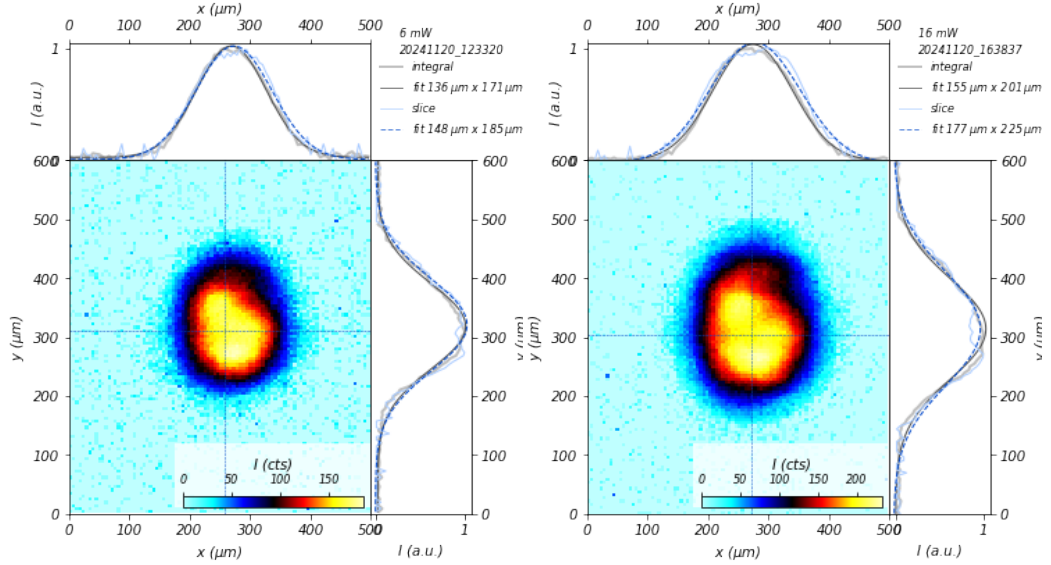


Figure 48: Beam profiles of the first and last measured fluences ($F = 4.6 \frac{\text{mJ}}{\text{cm}^2}$ and $F = 9.4 \frac{\text{mJ}}{\text{cm}^2}$ respectively). The shape of the beam profile is retained but the beam diameter becomes larger with time.

Fig. 49 displays the results of the fluence series. The delay ranges up to 118 ps and five loops were measured. For all fluences, the signal amplitude quickly reaches its maximum before decaying. Depending on the fluence the signal, the decay rate differs. One can observe the decay becoming faster for increasing fluences. At the lowest fluence of $F = 4.6 \frac{\text{mJ}}{\text{cm}^2}$ the signal barely bends before slowly decaying. Whereas at the highest fluence with $F = 9.4 \frac{\text{mJ}}{\text{cm}^2}$, the signal amplitude decays back to half its value within the first 10 ps. After about 80 ps, the signals decay steadily and are almost parallel to each other, indicating that they follow the same dynamic. The inset of fig. 49 shows the signals normalized to the maximum amplitude. The rise of the signal before the maximum is comparable for all fluences, indicating that the rise is faster than the temporal resolution of our setup. Only after the maximum when the decay begins, different dynamics emerge. Here, too, one can see that the highest fluence decays the fastest.

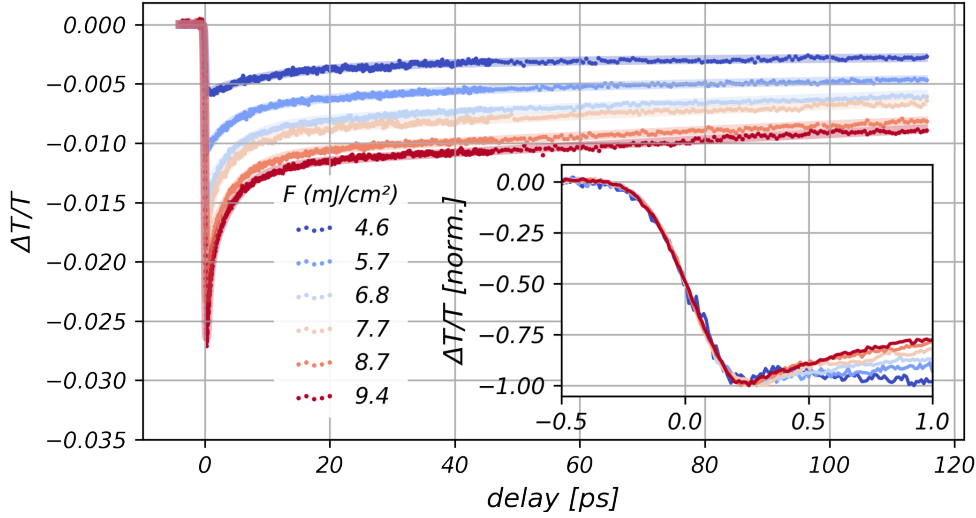


Figure 49: Fluence series with sample TiO₂- AuNP #2, $\lambda_{\text{pump}} = 400$ nm and $\lambda_{\text{probe}} = 2200$ nm. Six fluences were measured from low (blue) to high (red). Dots represent the measured data and the broad, slightly transparent line belongs to a tri-exponential fit. The fit parameters can be found in table 2 in the appendix. The inset shows the normalized data (lines). The rise of the signal aligns for all fluences. After the maximum amplitude, the different decay rates become visible.

Fig. 50 shows the maximum amplitude plotted against the fluence. This time, the amplitudes of the traces follow the increasing fluences, as expected initially. The relation seems to be linear. In ref. [44], a linear relation is found as well. Ratchford et al. also found a linear relation between fluence (\propto absorbed photon density), but did not correlate this behavior to a specific charge transfer mechanism. Zou et al., on the other hand, expected a charge transfer via tunneling, which would result in a nonlinear relation between amplitude and fluence. This expectation is not confirmed by our (and their own) measurements.

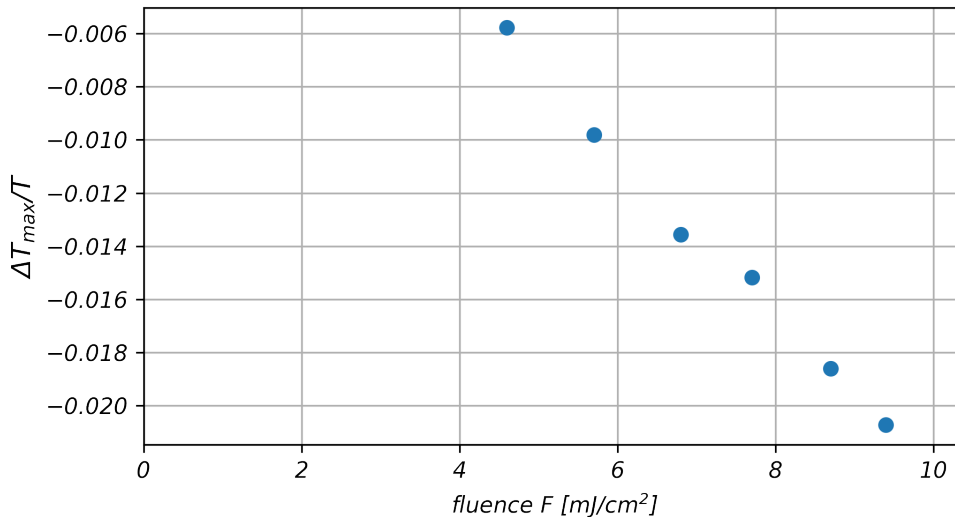


Figure 50: Maximum amplitudes of the fourth fluence series (fig. 49) plotted against the fluence. The maximum amplitude is determined from the mean of the first ten points after the maximum signal. The amplitude increases monotonously with the fluence, following a linear relationship.

The extinction spectra in fig. 29 shows a non-negligible extinction for the $\text{TiO}_2\#32$ sample at 400 nm. A clear signal from a the pump-probe measurement of this sample (see fig. 52) confirms that the sample does absorb the pump wavelength $\lambda_{\text{pump}} = 400$ nm. Assuming the sample resembles the TEM images of the similarly prepared TiO_2 & Au NP sample, the large fraction of TiO_2 without any Au adsorbed to the surface might also produce a significant signal. Consequently, a fluence series was taken to compare the results of the Au- TiO_2 sample to the behavior of pure TiO_2 . The fluences were selected to match the previous fluence series of the mixed sample. With the USB-capable power meter the laser power was monitored again, confirming a stable output throughout the measurement.

4 Measurements and analysis

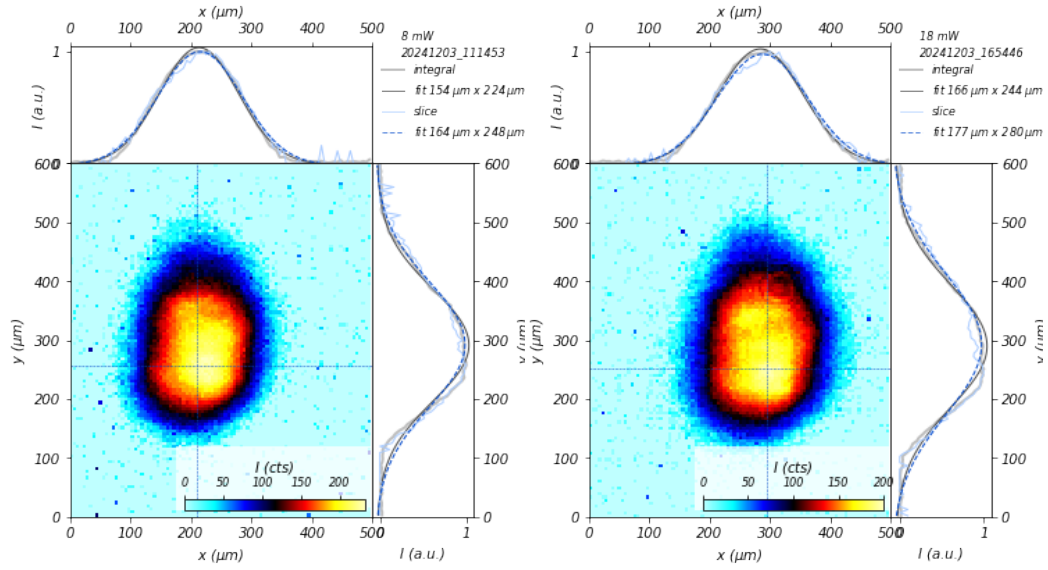


Figure 51: Beam profiles of the first and last measured fluences ($F = 4.5 \frac{\text{mJ}}{\text{cm}^2}$ and $F = 8.7 \frac{\text{mJ}}{\text{cm}^2}$ respectively). Shape and size of the beam profile are retained over time.

The results are displayed in fig. 52. Comparing both series, it is immediately noticeable that the amplitudes of the pure TiO_2 samples are larger by up to 50%. The quick decay that is observed in the sample with Au NPs for high fluences is not present in the TiO_2 results. The inset in fig. 49 again shows the first picosecond of the normalized signals. Up until the maximum amplitude is reached, the dynamics seem to be the same for every fluence as well. Contrary to the dynamics of the mixed sample, the highest fluence shows the slowest decay directly after the maximum.

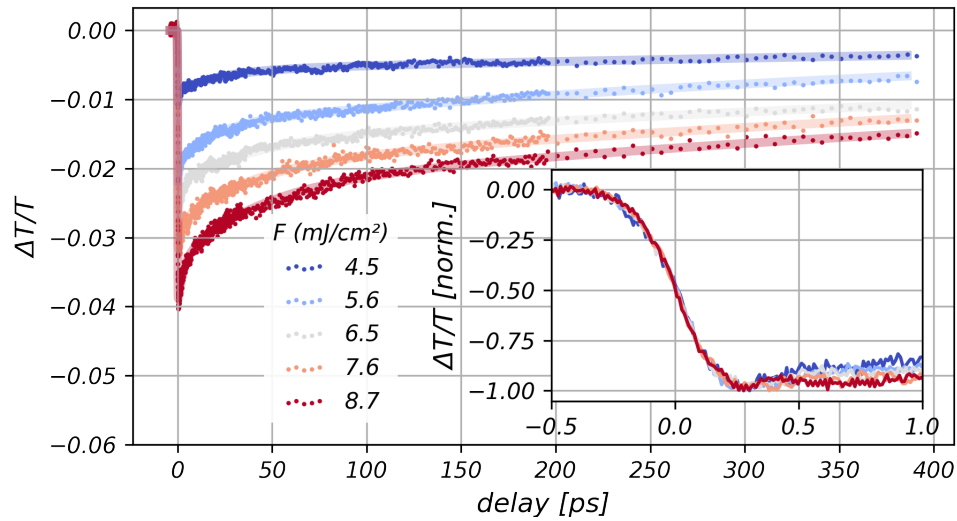


Figure 52: Fluence series of pure TiO_2 NPs with $\lambda_{\text{pump}} = 400 \text{ nm}$ and $\lambda_{\text{probe}} = 2200 \text{ nm}$. Five different fluences were measured. Points represent the measured data and the broader, transparent lines illustrate the tri-exponential fits. Inset presents the normalized traces within the first picosecond where the measurements seem to produce the same dynamics. Lines instead of points were chosen for better readability.

The maximum amplitudes reproduce linear trend, if the first point is considered to be an outlier. They are plotted in fig. 53. Since TiO_2 can be directly excited by the 400 nm pump beam and electrons from trap states can also be excited into the CB, the linear relation with the fluence is reasonable. The more photons are available to excite the sample over the band gap, the more electrons can be probed in the conduction band.

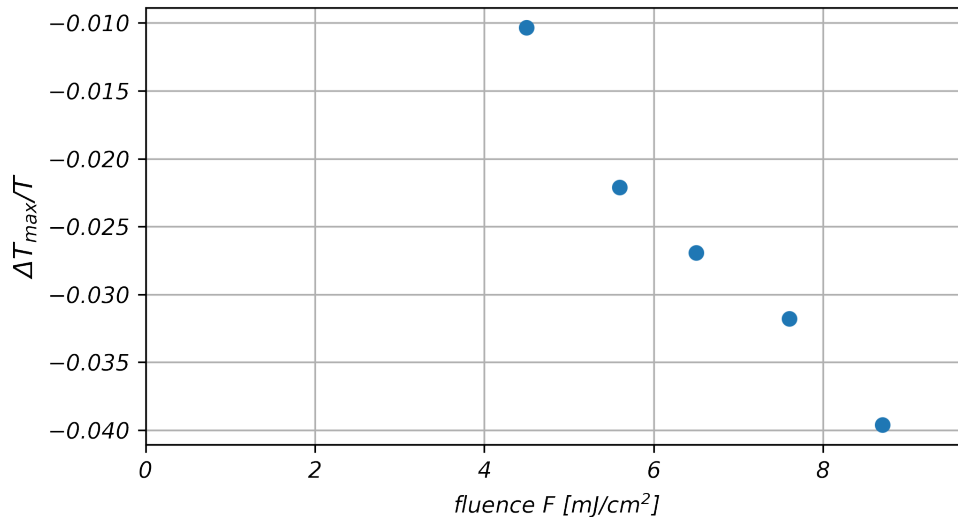


Figure 53: Maximum amplitudes calculated from the mean of the first ten points after maximum are plotted against the fluence. A linear relation is indicated.

To compare the change in dynamics caused by the addition of Au NPs to the TiO_2 NPs, the traces of both samples are plotted together for matching fluences in fig. 54. All signals are normalized to their maximum amplitude respectively. For small fluences, the signals seem to be very similar. For increasingly large fluences, however, the deviation in the dynamics becomes more apparent. Especially within the first 20 ps, the signals behave very differently while they seem to decay with the same rate after about 80 ps, where the signals only show an offset but are parallel otherwise.

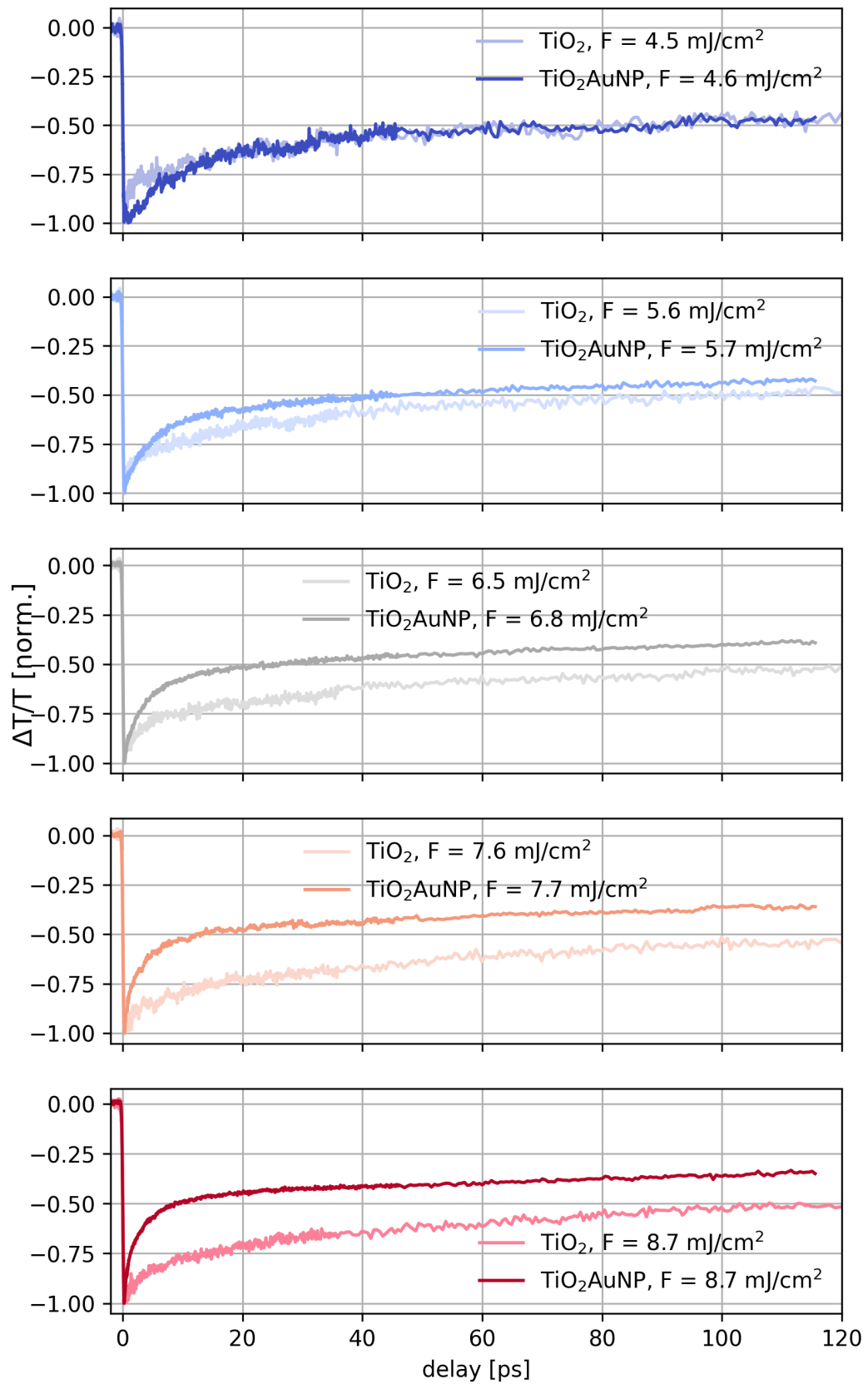


Figure 54: Transient absorption spectra of Au- TiO_2 NP (fluence series in fig. 49) and only TiO_2 (fluence series in fig. 52) plotted together for matching fluences. All signals are normalized to their maximum amplitude respectively.

4 Measurements and analysis

In order to take a closer look at the differences caused by the Au NPs, the signals are normalized to their respective value at later time delays where the dynamics seem to match. Subsequently, the TiO₂ signals are subtracted from the Au-TiO₂ NP signals for the respective fluences. These differences are plotted in fig. 55. Because the signals are not measured with the exact same delays, they had to be interpolated in order to calculate the difference. This unfortunately introduces additional noise, which is especially obstructive for the already noisy signals at small fluences. To obtain a smoother difference signal, the traces of both fluence series were fitted with tri-exponential functions without explicit physical meaning. Similar measurements in literature are often fitted with mono-, bi- or tri-exponential functions, sometimes also combining them with offsets [28, 26, 15, 44, 14, 5]. The tri-exponential function was chosen because it fits the data best. At first glance, the observations already made on fig. 54 are reproduced. For higher fluences, the signal difference shows a very fast decay that becomes slower for lower fluences. The differences in normalized amplitudes also seem to increase with fluence. Some of the difference signals do not just decay up to zero but also contain a positive contribution before reaching zero. Normalizing to the tail of the signal causes the amplitude of the Au-TiO₂ sample to exceed the TiO₂ sample. Due to the faster dynamics of the sample including the Au NPs, the normalized signal of the AuTiO₂ sample actually decreases below the TiO₂ signal amplitude at some point, causing a positive contribution in the difference. Fitting another exponential function to the difference signals to identify the different decay times did not work due to the change in sign.

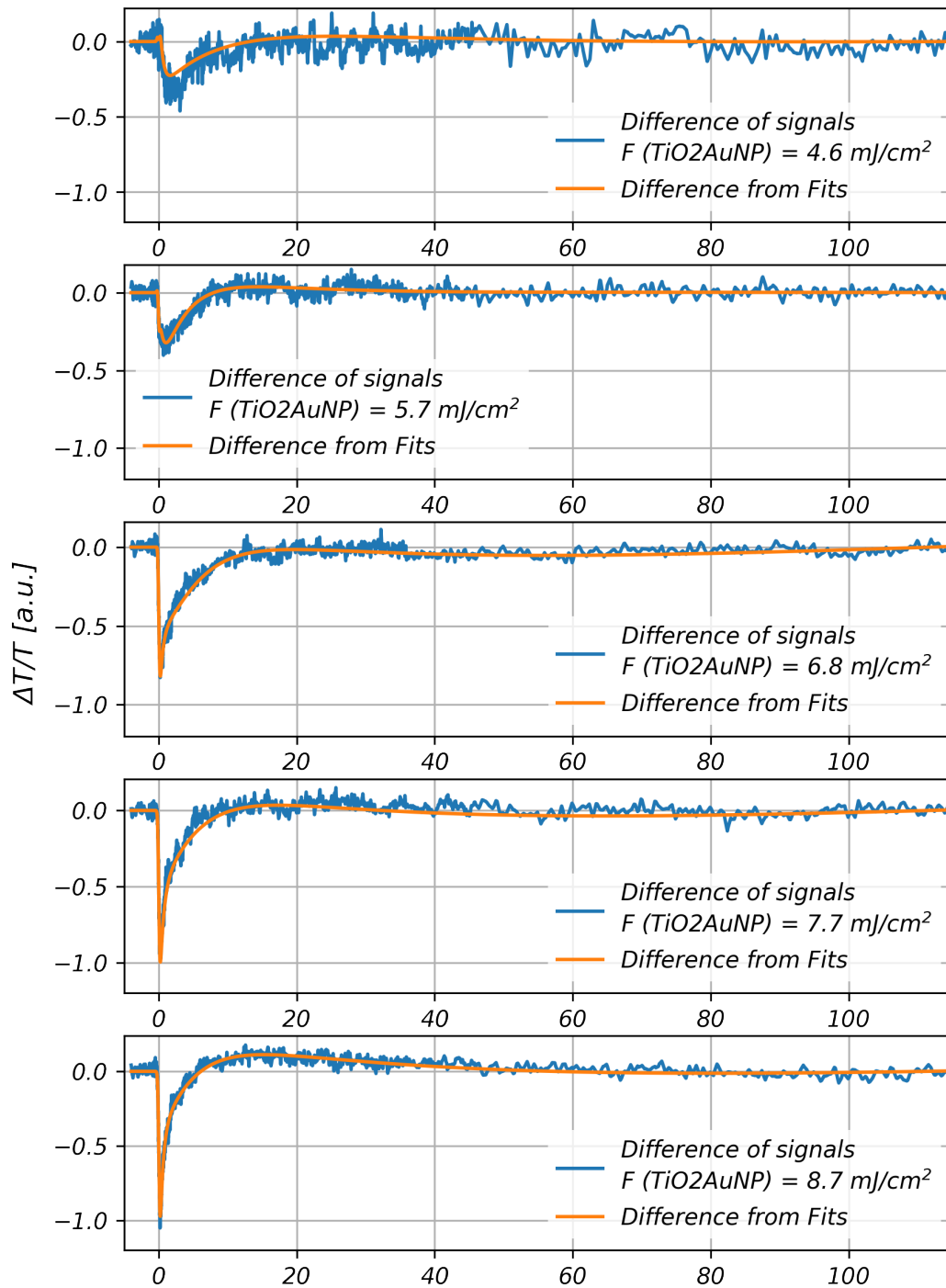


Figure 55: Difference signals of the previous two fluence series on TiO_2 and Au-TiO_2 NPs. The signals of both samples were normalized to their respective value at 115 ps, so that the tails of both signals converges to the same value. Then, the signal of the pure TiO_2 sample was subtracted from the sample with Au NPs (blue) for each matching fluence to uncover the influence that the Au NPs have on the dynamics. For the calculation of the differences, the data had to be interpolated which adds noise. To obtain a smoother signal, the tri-exponential fits were also subtracted (orange). The differences of the fits cross the y-axis at 15, 7, 17, 10, and 5 ps respectively, considering the fluences low to high.

4 Measurements and analysis

I hypothesize that the larger amplitude difference of the normalized signals and the faster decay for higher fluences can be attributed to a back-transfer of electrons from the TiO_2 conduction band to the Au NPs. A higher fluence would produce more carriers in the CB that might be able cross the barrier either to stronger Coulomb repulsion or a different occupation statistic of the conduction band. The hypothesis on the back-transfer of electrons needs to be further investigated for a definitive conclusion.

Camargo et al. investigated charge transfer between Au NPs and CdSe rods in ref. [5]. They observed that upon the excitation of the Au plasmon resonance an electron is quickly (30 fs) transferred to CdSe. On a time scale of about 200 fs a back-transfer of electrons from the Au NPs to the CdSe was observed. Exciting the CdSe rods directly resulted in the transfer of electrons to the Au NPs. They fitted their transient absorption kinetics with a tri-exponential function as well. However, their dynamics contained two sub-picosecond contributions and one contribution on the scale of about 2 ps. Combining TAS with 2D electron spectroscopy gave them the opportunity to gain insights on the various excitation and relaxation processes taking place.

5 Conclusion

Within the scope of this thesis, an experiment for the study of charge transfer between gold and TiO₂ nanoparticles was set up. Therefore, either the TiO₂ or Au is excited by a visible pump, and the charges in the conduction band of TiO₂ are measured by IR absorption. To this end, the visible NOPA was optimized, and the IR NOPA was adjusted for regular use. Transient IR absorption spectroscopy on the TiO₂ and TiO₂-AuNP samples was first carried out with the more stable 400 nm SHG as a pump beam. Measuring the fluence series revealed problems with the setup regarding beam profile and stability. Difficulties with the beam profile were addressed by lowering the laser power and replacing damaged optical elements in the beam path. Unexpected behavior of the signal amplitudes with respect to the fluences caused the hypothesis of observing charging effects during the measurements. Adding a power meter to the setup revealed drifts in the laser power, which are the likely source of inconsistencies regarding the signal amplitudes. By monitoring the laser power during the measurement, a fluence series without significant drifts of the laser power was obtained for pure TiO₂ and TiO₂-AuNP respectively. In both series, the amplitude and fluence exhibit a linear relationship. This indicates the absence of tunneling regarding charge transfer and thermal excitation processes. It was possible to fit the traces with tri-exponential functions but due to the complex dynamics, no interpretation of the fitting parameters is possible at this point. Especially for transient measurements of mixed phase TiO₂ pumped with 400 nm, literature has no conclusive explanation for the observed dynamics either. Comparing the signals of pure TiO₂ and of TiO₂-AuNP samples at matching fluences, the samples containing AuNPs exhibit a faster decay directly after excitation. The faster decay indicates a significant back transfer of electrons from the TiO₂ CB to the AuNP. Higher fluences cause a faster decay of the signal but the signals seem to be converging to the same dynamics on a timescale of about 100 ps.

For future investigations, measurements with a pump wavelength of 570 nm would be very interesting. This wavelength would correspond to the sample's plasmon resonance. Since Brown et al. argued that the excited plasmon in Au mainly decays to the interband transitions [4], which were already excited with the 400 nm pump, it would be interesting to see the influence of the plasmon excitation on the dynamics. Another reason for using this slightly longer pump wavelength is to avoid the direct excitation of TiO₂ over the band gap. However, the extinction spectrum indicates that the P25 NPs will absorb photons from the whole visible range if the signal is not caused by scattering. Of course, the absorption decreases with longer wavelengths, but due to a high number of interface and surface states, it might still be significant. To reduce the direct pumping of the semiconductor, one could use only anatase TiO₂ with the larger band gap of 3.2 eV. Avoiding the in-gap states, however, might call for a different production process of the TiO₂NPs.

6 Appendix

Setup of the vis-NOPA

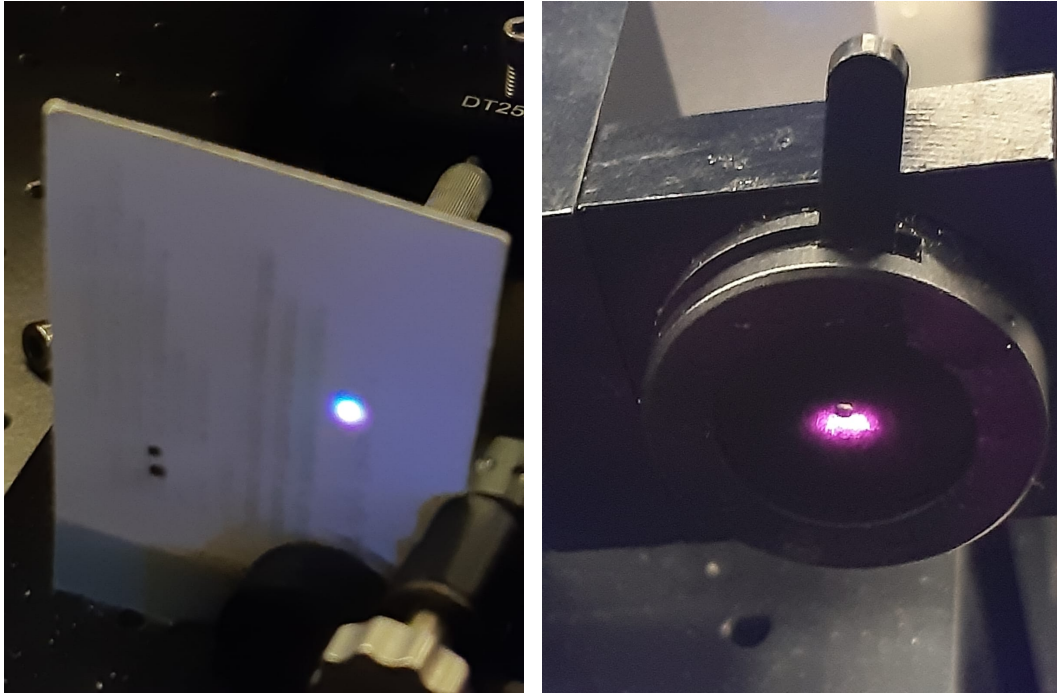


Figure 56: WLG in the vis-NOPA setup. Right: WL on a business card behind the collimating lens L4. Left: Aperture A3 closed after aligning the WL as described in section 3.3.1. The fundamental 800 nm does not go through the center of the aperture even though it goes through the center of lens L3, which is glued to aperture A3.

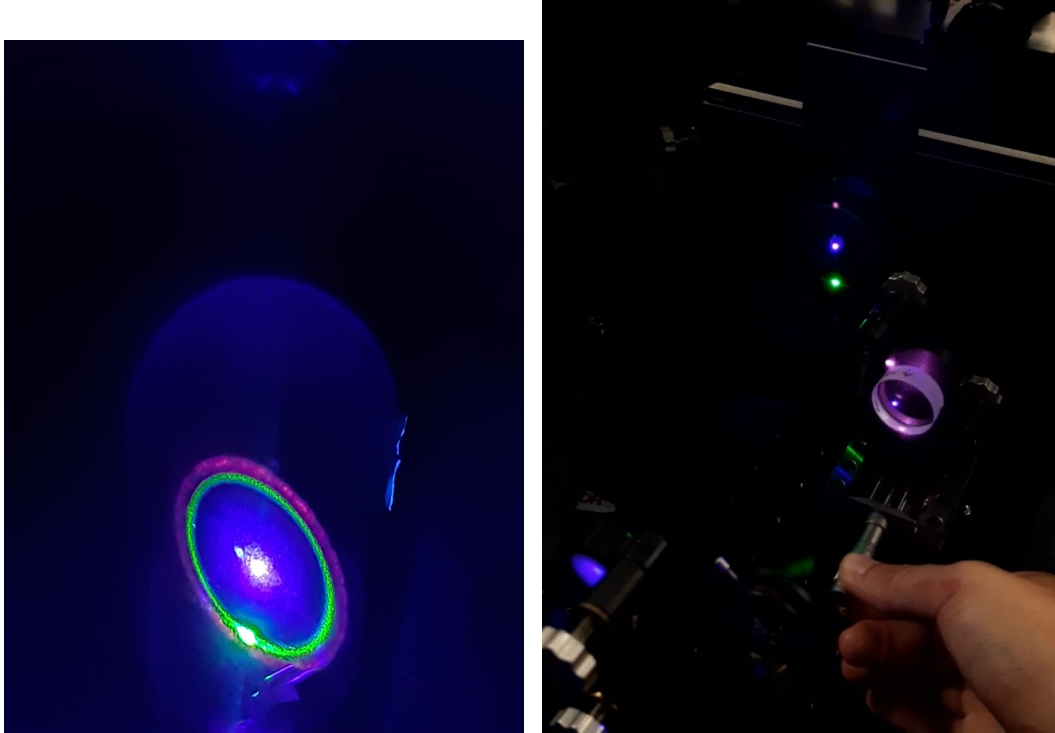


Figure 57: Left: Fluorescence cone before optimizing the tilting angle. The cone is broad and the colors arrive at different diameters. Right: Depleted cone with spatial and temporal overlap. The lowest spot is the amplified signal beam, the middle is the pump beam and the top spot is the IR idler that is only visible through the camera. Turning the setscrew of mirror M3 (on the right side of the picture) adjusts the output wavelength by changing the temporal overlap.

Beam profile of the IR NOPA

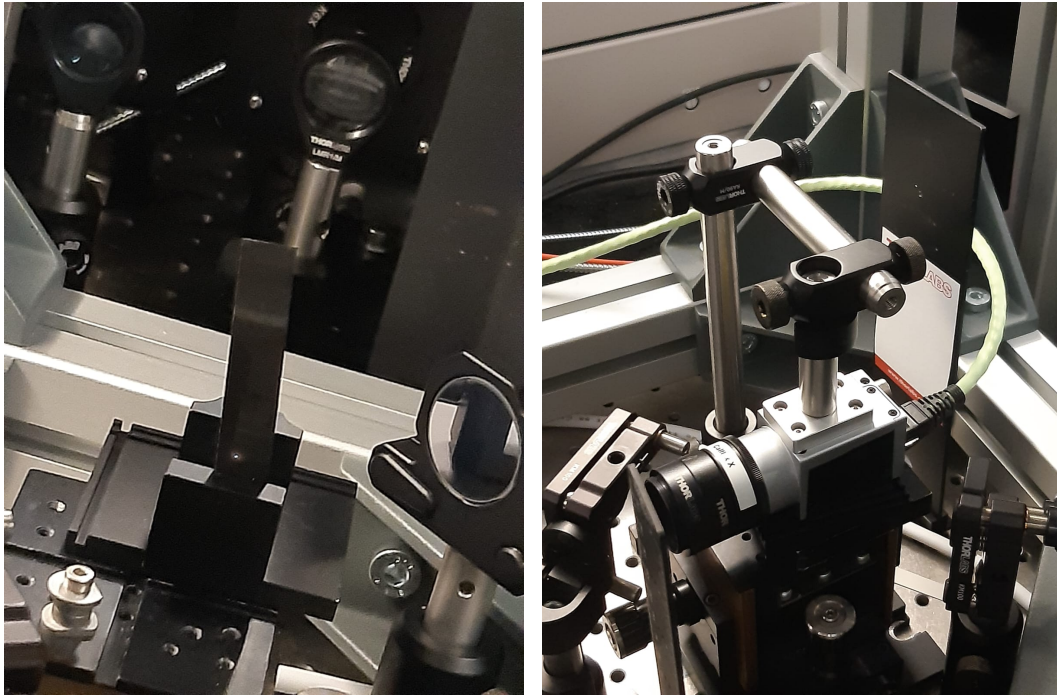


Figure 58: Left: Thermopaper is clamped into the sample holder. The white spot is caused by the IR NOPA output. Right: The camera was moved to the sample spot (where the thermopaper is clamped in the left picture) to record a beam profile of the IR NOPA output.

Fitting parameters of the TiO₂ and TiO₂AuNP fluence series

The tri-exponential function follows eq. 26.

$$f(t) = \sum_{i=1}^3 a_i \cdot \exp(-t/\tau_i) \quad (26)$$

| $F \left[\frac{\text{mJ}}{\text{cm}^2} \right]$ | $\tau_1 [ps]$ | $\tau_2 [ps]$ | $\tau_3 [ps]$ | $a_1 \cdot 10^3$ | $a_2 \cdot 10^3$ | $a_3 \cdot 10^3$ |
|--|---------------------------|---------------------------|-----------------------|--------------------------|--------------------------|-----------------------------|
| 4.6 | $8.0_{-1.6}^{+1.5}$ | $19.2_{-4.7}^{+12}$ | 690_{-130}^{+410} | $-1.28_{-0.56}^{+}$ | $-1.26_{-0.51}^{+0.51}$ | $-3.29_{-0.11}^{+0.20}$ |
| 5.7 | $3.77_{-0.18}^{+0.16}$ | $22.6_{-3.6}^{+4.8}$ | 570_{-72}^{+140} | $-3.36_{-0.13}^{+0.15}$ | $-1.79_{-0.12}^{+0.10}$ | $-5.67_{-0.15}^{+0.21}$ |
| 6.8 | $0.432_{-0.060}^{+0.071}$ | $4.94_{-0.14}^{+0.16}$ | $329.4_{-4.9}^{+5.1}$ | $-3.64_{-0.30}^{+0.22}$ | $-5.83_{-0.13}^{+0.14}$ | $-8.365_{-0.022}^{+0.023}$ |
| 7.7 | $0.529_{-0.029}^{+0.030}$ | $4.691_{-0.098}^{+0.11}$ | $340.1_{-4.9}^{+5.1}$ | $-5.67_{-0.16}^{+0.15}$ | $-6.461_{-0.11}^{+0.11}$ | $-9.154_{-0.021}^{+0.021}$ |
| 8.7 | $0.427_{-0.019}^{+0.019}$ | $4.372_{-0.073}^{+0.075}$ | $379.0_{-5.1}^{+5.2}$ | $-9.24_{-0.25}^{+0.23}$ | $-8.50_{-0.12}^{+0.12}$ | $-11.011_{-0.021}^{+0.021}$ |
| 9.4 | $0.422_{-0.016}^{+0.017}$ | $4.052_{-0.067}^{+0.069}$ | $370.5_{-4.9}^{+5.1}$ | $-12.17_{-0.30}^{+0.28}$ | $-9.66_{-0.14}^{+0.14}$ | $-12.050_{-0.023}^{+0.023}$ |

Table 2: Decay times τ and amplitudes a from the triexponential fit of the fluence series with sample TiO₂- AuNP #2 (dataset displayed in fig. 49).

| $F \left[\frac{\text{mJ}}{\text{cm}^2} \right]$ | $\tau_1 [ps]$ | $\tau_2 [ps]$ | $\tau_3 [ps]$ | $a_1 \cdot 10^3$ | $a_2 \cdot 10^3$ | $a_3 \cdot 10^3$ |
|--|---------------------------|-------------------------|-------------------|-------------------------|--------------------------|-----------------------------|
| 4.5 | $0.482_{-0.049}^{+0.052}$ | $22.6_{-0.99}^{+1.1}$ | 830_{-42}^{+47} | $-3.38_{-0.34}^{+0.28}$ | $-3.099_{-0.5}^{+0.59}$ | $-5.73_{-0.062}^{+0.067}$ |
| 5.6 | $0.563_{-0.059}^{+0.062}$ | $18.50_{-0.74}^{+0.77}$ | 533_{-12}^{+13} | $-5.44_{-0.44}^{+0.36}$ | $-5.740_{-0.92}^{+0.93}$ | $-13.609_{-0.091}^{+0.092}$ |
| 6.5 | $1.96_{-0.13}^{+0.14}$ | $38.2_{-2.3}^{+2.5}$ | 970_{-49}^{+56} | $-4.91_{-0.13}^{+0.13}$ | $-6.17_{-0.16}^{+0.16}$ | $-16.11_{-0.19}^{+0.21}$ |
| 7.6 | $2.64_{-0.31}^{+0.34}$ | $37.8_{-2.6}^{+2.9}$ | 896_{-45}^{+53} | $-4.43_{-0.18}^{+0.18}$ | $-8.27_{-0.21}^{+0.21}$ | $-19.65_{-0.26}^{+0.28}$ |
| 8.7 | $3.26_{-0.28}^{+0.29}$ | $41.8_{-2.8}^{+3.1}$ | 940_{-53}^{+64} | $-6.35_{-0.22}^{+0.22}$ | $-10.81_{-0.25}^{+0.24}$ | $-22.52_{-0.34}^{+0.37}$ |

Table 3: Decay times τ and amplitudes a from the triexponential fit of the fluence series with sample TiO₂ #32 (dataset displayed in fig. 52).

Bibliography

- [1] Florian Baltrusch. “balt2022bsc”. Universität Potsdam, 2022. URL: https://www.uni-potsdam.de/fileadmin/projects/udkm/Documents/BaMa_theses/balt2022bsc.pdf (visited on 12/05/2024).
- [2] *BBO Crystals - Beta Barium Borate / EKSMA Optics*. URL: <https://eksmaoptics.com/nonlinear-and-laser-crystals/nonlinear-crystals/beta-barium-borate-bbo-crystals/> (visited on 01/21/2025).
- [3] Robert W. Boyd. *Nonlinear Optics*. Ed. by Robert W. Boyd. Burlington: Academic Press, 2008. ISBN: 978-0-12-369470-6. DOI: 10.1016/B978-0-12-369470-6.00001-0.
- [4] Ana M. Brown et al. “Nonradiative Plasmon Decay and Hot Carrier Dynamics: Effects of Phonons, Surfaces, and Geometry”. In: *ACS Nano* 10.1 (2016), pp. 957–966. DOI: 10.1021/acsnano.5b06199.
- [5] Franco V. A. Camargo et al. “Visualizing Ultrafast Electron Transfer Processes in Semiconductor–Metal Hybrid Nanoparticles: Toward Excitonic–Plasmonic Light Harvesting”. In: *Nano Letters* 21.3 (2021), pp. 1461–1468. DOI: 10.1021/acs.nanolett.0c04614.
- [6] Giulio Cerullo and Sandro De Silvestri. “Ultrafast Optical Parametric Amplifiers”. In: *Review of Scientific Instruments* 74.1 (2003), pp. 1–18. DOI: 10.1063/1.1523642.
- [7] Zijian Cui et al. “Phase Matching Using the Linear Electro-Optic Effect”. In: *Physical Review Letters* 118.4 (2017), p. 043901. DOI: 10.1103/PhysRevLett.118.043901.
- [8] Audrius Dubietis and Arnaud Couairon. *Ultrafast Supercontinuum Generation in Transparent Solid-State Media*. SpringerBriefs in Physics. Cham: Springer International Publishing, 2019. ISBN: 978-3-030-14994-9 978-3-030-14995-6. DOI: 10.1007/978-3-030-14995-6.
- [9] Mykhaylo Evstigneev. *Introduction to Semiconductor Physics and Devices*. Cham: Springer International Publishing, 2022. ISBN: 978-3-031-08457-7 978-3-031-08458-4. DOI: 10.1007/978-3-031-08458-4.
- [10] Isioma M. Ezech et al. “Effect of Titanium Oxide (TiO₂) on Natural Dyes for the Fabrication of Dye-Sensitized Solar Cells”. In: *Engineering Proceedings* 63.1 (1 2024), p. 25. DOI: 10.3390/engproc2024063025.
- [11] R. H. Fowler. “The Analysis of Photoelectric Sensitivity Curves for Clean Metals at Various Temperatures”. In: *Physical Review* 38.1 (1931), pp. 45–56. DOI: 10.1103/PhysRev.38.45.
- [12] Akira Fujishima and Kenichi Honda. “Electrochemical Photolysis of Water at a Semiconductor Electrode”. In: *Nature* 238.5358 (1972), pp. 37–38. DOI: 10.1038/238037a0.
- [13] Akihiro Furube et al. “Ultrafast Plasmon-Induced Electron Transfer from Gold Nanodots into TiO₂ Nanoparticles”. In: *Journal of the American Chemical Society* 129.48 (2007), pp. 14852–14853. DOI: 10.1021/ja076134v.

Bibliography

- [14] Nandan Ghorai et al. “Efficient Size-Dependent Hot Electron Transfer from Au to TiO₂ Nanoparticles”. In: *Nano Letters* 25.8 (2025), pp. 3253–3258. DOI: 10.1021/acs.nanolett.4c06154.
- [15] Yocef Hattori et al. “Simultaneous Hot Electron and Hole Injection upon Excitation of Gold Surface Plasmon”. In: *The Journal of Physical Chemistry Letters* 10.11 (2019), pp. 3140–3146. DOI: 10.1021/acs.jpcllett.9b01085.
- [16] J. S. Helman and F. Sánchez-Sinencio. “Theory of Internal Photoemission”. In: *Physical Review B* 7.8 (1973), pp. 3702–3706. DOI: 10.1103/PhysRevB.7.3702.
- [17] Ursula Keller. *Ultrafast Lasers: A Comprehensive Introduction to Fundamental Principles with Practical Applications*. Graduate Texts in Physics. Cham: Springer International Publishing, 2021. ISBN: 978-3-030-82531-7 978-3-030-82532-4. DOI: 10.1007/978-3-030-82532-4.
- [18] Mareike Kiel. “Static and Ultrafast Optical Properties of Nanolayered Composites. Gold Nanoparticles Embedded in Polyelectrolytes”. Universität Potsdam, 2012. URL: https://www.uni-potsdam.de/fileadmin/projects/udkm/Documents/PhD_theses/kiel2012phd.pdf (visited on 12/05/2024).
- [19] Young Keun Lee et al. “Surface Plasmon-Driven Hot Electron Flow Probed with Metal-Semiconductor Nanodiodes”. In: *Nano Letters* 11.10 (2011), pp. 4251–4255. DOI: 10.1021/nl2022459.
- [20] Andrew J. Leenheer et al. “Solar Energy Conversion via Hot Electron Internal Photoemission in Metallic Nanostructures: Efficiency Estimates”. In: *Journal of Applied Physics* 115.13 (2014), p. 134301. DOI: 10.1063/1.4870040.
- [21] Ajay P. Manuel and Karthik Shankar. “Hot Electrons in TiO₂–Noble Metal Nano-Heterojunctions: Fundamental Science and Applications in Photocatalysis”. In: *Nanomaterials* 11.5 (5 2021), p. 1249. DOI: 10.3390/nano11051249.
- [22] Jianping Meng, Chengkuo Lee, and Zhou Li. “Adjustment Methods of Schottky Barrier Height in One- and Two-Dimensional Semiconductor Devices”. In: *Science Bulletin* 69.9 (2024), pp. 1342–1352. DOI: 10.1016/j.scib.2024.03.003.
- [23] S. Mitzscherling et al. “Dielectric Function of Two-Phase Colloid–Polymer Nanocomposite”. In: *Physical Chemistry Chemical Physics* 17.44 (2015), pp. 29465–29474. DOI: 10.1039/C5CP04326C.
- [24] Syed Mubeen et al. “Plasmonic Photosensitization of a Wide Band Gap Semiconductor: Converting Plasmons to Charge Carriers”. In: *Nano Letters* 11.12 (2011), pp. 5548–5552. DOI: 10.1021/nl203457v.
- [25] *Optical Constants of BaB₂O₄ (Barium Borate, BBO)*. RefractiveIndex.info. URL: <https://refractiveindex.info/?shelf=main&book=BaB204&page=Tamosauskas-o>.
- [26] Behnaz Ostovar et al. “The Role of the Plasmon in Interfacial Charge Transfer”. In: *Science Advances* 10.27 (2024), eadp3353. DOI: 10.1126/sciadv.adp3353.

- [27] Dimitar A. Panayotov, Steven P. Burrows, and John R. Morris. “Infrared Spectroscopic Studies of Conduction Band and Trapped Electrons in UV-Photoexcited, H-Atom n-Doped, and Thermally Reduced TiO₂”. In: *The Journal of Physical Chemistry C* 116.7 (2012), pp. 4535–4544. DOI: 10.1021/jp2053103.
- [28] Daniel C. Ratchford et al. “Quantification of Efficient Plasmonic Hot-Electron Injection in Gold Nanoparticle–TiO₂ Films”. In: *Nano Letters* 17.10 (2017), pp. 6047–6055. DOI: 10.1021/acs.nanolett.7b02366.
- [29] *Rotationsellipsoid*. In: *Wikipedia*. 2024. URL: <https://de.wikipedia.org/w/index.php?title=Rotationsellipsoid&oldid=247368983> (visited on 03/17/2025).
- [30] Claude Rullière. *Femtosecond Laser Pulses: Principles and Experiments*. 2nd ed. Springer Science and Business Media, 2005. ISBN: 0-387-01769-0.
- [31] N. Serpone, D. Lawless, and R. Khairutdinov. “Size Effects on the Photophysical Properties of Colloidal Anatase TiO₂ Particles: Size Quantization versus Direct Transitions in This Indirect Semiconductor?” In: *The Journal of Physical Chemistry* 99.45 (1995), pp. 16646–16654. DOI: 10.1021/j100045a026.
- [32] Olaf Stenzel. “Basic Effects of Nonlinear Optics”. In: *Light–Matter Interaction: A Crash Course for Students of Optics, Photonics and Materials Science*. Ed. by Olaf Stenzel. Cham: Springer International Publishing, 2022, pp. 471–494. ISBN: 978-3-030-87144-4. DOI: 10.1007/978-3-030-87144-4_18.
- [33] Felix Stete. “Gold at the Nanoscale: Plasmon-Exciton Coupling and Optical Heating”. Universität Potsdam, 2021, 38231 KB, X, 186 pages. DOI: 10.25932/PUBLISHUP-49605.
- [34] Felix Stete, M. Bargheer, and Wouter Koopman. *Optical Non-linearities in Plasmon-Exciton Core-Shell Particles: The Role of Heat*. 2020. DOI: 10.48550/arXiv.2009.00075.
- [35] Ludwig K. Thomas. *Solid State Physics: Festkörper*. Vol. 6. Bergmann - Schaefer. Berlin/Boston: De Gruyter, Inc, 2008. 1 p. ISBN: 978-3-11-017485-4 978-3-11-019815-7.
- [36] Raymond T. Tung. “The Physics and Chemistry of the Schottky Barrier Height”. In: *Applied Physics Reviews* 1.1 (2014), p. 011304. DOI: 10.1063/1.4858400.
- [37] Kosei Ueno and Hiroaki Misawa. “Plasmon-Enhanced Photocurrent Generation and Water Oxidation from Visible to near-Infrared Wavelengths”. In: *NPG Asia Materials* 5.9 (2013), e61–e61. DOI: 10.1038/am.2013.42.
- [38] Daniel Wegkamp. “Schnelle Elektrodynamiken an Grenzflächen untersucht mit einer NOPA-basierenden Femtosekunden-Lichtquelle”. Diplomarbeit. Berlin: Freie Universität Berlin, 2009.
- [39] Xiaole Weng et al. “Thermocatalytic Syntheses of Highly Defective Hybrid Nano-catalysts for Photocatalytic Hydrogen Evolution”. In: *J. Mater. Chem. A* 5 (2017). DOI: 10.1039/C7TA07808K.
- [40] Kristina Wilson. *Guide to NOPAs*. URL: https://www.sas.rochester.edu/chm/groups/mccamant/assets/pdf/documents_nopa.pdf.

Bibliography

- [41] Bo Xiang et al. “Ultrafast Direct Electron Transfer at Organic Semiconductor and Metal Interfaces”. In: *Science Advances* 3.11 (2017), e1701508. DOI: 10.1126/sciadv.1701508.
- [42] Yangyang Yu et al. “Synergistic Effect of Cu Single Atoms and Au–Cu Alloy Nanoparticles on TiO₂ for Efficient CO₂ Photoreduction”. In: *ACS Nano* 15.9 (2021), pp. 14453–14464. DOI: 10.1021/acsnano.1c03961.
- [43] Chao Zhan et al. “From Plasmon-Enhanced Molecular Spectroscopy to Plasmon-Mediated Chemical Reactions”. In: *Nature Reviews Chemistry* 2.9 (2018), pp. 216–230. DOI: 10.1038/s41570-018-0031-9.
- [44] Xianshao Zou et al. “Photophysical Study of Electron and Hole Trapping in TiO₂ and TiO₂ /Au Nanoparticles through a Selective Electron Injection”. In: *The Journal of Physical Chemistry C* 126.50 (2022), pp. 21467–21475. DOI: 10.1021/acs.jpcc.2c07021.

7 Authorship declaration

I hereby declare that I have prepared this master thesis independently, have not submitted it elsewhere for examination purposes and have not used any aids other than those specified. All knowingly used text excerpts, quotations or contents of other authors have been explicitly marked as such.

Potsdam, 24.03.2025

Lisa Mehner

8 Acknowledgments

Completing my master's thesis has been a significant milestone in my academic journey, marking an exciting and challenging first step towards working independently in science. I am deeply grateful to all the people who have supported me in various ways throughout this process.

Firstly, I would like to express my gratitude to Prof. Dr. Matias Bargheer, who gave me the opportunity to write my master's thesis as a member of his group. His invaluable feedback and insightful perspectives, especially when faced with challenges, have greatly enriched my work and learning experience.

I am also profoundly grateful to Dr. Wouter Koopman for offering me this topic for my master's thesis and for his guidance throughout this work. His expertise in navigating obstacles with the setup and samples provided me with new approaches when unexpected problems arose. Our discussions and his explanations significantly deepened my understanding of the mechanisms behind the experiments I conducted.

I would like to extend my appreciation to Dr. Felix Stete for introducing me to the lab and instilling in me a fascination for the NOPA setup. His innovative ideas provided invaluable assistance.

A special thanks goes to Dr. Alexander von Reppert, whose support with the lab equipment, particularly related to lasers, was crucial.

Moreover, I am thankful for the regular discussions with all the other group members, which offered me fresh perspectives and stimulated my thinking in new directions. The pleasant working environment fostered by all of you has been highly motivating and has made it easy to ask questions and seek help.

Finally, I am profoundly grateful for the constant support from my partner, friends and family, who have been my reliable source of strength throughout this journey. Their encouragement has been indispensable.

Thank you all for your contributions to the successful completion of this thesis. Without all of you, this would not have been possible.